MICROCOPY RESOLUTION TEST CHART

②

Department of AERONAUTICS and ASTRONAUTICS
STANFORD UNIVERSITY   Report AA CFD 85-2

DTIC
ELECTE
DEC 1 2 1986
S
D

FINAL SCIENTIFIC REPORT
Air Force Office of Scientific Research
Contract AFOSR 82-0083

AD-A175 194

DTIC FILE COPY

COHERENT STRUCTURE MODELING OF VISCOUS SUBLAYER TURBULENCE
FOR INCOMPRESSIBLE FLOW WITH HEAT TRANSFER

by

DALE K. OTA AND DEAN R. CHAPMAN

Submitted to the

Directorate of Aerospace Sciences
Air Force Office of Scientific Research
Bolling AFB
Washington D.C. 20332

by the

Department of Aeronautics and Astronautics
Stanford University
Stanford, CA 94305-2186

May 1985

86 12 12 113

SECURITY CLASSIFICATION OF THIS PAGE (When Data Entered)

REPORT DOCUMENTATION PAGE		READ INSTRUCTIONS BEFORE COMPLETING FORM
1. REPORT NUMBER AFOSR·TR· 86-2104	2. GOVT ACCESSION NO. AD-A	3. RECIPIENT'S CATALOG NUMBER
4. TITLE (and Subtitle) Coherent Structure Modeling of Viscous Sublayer Turbulence for Incompressible Flow with Heat Transfer		5. TYPE OF REPORT & PERIOD COVERED Final Scientific Report
		6. PERFORMING ORG. REPORT NUMBER
7. AUTHOR(s) Dale K. Ota and Dean R. Chapman		8. CONTRACT OR GRANT NUMBER(s) AFOSR 82-0083
9. PERFORMING ORGANIZATION NAME AND ADDRESS Department of Aeronautics and Astronautics Stanford University Stanford, CA 94305		10. PROGRAM ELEMENT, PROJECT, TASK AREA & WORK UNIT NUMBERS 61102F 2703/A2
11. CONTROLLING OFFICE NAME AND ADDRESS Directorate of Aerospace Sciences Air Force Office of Scientific Research Bolling AFB, Washington, D.C. 20332		12. REPORT DATE May 1985
		13. NUMBER OF PAGES 129
14. MONITORING AGENCY NAME & ADDRESS(if different from Controlling Office) Same as 11		15. SECURITY CLASS. (of this report) UNCLASSIFIED
		15a. DECLASSIFICATION/DOWNGRADING SCHEDULE

16. DISTRIBUTION STATEMENT (of this Report)

Approved for public release; distribution unlimited.

17. DISTRIBUTION STATEMENT (of the abstract entered in Block 20, if different from Report)

18. SUPPLEMENTARY NOTES

19. KEY WORDS (Continue on reverse side if necessary and identify by block number)

Fluid Mechanics, heat transfer, turbulent Prandtl number, viscous sublayer, Navier-Stokes, Computational Model.

20. ABSTRACT (Continue on reverse side if necessary and identify by block number)

A Navier-Stokes computational model of the time-dependent dynamics and heat transfer in a viscous sublayer has been developed. The main research objective is to determine the variation of turbulent Prandtl number across the sublayer. Experiments have been unable to define this variation, and existing theories differ greatly.

The computational code uses prescribed temperature and velocity boundary conditions at the outer edge of the sublayer. Numerical

DD $_{1\ JAN\ 73}^{FORM}$ 1473

SECURITY CLASSIFICATION OF THIS PAGE (When Data Entered)

(20. continued)

computations of turbulent Prandtl number have been made for molecular
Prandtl numbers ranging from 0.7 to 6 with zero pressure gradient,
and for adverse, zero, and favorable pressure gradient with a Prandtl
number of 0.7. The results show a strong effect of molecular Prandtl
number on turbulent Prandtl number very near the wall; but only a
relatively small effect of pressure gradient throughout the sublayer.
For most practical computations of heat transfer, the simple assumption
of constant turbulent Prandtl number across the viscous sublayer
appears adequate.

Acknowledgements

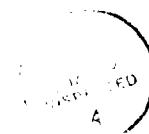| Accesion For		
NTIS CRA&I		☑
DTIC TAB		☐
Unannounced		☐
Justification		
By		
Dist ibution /		
Availability Codes		
Dist	Avail a d / or Special	
A-1		

i

Abstract

The objective of the present research is to compute the variation of turbulent Prandtl number across the viscous sublayer for fluids of different molecular Prandtl number and for flows with adverse and favorable pressure gradients. This is accomplished using a time-dependent compressible Navier-Stokes code together with a coherent structure model of the boundary conditions. Existing theories for turbulent Prandtl number Pr_T near a wall are shown to differ greatly, while experimental measurements are scarce and exhibit a large uncertainty band.

A variety of boundary conditions for the coherent structure model were explored and are briefly described. Numerical results are presented for the set of boundary conditions that yielded the most realistic results for those turbulence quantities which could be compared with experiment.

Computational results for Pr_T have been obtained for the cases of varying molecular Prandtl number from 0.72 to 6.0; for pressure gradients in wall variables of +0.01 (mild adverse),zero, and -0.01 (mild favorable); and for two different wall temperature boundary conditions. These results are compared to various theories and experiments. It is found that the dependence of Pr_T on pressure gradient is negligible; but that the dependence on molecular Prandtl number is sizable near the wall ($y^+ < 3$). Turbulent Prandtl number is found to be essentially constant throughout most of the viscous sublayer for the Prandtl number and pressure gradient variations investigated. It is shown that the assumption of constant Pr_T (0.9) across the viscous sublayer is adequate for practical heat transfer computations.

TABLE OF CONTENTS

NOMENCLATURE

Roman Symbols

a	Constant in stretching function
A	Constant in van Driest formula for eddy viscosity
CFL	Courant Friedrichs Lewy number
c_p	Specific heat
e	Total energy
e_I	Internal energy
l_{max}	Number of grid points in normal direction
LSE	Large Scale Eddy
L	Length Scale
M	Mach Number
M_τ	Friction Mach number $\dfrac{u_\tau}{\sqrt{\gamma R\theta_f}}$
MSE	Medium Scale Eddy
n^- or N	Frequency $\dfrac{n\nu}{u_\tau^2}$
N_1	Bursting frequency per λ_z span
N_{u2}	Frequency of u_{e2} LSE
N_{u2}	Frequency of w_{e2} LSE
$N_{\theta 2}$	Frequency of θ_{e2} LSE
OSF	Oscillating Shear Flow
P^-	Total pressure $\dfrac{P}{\tau_{wall}}$
$\bar{p}^-$	Mean pressure
p^-	Fluctuating pressure
p'	Pressure intensity
Pr_T	Turbulent Prandtl Number
Pr	Molecular Prandtl Number
q_T	Turbulent heat flux
q	Total heat flux
q_u	Total heat flux at wall
R	Gas constant
Re_δ	Reynolds number based on boundary layer thickness
Re_θ	Reynolds number based on momentum thickness

v

Re_L	Reynolds number based on L
R_{uv}	Correlation Coefficient for $\overline{uv}$
$R_{u\theta}$	Correlation Coefficient for $\overline{u\theta}$
$R_{v\theta}$	Correlation Coefficient for $\overline{v\theta}$
$R_{v\theta}$	Correlation Coefficient for $\overline{v\theta}$
SSE	Small Scale Eddy
t^+ or T	Time $\frac{tu_\tau^2}{\nu}$
T_{LSE}	Mean period of the LSE
U_∞	Freestream streamwise velocity
u^+	Streamwise velocity $\frac{u}{u_\tau}$
u_{e1}	SSE u_e Component of VSL model
u_{e2}	LSE u_e Component of VSL model
u_τ	Friction velocity $\sqrt{\frac{\tau_w}{\rho}}$
$\overline{uv}$	Correlation between u and v
VSL	Viscous sublayer
v^+	Normal velocity $\frac{v}{u_\tau}$, $\bar{w}^+$ in Pulliam-Steger notation
v_{e1}	SSE v_e Component of VSL model
v_{e2}	LSE v_e Component of VSL model
w^+	Spanwise velocity $\frac{w}{u_\tau}$, $\bar{v}^+$ in Pulliam-Steger Notation
w_{e1}	SSE w_e Component of VSL model
w_{e2}	LSE w_e Component of VSL model
x^+	Streamwise coordinate $\frac{xu_\tau}{\nu}$
y^+	Normal coordinate $\frac{yu_\tau}{\nu}$, $\bar{z}^+$ in Pulliam-Steger Notation
z^+	Spanwise coordinate $\frac{zu_\tau}{\nu}$, $\bar{y}^+$ in Pulliam-Steger notation

Greek Symbols

α	Intensity of u
β	Intensity of v
δ	Boundary layer thickness
$\Delta\bar{y}$	Spanwise mesh spacing in Pulliam-Steger notation
$\Delta\bar{z}$	Normal mesh spacing in Pulliam-Steger notation
$\eta_{\bar{y}}$	Spanwise metric
ϵ_m	Eddy viscosity

ϵ_q	Thermal eddy diffusivity
γ	Ratio of specific heats
κ	Karman constant
λ_x	Streamwise length of streaks
λ_z	Spanwise spacing of streaks
μ	Viscosity
ν	Kinematic viscosity
$\mathcal{O}_{u2}$	Phase angle for LSE u_e Component
$\mathcal{O}_{v1}$	Phase angle for SSE v_e Component
$\mathcal{O}_{w1}$	Phase angle for SSE w_e Component
$\mathcal{O}_{w2}$	Phase angle for LSE w_e Component
$\mathcal{O}_{\theta1}$	Phase angle for SSE θ_e Component
$\mathcal{O}_{\theta2}$	Phase angle for LSE θ_e Component
ρ^-	Density $\frac{\rho}{\rho_w}$
$\bar\rho^-$	Mean density
ι'	Intensity of θ
σ	Intensity of u'
τ	Total shear stress
τ_w	Total shear stress at wall
θ_{e1}	SSE θ_e Component of VSL model
θ_{e2}	LSE θ_e Component of VSL model
θ_f	Friction temperature
Θ^-	Total temperature $\frac{\Theta}{\theta_f}$
$\bar\theta^+$	Mean temperature
θ^-	Fluctuating temperature
$\bar{\theta v}$	Correlation of v and θ
ξ_x	Streamwise metric
$\varsigma_{\bar z}$	Normal metric
ς	Modified spanwise coordinate $\frac{2\pi z}{\lambda_z}$

Ancillary Symbols

$\overline{(\ )}$	Space and time-averaged mean quantity
$(\ )'$	Turbulence intensity

$( )^-$ Nondimensionalized by wall variables

$( )_e$ Value at outer boundary

$( )_1$ Value of SSE Component

$( )_2$ Value of LSE Component

$( )_w$ Value at wall

LIST OF TABLES

LIST OF FIGURES

x

xii

1. Introduction and Objectives

Many engineering problems today are concerned with some aspect of turbulent flow, and are complicated by the complex nature of turbulence. For most calculations, some type of modeling is used since it would take huge amounts of computer time to capture all of the turbulent dynamics numerically. Many calculations use Reynolds' averaging. Once this is done however the set of conservation equations for mass, momentum, and energy is not closed. This closure problem is solved by expressing the added unknowns in terms of the averaged flow variables.

Many of the terms which need to be modeled for turbulent flow are dominant in the viscous sublayer region very close to the wall. Turbulence kinetic energy production and dissipation have their peak values in the viscous sublayer at about a $y^- \approx 10$ (Hinze 1975). Also 70% of the production of turbulence occurs in the viscous sublayer (Kim et. al. 1971). In the case of turbulent heat transfer, the value of turbulent Prandtl number in the viscous sublayer has been found to be a very important parameter in determining the rate of heat transfer and the temperature profile. The turbulent Prandtl number appears when the energy equation is time-averaged, and is defined as

$$Pr_T = \frac{\overline{u\bar{v}}\,\dfrac{\partial \bar{\theta}^-}{\partial y^-}}{\overline{\theta \bar{v}}\,\dfrac{\partial u^-}{\partial y^-}} \tag{1.1}$$

Difficulties are encountered in measuring the turbulent Prandtl number near wall in the viscous sublayer (hereafter called VSL). This is because experimental measurements are technically difficult to obtain due to the extreme thinness of the viscous sublayer. For a high Reynolds number, $Re_L = 2.0 \times 10^8$, wing cord length $L = 10$m and free stream velocity $U_\infty = 300$m/s in air, the viscous sublayer thickness $\delta_{vsl} = .03$mm. This is approximately .05% of the boundary layer thickness δ, and is typical for a boundary layer on a jet transport wing. For a low Reynolds number, $Re_L = 1.0 \times 10^5$, a flat plate length $L = 1.0$m, and free stream velocity

1

$U_\infty = 20.0$ m s in air, the viscous sublayer thickness $\delta_{vsl} = .7$ mm. This is approximately 5% of the boundary layer thickness δ. This is typical for an experimental channel flow with air. For the higher Re, it is clear that the VSL is very thin. The thickness of the viscous sublayer can be enhanced with low Re and fluids of high viscosity. In wall units, the thickness of the VSL is about $y^- = 40$. Wall units are the conventionally used nondimensionalization in turbulence analysis. The VSL designates the region from the wall to the beginning of the log region which is at about $y^- \approx 30 - 50$. For this study, the edge of the VSL will be at 40. Because the VSL is so thin, near wall measurements of $\overline{uv}$ and $\overline{v\theta}$ correlations are unrealiable due to probe interference effects. This is because the long-dimension of the probe has to be normal to the wall in order to measure the v-velocity component. The measurements of the normal gradients of u and θ are difficult because within the thin VSL, these gradients are very steep. Hence, measurements of Pr_T near a wall are highly uncertain.

Some experimentalists use alternate formulations for the turbulent Prandtl number which involve additional assumptions. These still rely on having accurate values of the velocity and temperature gradients near the wall so their reliabilty can still be questioned. An example of this is the expression used by L.C. Thomas (1982)

$$Pr_T = \frac{\dfrac{1}{\dfrac{\overline{\partial u}}{\partial y}} - 1}{\dfrac{1}{\dfrac{\overline{\partial \theta}}{\partial y}} - \dfrac{1}{\overline{Pr}}} \tag{1.2a}$$

which assumes

$$\frac{\tau}{\tau_w} \approx 1 \qquad \frac{q}{q_w} \approx 1 \tag{1.2b}$$

The extreme experimental difficulties in measuring Pr_T make all measurements of Pr_T in the VSL unreliable. The experimental uncertainty envelope for air

with $Pr = .72$ is shown in figure 1 (Simpson et. al 1973). This shows that even for air as the wall is approached the scatter of the measured value of the turbulent Prandtl number is large. Launder (1978) states that for $Pr > 1$, the scatter of experimental data is so large even away from the wall that the existing data is hard to evaluate except to say there is much scatter. Experimental data for $Pr > 1$ and of non-zero pressure gradients for even casual perusal is scarce. Figure 2 shows two data sets for the Pr_T with adverse pressure gradient. Thomas' data (1982) is from his computational model. Blackwell's data (1972) is experimental. These two data sets show contrasting behavior of the Pr_T in an adverse pressure gradient.

Many analytic expressions have been developed for the turbulent Prandtl number, as illustrated in the survey of Reynolds (1975). The initial assumptions of these various models of the turbulent Prandtl number differ greatly. A basic list of the models would be the following:

(1)   Various mixing length models like the van Driest temperature wall damping function from Stokes flow analogy

(2)   Turbulent heat transfer models like Jenkin's or Diessler's analysis with heat transfer to and from moving spherical eddy

(3)   Formal analysis based on exact equations like Geshev's Green's function analysis on the linearized equations

The validity of these models is hard to estimate since the experimental data varies tremendously. Various existing theories are shown in figures 3-6 for different molecular Prandtl numbers between 0.72 and 1000. As with the experimental data, the turbulent Prandtl number exhibits wide scatter as the wall is approached. The scatter of values of Pr_T is not unexpected since the experimental measurements of Pr_T can give no trends of its behavior in the VSL upon which a reliable theory can be based. For $Pr = .72$, the scatter is not as wide since most of the expressions

3

derived for the turbulent Prandtl number include at least one floating coefficient which was adjusted to give a Pr_T of order 1 in the outer part of the VSL.

The turbulent Prandtl number is very important in the determination of heat transfer; the existing state of knowledge, however, is incomplete and confusing. The present theories and experimental data sets show both strong qualitative and quantitative differences which are impossible to collapse onto any unified curve. Several general conclusions have been advanced from research on the turbulent Prandtl number.(Reynolds 1975, Jischa 1978)

(1) $Pr > 1$ then $Pr_T < 1$

(2) $Pr < 1$ then $Pr_T > 1$

(3) $\dfrac{d\bar{p}^-}{dx^-} > 0$ then Pr_T decreases from its $\dfrac{d\bar{p}^-}{dx^-} = 0$ value

These conclusions only apply to the region away from the wall. There are no general conclusions for the behavior near a wall.

This present state of great uncertainty about the near-wall behavior of the turbulent Prandtl number gives an obvious motivation to undertake a computational investigation. The objectives of the present research are to study the behavior of the turbulent Prandtl number as a function of various parameters. Specifics of the study are to investigate: (1) the dependence of the Pr_T on molecular Prandtl number between $0.72 < Pr < 6.0$; (2) the effect of a mild mean streamwise pressure gradient both adverse and favorable on Pr_T; and (3) the effect on Pr_T of using different temperature wall boundary conditions. Also investigated is the limiting behavior of Pr_T as the wall is approached.

The method chosen for this study is that of a time dependent three dimensional Navier Stokes computation with coherent structure modeling. This approach was developed by Chapman and Kuhn (1981) and Hatziavramidis and Hanratty (1979) for modeling viscous sublayer turbulence in incompressible flow without heat transfer . During the past two decades a great deal of new experimental information

4

has been assembled on the physics of organized eddy structures in turbulent flow especially within the sublayer (Cantwell 1981). Yet it has not been possible thus far to incorporate this body of physical information within the framework of Reynolds-averaged turbulence modeling. A fundamental limitation of the Reynolds-averaged approach is that time averaging is done to the dynamic equations of motion. In this initial mathematical step important physical aspects of organized eddy structures, such as phase relationships and coherent structure dynamics are obliterated irreversibly. Consequently some totally different approach is required if the observed physics of coherent eddy motions are to be incorporated within the framework of a turbulence model.

Coherent structure modeling fits this requirement. This method directly models the essential organized eddy structures observed in experiments. The principle steps in coherent structure modeling are the following:

(1)   model velocity and temperature boundary conditions at the edge of the viscous sublayer

(2)   compute time-dependent dynamics

(3)   time average computed results

Thus time averaging is the last operation performed on the computed dynamics, rather than the first operation performed on the dynamic equations. The study by Chapman and Kuhn (1981) led to surprising success in modeling some important characteristics of viscous sublayer turbulence.

Both the motivations and the payoff for the present research are quite different from those in conventional turbulence modeling. In addition to the specific motivations stated for the present research, there are other important motivations that could affect different areas of turbulence research. It is appropriate, therefore, to outline some of these.

5

Three other motivations for developing a realistic coherent structure model of viscous sublayer turbulence are the following:

(1) *To provide a basis for strengthening a major weak link in present Reynolds average closure schemes* by providing a method of computing the production.destruction. and redistribution terms in the exact transport equation for dissipation or turbulent heat flux which then can be compared against the corresponding modeled terms.

(2) *To provide a simple test flow against which subgrid models of turbulence in large eddy simulations can be tested.* A realistic coherent structure model of viscous sublayer turbulence could be used to test subgrid-scale models for large eddy simulations of turbulent flow in the region adjacent to a wall.

(3) *To provide a guide for modeling the lower boundary conditions for the outer turbulent region in large eddy simulations of boundary layer flow.* If a realistic boundary condition of this type could be developed. the entire viscous sublayer could be modeled rather than directly computed which would greatly help large eddy simulations.

In summary. with these motivations for developing coherent-structure VSL turbulence models. it is clear that the potential payoffs may be of much broader scope than the specific objectives of the present research.

2. Effect of Pr_T on Heat Transfer

The turbulent Prandtl number is an important parameter which appears in the turbulent energy equation when the time-average is taken. Thus, Pr_T is a parameter which must be modeled in computations of turbulent heat transfer from the turbulent boundary layer equations.

In the case of turbulent heat tranfer, the turblulent heat flux is rewritten using a Boussinesq approximation. This still involves an unknown parameter, the thermal eddy diffusivity, ϵ_q.

$$q_T = -\rho c_p \overline{v\theta} \tag{2.1}$$

$$\overline{v\theta} = \epsilon_q \frac{\partial \bar{\theta}^+}{\partial y^+} \tag{2.2}$$

In order to simplify the solution a little more, Reynolds assumed that the mechanisms of energy and momemtum transfer were similar, and then applied dimensional analysis. When this is done, the turbulent Prandtl number is related to the thermal eddy diffusivity in a manner analogous to the molecular Prandtl number. Both Pr and Pr_T are ratios of measures of the diffusivity of momentum to temperature.

$$Pr_T = \frac{\epsilon_m}{\epsilon_q} \tag{2.3}$$

$$q_T = -\rho c_p \frac{\epsilon_m}{Pr_T} \frac{\partial \bar{\theta}^-}{\partial y^-} \tag{2.4}$$

Conventionally, the eddy viscosity ϵ_m is obtained from an empirical equation or a hydrodynamic balance equation. The turbulent Prandtl number is also obtained from an empirical equation. Finally, both these values are then used in the turbulent energy equation which can now be solved. The turbulent Prandtl number is used extensively in many computations; however, its value for fluids of varying Pr and its behavior under different flow conditions is not well understood.

Many investigators have conducted studies on the turbulent Prandtl number with the main objective of estimating its value for many different molecular Prandtl

7

numbers and types of flows. From Reynolds' original analysis, the turbulent Prandtl number is a constant equal to 1. This is called Reynolds analogy. The effect of the presence of the wall was known to be an added difficulty. Near the wall viscous and molecular processes were thought to be dominant and the turbulent Prandtl possibly to be an unimportant parameter. Some experiments (Johnson 1959) have suggested that the turbulent Prandtl number may not be constant across the viscous sublayer. Once this was observed, several researchers investigated the effect of a variable turbulent Prandtl number on the flow solution. Rotta, von Driest, and Reichardt (Schlichting 1979) all concluded that the value of the turbulent Prandtl number near wall in the viscous sublayer is an important parameter in determining the rate of heat transfer and the temperature profile.

A simple computation serves to show this. This computation is similar to that in Rotta's paper (1964) reformulated to emphasize the importance of the turbulent Prandtl number. An equation of temperature as a function of y^+, distance from the wall, Pr, molecular Prandtl number, Pr_T, turbulent Prandtl number, and ϵ_m, eddy viscosity can be written as follows (Kays and Crawford 1980).

$$\bar{\theta}^+ = \int_0^{y^+} \frac{dy^+}{\dfrac{1}{Pr} - \dfrac{\epsilon_q}{\nu}} \tag{2.5}$$

The van Driest formulas for eddy viscosity and the mean streamwise velocity gradient are (Hinze 1975)

$$\frac{\epsilon_m}{\nu} = \kappa^2 y^{+2} \left[1 - \exp \frac{-y^+}{A} \right]^2 \left| \frac{\partial \bar{u}^+}{\partial y^+} \right| \tag{2.6}$$

$$\frac{\partial \bar{u}^+}{\partial y^+} = \frac{2}{1 + \sqrt{1 + 4\kappa^2 y^{+2} \left[1 - \exp \frac{-y^+}{A} \right]^2}} \tag{2.7}$$

where A is a fitted parameter which has a value of 26. Then for a given Pr, a two layer step model for the Pr_T is used to assess the effects on heat transfer. The

8

interface position y_i between the two steps is also an additional variable. The results for $Pr = .72$ (air) and $Pr = 6.0$ (water) are shown graphically in figures 7 and 8. The calculation was first made for a base value of the $Pr_T = 1.0$. Then this was increased and decreased by a factor of two in the inner step region ($y < y_i$). The interface position y_i was moved out until the approximate heat transfer coefficients differed by approximately 20% at the end of the integration. An approximate heat transfer coefficient was computed using the temperature at the end of the integration. These values were used to get an approximate change in the heat transfer coefficient Δh in per cent. Therefore within the value of y_i shown, the value of the Pr_T does not effect the heat transfer solution significantly ($< 20\%$). For $Pr = .72$, this value is around $y^- = 13.7$, and for $Pr = 6.0$, the value is about $y^+ = 7.5$. It can be seen that the value of the Pr_T is important even in regions where molecular diffusion should be dominant. This region moves closer to the wall as the Pr increases which is expected since the thermal layer is getting thinner.

Therefore, if quantitatively accurate heat tranfer computations are desired then accurate values of the turbulent Prandtl number in the viscous sublayer are needed as an input. Since the value of turbulent Prandtl number in the VSL in turbulent heat transfer computations is important, and since experiment and theory have not been able to define the variation of the Pr_T with molecular Pr and mean streamwise pressure gradient (as previously shown),there is a need for a Navier-Stokes computation of the Pr_T distribution in the viscous sublayer.

3. Formulation of Boundary Conditions
for the Viscous Sublayer

The study by Chapman and Kuhn (1981) showed promising viscous sublayer turbulence results for flow with zero heat transfer. In the present study, a similar relatively simple coherent-structure model is developed for the case of flow with heat transfer. Thus the present research provides an extension of their work to flow with heat transfer.

The primary element in formulating the computational model involves the construction of time and space dependent boundary conditions that are as realistic as possible for the fluctuating temperature θ and the fluctuating velocity components u, v, w at the outer edge of the viscous sublayer. These boundary conditions are constructed using various experimental observations as a guide to model the coherent structures present.

The boundary conditions attempt to model the bursting process revealed by experimental observations of flow in the viscous sublayer. The bursting process comprises two events, ejection sweep events and sweep ejection events (Corino and Brodkey 1969, Johansson and Alfredsson 1982). These events are associated with the highly elongate streamwise streaks present in the viscous sublayer. The ejection event is associated with fluid being lifted away from the wall from a low speed streak which is a region of slower moving streamwise fluid. A characteristic of the ejection process is fluid being lifted away from the wall and creating an inflectional profile of the streamwise velocity. When fluid moves towards the wall, high speed streaks which are regions of faster moving streamwise fluid occur. This is called a sweep event. Ensemble conditional averaging shows evidence of contra-rotating vortical motion associated with these high and low speed streaks (Blackwelder and Eckelmann 1979). Iritani (1981) has shown, using liquid crystal flow visualization and the comparison of temperature correlations to velocity correlations, that the temperature field under slight heating conditions also has evidence of a vortical

10

structure. This is logical since temperature should be acting as a passive contaminant. A computational study by Kim (1984) has shown that the the vortical structure does not have any "long legs" which lie along the wall, but instead these legs have characteristic lengths much shorter than the typical length scale of the streaks. These vortex legs lift off immediately forming the horeshoe vortex structure at an angle of 45 degrees. This is in constrast to the model suggested by Blackwelder and Eckelmann of highly elongate contra-rotating vortical pairs associated with the streaks with characteristic lengths of the order of 1000 wall units. (see figure 9). Moser (1984) has indicated, also from a computational study, that the vortical structure does not occur as a contra-rotating pair in a time-instantaneous frame but only in ensemble-averaging. In developing the present VSL model, a simple idealized picture of the time-instantaneous contra-rotating pairs in the VSL is assumed. Regions where the vortices will lift fluid away from the wall are to be associated with the low-speed streaks and where the vortices move fluid towards the wall, this region will be associated with the high-speed streaks. It is noted that this idealized model only corresponds to ensemble conditional averaging of VSL structures, and does not take into account that the vortices lie along the wall for short distances. Whatever the real picture, vortical structure is dominant in the viscous sublayer.

A two eddy component model is chosen for initial development. The two components model the small scale eddies (SSE) together with organized large scale eddies (LSE). These organized large scale eddies exist on top of the VSL and have length scales of order δ. Turbulence, of course, exhibits a wide range of scales in reality. This may be seen from figure 10 showing spectral density data of Fulachier (1972) for the three velocity components and the temperature. It is to be noted that the temperature exhibits scales similar to the streamwise velocity component. The attempt here is try to model the main characteristics of the viscous sublayer with only two eddy scales: one scale λ_z corresponding to the spanwise spacing between streaks, and another scale ℓ much larger than λ_z corresponding to boundary layer

11

thickness. The subscript e refers to outer edge values $(y^- = 40)$. The additional subscript 1 refers to the SSE component and the subcript 2 refers to the LSE component. The general form of the boundary conditions applied at $y_e^- = 40$ is

$$
\begin{array}{ccc}
\text{Component 1 - SSE} & & \text{Component 2 - LSE} \\
\text{scale } \lambda_z & & \text{scale } \delta \\
U - \bar{u} = u_e^- = u_{e1}(x, y_e, z, t) & + & u_{e2}(t) \\
v_e^- = v_{e1}(x, y_e, z, t) & - & v_{e2}(t) \\
w_e^- = w_{e1}(x, y_e, z, t) & - & w_{e2}(t) \\
\Theta - \bar{\theta} = \theta_e^- = \theta_{e1}(x, y_e, z, t) & - & \theta_{e2}(t)
\end{array}
\tag{3.1}
$$

The SSE which are associated with the streaky vortical structure are responsible for the production of turbulence and Reynolds stress. Visual flow observations indicate that the SSE can have characteristic length scales as small as 10-30 wall units. The LSE on the other hand do not produce Reynolds stress. They exist in the region external to the VSL and must be modeled because of their interaction with the SSE and their contribution to pressure fluctuations. The LSE are modeled as an unsteady stream oscillating at the outer edge of the VSL.

This two component model is compatible with the concept of "active" and "inactive" components of turbulent motion in the log region as characterized by Townsend (1961) and Bradshaw (1967). The SSE component is active producing the Reynolds stress. rotational. and dependent on wall variables. The LSE component is inactive. producing pressure fluctuations, irrotational. and dependent on outer variables. There is much experimental information that turbulent flow in the log region and hence at the outer edge of the viscous sublayer comprises these two distinct types of motion. However. Coles (1978) concluded that a three component model is needed to describe the turbulent dynamics in the viscous sublayer. The third component is needed as a transitional component between the "active" SSE

12

and the "inactive" LSE, so the use of only two components may not be sufficiently realistic for some turbulence parameters. Other aspects and complexities of this type could be added without difficulty in principle.

In an effort to incorporate coherent structure observations in a relatively simple two component model, the boundary conditions at the outer edge of the viscous sublayer ($y_c^+ = 40$), as expressed in conventional nondimensional wall variables, are structured as terms harmonic in time and span as follows:

Component 1 - SSE   Component 2 - LSE

$$\text{scale } \lambda_z \qquad\qquad \text{scale } \delta$$

$$u_c^+ = 2\alpha_1 \sin N_1 T \sin \zeta - \sqrt{2(\alpha^2 - \alpha_1^2)} \sin(N_{u2} T - \phi_{u2})$$

$$v_c^+ = 2\beta_1 \sin(N_1 T - \phi_{v1}) \sin \zeta \tag{3.2}$$

$$w_c^+ = 2\sigma_1 \sin(N_1 T - \phi_{u1}) \cos \zeta - \sqrt{2(\sigma^2 - \sigma_1^2)} \sin(N_{w2} T - \phi_{w2})$$

$$\theta_c^+ = 2v_1 \sin(N_1 T - \phi_{\theta 1}) \sin \zeta - \sqrt{2(v^2 - v_1^2)} \sin(N_{\theta 2} T - \phi_{\theta 2})$$

with

$$\lambda_z \quad (\text{Spacing between streaks}) \tag{3.3a}$$

$$\zeta = \frac{2\pi z}{\lambda_z} \tag{3.3b}$$

$$\alpha = u_c', \quad \beta = v_c', \quad \sigma = w_c', \quad v = \theta_c' \tag{3.3c}$$

$$\alpha = \sqrt{\alpha_1^2 - \alpha_2^2}, \quad \beta = \beta_1, \quad \sigma = \sqrt{\sigma_1^2 - \sigma_2^2}, \quad v = \sqrt{v_1^2 - v_2^2} \tag{3.3d}$$

$$(R_{uv})_c = -\frac{\alpha_1}{\alpha} \cos(\phi_{v1}) \tag{3.3e}$$

$$(R_{u\theta})_c = \frac{v_1}{v} \cos(\phi_{v1} - \phi_{\theta 1}) \tag{3.3f}$$

$$(R_{v\theta})_c = \frac{\alpha_2 v_2 \cos(\phi_{\theta 2} - \phi_{u2} - \alpha_1 v_1)}{\alpha v} \tag{3.3g}$$

Experimental measurements give various information about the boundary condition parameters in the computational model. The low speed streaks seen in the

13

viscous sublayer have a spacing of about $\lambda_z^- \approx 100$. This gives the spanwise length of the computational domain. The vortical structure seen by experimentalists is not really periodic. however the vortical pairs have a measurable mean frequency and occur repetitively enough in the viscous sublayer that the term "quasi-periodic" applies (Blackwelder and Eckelmann 1979). In the present model. the streaky structure is assumed to be periodic. hence periodic boundary conditions are applied spanwise. The streaks which alternate with their high and low speed parcels of fluids provide a guide for modeling the spanwise variation of the streamwise velocity u_{e1}^-.

The coherent streamwise velocity structures are highly elongated in the streamwise directions with $\lambda_x^- \approx 1000$. This leads to a mathematical simplification of neglecting derivatives in the streamwise direction (x) compared to the derivatives in the spanwise (z) and normal (y) directions. This basic approximation which involves the computation of three velocity components in two space directions has been either termed "2.5D flow". "slender turbulence theory". or "slender eddy theory". As noted before. the dominant eddy stuctures in the viscous sublayer are streamwise contra-rotating vortices. This information provides a guide for structuring the spanwise variations of v_{e1}^- and u_{e1}^-. To account for the contra-rotating vortical motion. with $\zeta = 2\pi z / \lambda_z$. the v_{e1}^- term is given a $-\sin \zeta$ dependence and the w_{e1}^- term is given a $\cos \zeta$ dependence. The u_{e1}^- term is given a $\sin \zeta$ dependence in view of the observations of conditional samples of the bursting process.The u_{e1}^- term is 180 degrees out of phase with v_{e1}^- (Wallace et. al. 1977). For a heated wall. θ_{e1}^- is in phase with v_{e1}^-. A conditional sample record of velocity and temperature in a bursting process is shown in figure 11 to illustrate this point (Antonia et. al. 1982). This follows the conventional picture. In the ejection process for a heated wall. a temperature parcel transported up ($v > 0$) will be at a higher temperature than its time-mean level. Therefore v, θ. and $v\theta$ will all be positive.

An essential constraint must be placed on v_{e1}^- in order to conserve mass. Since periodic boundary conditions are used in the spanwise direction. there is no

14

net mass flux in the spanwise direction. Also at the wall no mass can flow through. At the outer boundary, therefore, it is required for continuity that

$$\int_{0}^{2\pi} \rho v_{e2} d\varsigma = 0 \tag{3.4}$$

Because v_{e2} is a function of time alone, it must be set to zero for global mass continuity at every instant of time. Additional components for v_e obviously could be added provided such components have a spatial dependence which satisfies the global mass continuity requirement.

In modeling the time variations of the velocity and temperature boundary conditions, sinusoidal functions are used with allowance for phase and frequency differences between the fluctuating components. The frequency is set by the measured frequency of both ejection sweep and sweep, ejection events. Both events occur equally as often in the limit of low threshold and long integration time as shown by Johansson and Alfredson (1982). The structure of the present boundary conditions comprises equal proportions of both. A representative burst frequency has been found from the experimental measurements of Blackwelder and Haritonidis (1983). Their mean frequency of the ejection sweep event is .0035 averaged over space and time in wall units. The frequency for both ejection sweep and sweep ejection events will be twice that using the observation of Johansson and Alfredson. For radian measure, a factor of 2π needs to be added. Using this information, the bursting frequency N_1 has a value of .044. The mean period of the LSE is taken as $T_{LSE} = 56 \ U_\infty$ (Laufer and Narayanan 1971). This sets the frequency $N_{v2} = T_{LSE} \ 2\pi$. The Reynolds number has been chosen so that Re_θ is near 10^3. Measurements of $T_{B\lambda}$ in this Re range have been made, and this avoids the problem of whether $T_{B\lambda}$ scales with wall variables or free stream variables. For this Re_∞, it turns out that $N_{v2} \ N_1$. The values of the intensities of the velocities and

15

the temperature are also used to set some of the parameters. The values at $y_e^- = 40$ are taken as $u_e^{-\prime} \equiv \alpha = 2.0, v_e^{-\prime} \equiv \beta = 1.0, w_e^{+\prime} \equiv \sigma = 1.3$, and $\theta_e^{-\prime} \equiv \upsilon = 1.6$.

Using appropriate correlation data at $y_e^- = 40$ most of the coefficients and phase angles can be determined. Conditional sample data of the burst events show a 180 degree phase difference in u_{e1} and v_{e1} which sets $\phi_{v1} = 0$. Experimental data for a heated plate also show that u_{e1} and θ_{e1} are also 180 out of phase. This sets $\phi_{\theta1} = \pi$. Correlation coefficient measurements of $R_{uv} = -.45$ sets $\alpha_1 = .45\alpha$. and of $R_{v\theta} = .45$ sets $\upsilon_1 = .45\upsilon$. The $R_{u\theta}$ correlation gives a relationship between ϕ_{u2} and $\phi_{\theta2}$.

$$\phi_{\theta2} = \phi_{u2} \mp \arccos\left(\frac{\alpha\upsilon R_{u\theta} - \alpha_1 \upsilon_1}{\alpha_2 \upsilon_2}\right) \tag{3.5}$$

The correlation $R_{u\theta}$ has a value of -0.8 at $y^- = 40$. Also. ϕ_{u1} has been fixed in order to be consistent with experimental data showing that $\dfrac{d(v_e^{-\prime})^2}{dy} \approx 0$. From the boundary conditions of the model.

$$\frac{d(v_e^{-\prime})^2}{dy} = -\frac{4\pi\sigma_1\beta_1}{\lambda_z^-}\cos(\phi_{u1} \quad \phi_{v1}) \tag{3.6}$$

Since $\phi_{v1} \quad 0$ previously. then $\phi_{u1} \quad \pi \quad 2$.

This still leaves some remaining parameters which have not been fixed by experimental data. These are $\sigma_1. N_{u2}. \phi_{v2}. \phi_{u2}.$ and $N_{\theta2}$. Three of these are set by assumption and and two by computational experimentation. Thus. σ_1 is set equal to β_1. since the vortical structure should have comparable magnitudes for v_{e1}^- and u_{e1}^-. Using the assumption of staggered LSE. N_{u2} has been set to $N_{u2} \quad 2$. In view of the similar spectral energy distributions of θ and u. $N_{\theta2}$ is set equal to N_{u2}. The two phase angles set by computational trial are $\phi_{u2} \quad 1.05$ and $\phi_{u2} \quad 3.14$ radians. These parameters have slight effects on the mean velocity profile $u(y). u'.$and uv and were selected to best fit the law of the wall for $u(y)$ and $\theta(y)$.

The use of sinusoidal functions for the time and space variations as boundary conditions for the viscous sublayer model would fall into the category of "psuedo-turbulence". This type of analysis has been useful in turbulence analysis especially in allowing analytic solutions to be obtained for certain idealized flows. These are not real turbulent solutions, but they provide some insight about turbulent flows (Hinze 1975). Most of these analytic attempts reduce the Navier-Stokes equations to some linearized form. The present investigation with boundary conditions which are sinusoidal functions differs slightly since the full Navier-Stokes equations are used for the computation.

Another point about the use of sinusoidal functions for boundary conditions concerns the bursting event. Use of sinusoidal functions in the two-component model does not allow for any negative interactions ($u > 0$ and $v > 0$ or $u < 0$ and $v < 0$). During the burst, these have been measured near the outer egde of the VSL to contribute negatively about 30% to the Reynolds stress (Wallace 1972). The ejection events ($u < 0$ and $v > 0$) and sweep events ($u > 0$ and $v < 0$) near the outer edge of the VSL contribute about 70% and 60% respectively to the Reynolds stress. In this model, there are no negative interactions and the ejection and sweep events contribute equally to the Reynolds stress with 50% each. Also the burst process is a highly intermittent process in time and space. The bursting process makes up only about 20 - 25% of the mean period between bursts. When the burst is not occurring, a relativley quiescent signal is observed. This intermittency is not being modelled with the current sinusoidal functions. A Fourier series type boundary condition is one way the boundary conditions can be modified to model the intermittency better.

With the above considerations, the velocity and temperature boundary conditions for the two-component coherent-structure model of viscous sublayer turbulence become:

17

Component 1 - SSE   Component 2 - LSE

scale λ_z _____ scale δ _____

$$u_\zeta^- = 2\alpha_1 \sin N_1 T \sin\varsigma \quad - \sqrt{2(\alpha^2 - \alpha_1^2)} \sin(N_{u2}T - \phi_{u2})$$

$$v_\zeta^- = -2\beta_1 \sin(N_1 T) \sin\varsigma$$

$$w_\zeta^- = 2\sigma_1 \cos(N_1 T) \cos\varsigma - \sqrt{2(\sigma^2 - \sigma_1^2)} \sin(N_{w2}T - \phi_{w2})$$

$$\theta_\zeta^- = -2v_1 \sin(N_1 T) \sin\varsigma - \sqrt{2(v^2 - v_1^2)} \sin(N_{\theta2}T - \phi_{\theta2})$$

$\qquad\qquad\qquad\qquad\qquad\qquad\qquad\qquad\qquad\qquad$ (3.7)

with

$$N_1 = N_{u2} = N_{\theta2} = .044 \qquad\qquad (3.8a)$$

$$\phi_{u2} = 1.05 \quad \phi_{w2} = 3.14 \quad \phi_{\theta2} = 3.47 \qquad\qquad (3.8b)$$

$$\alpha = 2 \quad \alpha_1 = .9 \quad \beta = \beta_1 = 1.0 \quad \sigma = 1.3 \quad \sigma_1 = 1.0 \quad v = 1.6 \quad v_1 = .72 \qquad (3.8c)$$

These boundary conditions can now be applied to a time-dependent Navier-Stokes code and turbulent quantities can be computed. Figure 12 shows the computational domain and its relation to the boundary layer. When these boundary conditions are applied to the Navier-Stokes equations, all normal (y) derivative quantities are not fixed. These normal derivative quantities are computed as part of the numerical solution of the Navire-Stokes equations. Therefore, for each time step, the boundary conditions with the computed normal derivative terms will be consistent with the Navier-Stokes equations at the boundaries. The LSE component of the boundary conditions are being modelled as an unsteady oscillating flow. To be consistent with oscillating 2-D shear flow, a pressure body force term is added. This term will be described in detail later.

18

4. Development of Computational Code

The numerical scheme selected for the viscous sublayer model is an adaptation and modification of the Pulliam and Steger (1980) code. This code is based on a three dimensional implicit factorized algorithm for the unsteady compressible Navier-Stokes equations with the thin-layer approximation. The code was written for arbitrary geometries and even though the computational domain for the viscous sublayer model is cartesian, the use of metrics makes clustering conveniently easy. The clustering will be discussed later.

The Pulliam-Steger code had to be modified to adapt it to the viscous sublayer model in seven ways as follows: (1) the grid has been stretched to cluster points near the wall and the outer edge; (2) the flow variables have been made nondimensional in the conventional wall variables used for turbulent flows; (3) various necessary viscous terms have been added to bring the Pulliam-Steger "thin layer" code in the full Navier-Stokes form; (4) the boundary conditions have been restructured to be appropriate for computations of viscous sublayer turbulence; (5) the algorithm for time derivatives has been revised for increased accuracy and stability; (6) the dissipation function has been removed; (7) body force term associated with the VSL model has been added; (8) ξ differencing has been dropped using the slender-eddy approximation. After these modifications are described, numerical accuracy and stability will be discussed.

4.1 Basic Code and Finite difference algorithm

Variables have been modified slightly to conform with turbulence convention. The definition of the physical coordinates and velocities in the Pulliam-Steger code is different from turbulent boundary-layer convention. In boundary layer convention, the streamwise direction and velocity are x and u, the normal direction and velocity are y and v, and the spanwise direction and velocity are z and w, respectively. Pulliam and Steger employ a different coordinate system in which their normal direction and velocity are z and w, and their spanwise direction and velocity are y

19

and v. This is NASA wing convention. This convention is also used in meteorology. In order to minimize code changes, their coordinate system is used in the numerical computations and then for the output, the boundary layer convention is used. Overbars will be used to denote the Pulliam and Steger variables. Therefore, the coordinates are $x, y = \bar{z}, z = y$; and the respective velocities are $u, v = \bar{w}, w = v$.

The grid is basic with clustering only in one coordinate. Simple cartesian coordinates are used for the streamwise and spanwise directions. A stretched mesh is used in the normal direction. Hyperbolic tangent clustering is used so that points can be concentrated both near the wall and the outer edge. This allows for greater resolution near the boundaries. The metrics for this transformation are $\xi_x = 1, \eta_{\bar{y}} = 1/\Delta \bar{y}^-, \zeta_{\bar{z}} = 1/\Delta \bar{z}^-$ where $\Delta \bar{y}^-$ and $\Delta \bar{z}^-$ are the mesh spacings in wall units in the spanwise and normal directions respectively. The stretching function used is the following

$$\bar{z}_i = \frac{1}{2}\left(1 - \frac{1}{a}\tanh\left\{\left(\frac{2(l-1)}{(l_{max}-3)} - 1\right)\tanh^{-1}(a)\right\}\right) \qquad (4.1a)$$

$$z_i = z_{max}\frac{\bar{z}_{yi}}{\bar{z}_{max}} \qquad (4.1b)$$

with $a = 0.98$ and $l_{max} = $ number of grid points in the normal direction.

With the grid and Pulliam-Steger notation defined, the nondimensional strong conservation form the the Navier-Stokes equations with all the approximations of the model included in wall variables is now presented.

$$\partial_t \hat{q} = \partial_\eta(\hat{F}_v - \hat{F}) - \partial_\zeta(\hat{G}_v - \hat{G}) - \hat{F}_I \qquad (4.2)$$

where

20

$$\hat{q} = J^{-1} \begin{pmatrix} \rho^- \\ \rho u^- \\ \rho v^- \\ \rho \dot{u}^- \\ e^- \end{pmatrix}$$

$$\hat{F} = J^{-1} \begin{pmatrix} \rho V^- \\ \rho u V^- \\ \rho \bar{v} V^- - \eta_{\dot{y}} p^- \\ \rho u \cdot V^- \\ (e-p) V^- \end{pmatrix} \qquad \hat{G} = J^{-1} \begin{pmatrix} \rho W^- \\ \rho u W^- \\ \rho \bar{v} W^- \\ \rho \bar{u} W^- - \varsigma_{\bar{y}} p^- \\ (e-p) W^- \end{pmatrix} \tag{4.3}$$

and

$$U = u^- , V = \eta_y \bar{v}^- , W = \varsigma_{\bar{z}} \bar{u}^- \tag{4.4}$$

The viscous flux terms are

$$\hat{F}_v = J^{-1} \begin{pmatrix} 0 \\ \eta_v \tau_{xy}^- \\ \eta_y \tau_{yy}^- \\ \eta_v \tau_{\bar{z}y}^- \\ \eta_v \beta_y^- \end{pmatrix} \qquad \hat{G}_v = J^{-1} \begin{pmatrix} 0 \\ \varsigma_{\bar{z}} \tau_{x\bar{z}}^- \\ \varsigma_{\bar{z}} \tau_{\bar{y}\bar{z}}^- \\ \varsigma_{\bar{z}} \tau_{\bar{z}\bar{z}}^- \\ \varsigma_{\bar{z}} \beta_{\bar{z}}^- \end{pmatrix} \tag{4.5}$$

with the body force terms associated with the LSE given by

$$\hat{F}_l = J^{-1} \begin{pmatrix} 0 \\ \dfrac{\partial p_\epsilon^-}{\partial x} \\ \dfrac{\partial p_\epsilon^-}{\partial y} \\ \dfrac{\partial p_\epsilon^-}{\partial \bar{z}} \\ - u \cdot \dfrac{\partial p_\epsilon^-}{\partial x} - \bar{v}_\epsilon \dfrac{\partial p_\epsilon^-}{\partial \bar{y}} - \bar{u}_\epsilon \dfrac{\partial p_e^-}{\partial \bar{z}} \end{pmatrix} \tag{4.6}$$

where

$$\tau_{x\bar{y}}^{-} = \tau_{\bar{y}x}^{-} = \mu u_{\bar{y}}^{-}$$

$$\tau_{\bar{z}x}^{-} = \tau_{x\bar{z}}^{-} = \mu u_{\bar{z}}^{-}$$

$$\tau_{\bar{y}\bar{z}}^{-} = \tau_{\bar{z}\bar{y}}^{-} = \mu(\bar{v}_{\bar{z}}^{-} - \bar{w}_{\bar{y}}^{-})$$

$$\tau_{\bar{y}\bar{y}}^{-} = \lambda(\bar{v}_{\bar{y}}^{-} - \bar{w}_{\bar{z}}^{-}) - 2\mu\bar{v}_{\bar{v}}^{-} \qquad (4.7)$$

$$\tau_{\bar{z}\bar{z}}^{-} = \lambda(\bar{v}_{\bar{y}}^{-} - \bar{w}_{\bar{z}}^{-}) - 2\mu\bar{w}_{\bar{w}}^{-}$$

$$\mathfrak{Z}_{\bar{y}}^{-} = \gamma\kappa Pr^{-1}\partial_{\bar{y}}e_{I}^{-} - u\tau_{\bar{y}x}^{-} - v\tau_{\bar{y}\bar{y}}^{-} - w\tau_{\bar{y}\bar{z}}^{+}$$

$$\mathfrak{Z}_{\bar{z}}^{-} = \gamma\kappa Pr^{-1}\partial_{\bar{z}}e_{I}^{-} - u\tau_{\bar{z}x}^{-} - \bar{v}\tau_{\bar{z}\bar{y}}^{-} - \bar{w}\tau_{\bar{z}\bar{z}}^{-}$$

The internal energy is

$$e_{I}^{-} = \frac{e^{-}}{\rho^{-}} - 0.5(u^{+2} - \bar{v}^{-2} - \bar{w}^{-2}) \qquad (4.8)$$

and pressure

$$p^{-} - (\gamma - 1)\, e^{-} - 0.5\rho^{-}(u^{+2} - \bar{v}^{-2} - \bar{w}^{-2}) \qquad (4.9)$$

Temperature is related to pressure and density using the equation of state for a perfect gas

$$\theta^{-} = \gamma M_{\tau}^{2} p^{-}\ \rho^{-} \qquad (4.10a)$$

$$M_{\tau} = u_{\tau}\ \sqrt{\gamma R \theta_{f}} \qquad (4.10b)$$

where the friction temperature θ_f is defined by

$$\theta_{f} = \frac{q_{u}}{\rho c_{I} u_{-}} \qquad (4.10c)$$

Conventional wall variables are

22

$$u_\tau = \sqrt{\overline{\tau_u \ \rho_u}} \qquad p^- = \frac{p}{\tau_{u'}} \qquad \theta^+ = \frac{\theta}{\theta_f} \qquad \rho^- = \frac{\rho}{\rho_u}$$

$$x^- = \frac{x u_\tau}{\nu} \qquad y^- = \frac{y u_\tau}{\nu} \qquad z^- = \frac{z u_\tau}{\nu}$$

$$u^- = \frac{u}{u_\tau} \qquad v^- = \frac{v}{u_\tau} \qquad w^- = \frac{w}{u_\tau} \qquad (4.11)$$

$$T = t^- = \frac{t u_\tau^2}{\nu} \qquad N = n^- = \frac{n\nu}{u_\tau^2}$$

In this code θ^- represents the absolute temperature in wall variables. When plotting temperature. a modification is made so that $\theta_{u'}^- = 0$. For a heated wall. this becomes: $\theta^- = (\frac{\theta_u - \theta}{\theta_f})$.

The finite-difference scheme used is the Beam-Warming (1978) approximate factorization algorithm in delta form.

$$(I - h\delta_\eta \hat{B}^n - h\delta_\eta J^{-1} B_\iota J)(I - h\delta_\iota \hat{C}^n - h\delta_\iota J^{-1} C_\upsilon J)(\hat{q}^{n-1} - \hat{q}^n)$$

$$= -h\delta_\eta(\hat{F}^n - \hat{F}_\iota^n) - h\delta_\iota(\hat{G}^n - \hat{G}_\upsilon^n) - h\hat{F}_{\iota'} - .5h\Delta q^n \qquad (4.12a)$$

with

$$h = \frac{2\Delta t}{3} \qquad (4.12b)$$

$\hat{B}.\hat{B}_\iota.\hat{C}.\hat{C}_\iota$ are the Jacobian matrices obtained from time linearization of $\hat{F}.\hat{F}_\iota.\hat{G}.\hat{G}_\iota$ respectively. These are written out explicitly in Appendix I. The fourth order dissipation operator typically used has been removed. Various modifications to the code were necessary to make it compatible with the present computational model. Differencing in the ξ direction has been dropped because of the slender-eddy approximation. The addition of the complete set of viscous terms is needed since spanwise motions are to be modeled by the Navier-Stokes equations. Spanwise shear terms were not included in the Pulliam-Steger code because of their thin-layer approximation. The time-differencing was adapted to a three-point backward scheme at the suggestion of Dr. T. Pulliam. The code modification was minimal for this time algorithm change. This modification was made for reasons of stability as

23

shown by Beam and Warming. The nondimensionalization was also changed from free-stream reference used by Pulliam and Steger to the conventional turbulent wall variables as defined previously.

The term not common to the Navier-Stokes equations is the body force term $\dot{F}_p$. The addition of the right hand side term of $\hat{F}_p$ allows for a forcing function compatible with oscillating shear flow. The function $\hat{F}_p$ plays the role of the pressure fluctuations caused by the LSE interaction with the viscous sublayer by setting $\frac{\partial p_e}{\partial x} = \rho \frac{\partial u_{e2}}{\partial t}$ and $\frac{\partial p_e}{\partial z} = -\rho \frac{\partial w_{e2}}{\partial t}$. With these as the imposed pressure gradients. the model is compatible with the "active/inactive" concept mentioned previously. In the VSL model. there is no reason to assume that the external pressure gradients are correlated one to one with the LSE components. It has been found that when the body force terms were not used. the phasing of the $\overline{uv}$ and θ terms near wall.$y^- < 2$. was opposite in sign to experimental measurement. Therefore. the body force terms were necessary to get the near wall phasing of these two components consistent with experiment. Also when a mean streamwise pressure gradient is applied. a constant corresponding to the pressure gradient is added to the $\frac{dp_e}{dx}$ term in $\dot{F}_p$.

4.2 Code Verification and Accuracy Test

Since the Pulliam-Steger code is a compressible code, there is some concern about accuracy and stability since the computation is done at low subsonic Mach numbers. Using a compressible code for this computation is not necessary. however. computations of this type increase the general understanding of how these codes perform in the limit of incompressible flow. An empirically set lower bound to guarantee numerical accuracy and stability is about $M > 0.2$. The code for this research is being run in a low Mach number range (about .1). Therefore since the code for this computation is being used in a very extreme case, a test flow must be computed to show that the numerical scheme is accurate and stable. Oscillating shear flow with isothermal and adiabatic temperature boundary conditions was used

24

as the test flow for assessing the accuracy of the time derivative algorithm and the stability of the present code at low Mach numbers. The boundary conditions for oscillating shear flow are

$$U - \bar{u} - u_e = A \sin nt \qquad \frac{\partial p}{\partial x} = -\rho \frac{\partial u_e}{\partial t}$$

$$w_e = B \sin(mt - \phi) \quad \frac{\partial p}{\partial z} = -\rho \frac{\partial w_e}{\partial t} \qquad (4.13)$$

$$\theta_e = C$$

with $\bar{u} = Dy$, and A.B.C.and D are arbitrary constants. The analytic solution for the velocity fields is given by Chapman and Kuhn (1981). The temperature solution has been worked out and is presented in Appendix II. Test runs of the code for oscillating shear flow gave very accurate results as can be seen in figures 13 and 14. These test runs are for a heating ratio $\frac{\theta_w}{\theta_e} = 1.0$(adiabatic) and 1.1(heated). Mach number $M = .02$, and $Pr = 1.0$. This test shows that time accuracy is good and the compressible code is stable for low Mach numbers. These results show that the errors due to the cross terms from the approximate factorization do not affect the time accuracy. It was found for stability, however,that the parameter M_r from the equation of state should be less than 0.4.

§4.3 Decoupling and Stability

In running the algorithm with the desired boundary conditions, several numerical problems were encountered in the course of research. A brief description of these, and the methods devised to solve or minimize them are described in the following paragraphs.

Global mass continuity needs to be satisfied or else there is a density and pressure build-up. In order to guarantee global mass continuity, it was found that the specification of mass flux variables at the boundaries was necessary. When just the velocities were specified, a large build-up of density and pressure was observed. Consequently, the velocity boundary conditions were changed to boundary

conditions on $\rho u_e^- = \bar{\rho}_e u_e, \rho v_e^- = \bar{\rho}_e v_e$, and $\rho w_e^- = \bar{\rho}_e w_e$. This corrected the problem of the severe density and pressure build-up, however, other problems with the boundary conditions were encountered.

Imposition of boundary conditions on a compressible algorithm still does not have precise rules to follow and thus numerical difficulties can arise if incorrect boundary conditions are imposed. Initially, explicit boundary conditions were implemented in the code. At the outer edge of the viscous sublayer, four boundary conditions have been constructed (equations 3.7). At the wall, the no slip velocity boundary conditions and an isothermal temperature boundary condition also give four boundary conditions. Five boundary conditions are required, however, for a three dimensional compressible code. Conventional numerical schemes use the energy equation or the normal momentum equation to back out pressure as the fifth boundary condition at walls. For the spanwise direction, periodic conditions were imposed on all five variables as stated before. This was implemented by using a block periodic solver. Initially, a normal momentum equation is used as the fifth boundary condition to back out pressure both at the wall and the outer edge.

With these conventional explicit boundary conditions, the code was either unstable or the solution exhibited decoupling. Decoupling is when the solution on adjacent grid points is discontinuous in a saw-tooth fashion, but solutions on every other grid point are continuous. Therefore, there exists a smooth solution for the even points and another for the odd points when decoupling occurs. This is a typical problem when central differencing schemes are used. Decoupling of a solution is often a signal that there is a problem with the boundary condition specification. A signal that a problem exists at the outer boundary can also be seen from the relatively high mass continuity residual which exists there. At the outer edge, the mass continuity residual is about .01, whereas interior continuity residuals are in the range of 10^{-4}. The artificial boundary conditions cause a difficulty for the continuity equation to be satisfied numerically at the outer edge.

26

Problems with decoupling were most noticeable when the oscillating normal velocity component v_e was nonzero. Some of the problems are assumed to be associated with the pressure pulses generated by the oscillating v_e component. The decoupling mainly was observed in $p, p', \bar{v}, v'$, and $\bar{e}$. Decoupling was most noticible at the walls. Also, decoupling became more severe as Prandtl number was increased, the heating ratio $\dfrac{\theta_u}{\theta_e}$ decreased, or the friction velocity increased.

A common method for solving the decoupling problem is the use of an artificial dissipation function. The fourth order artificial dissipation function appearing in the Pulliam-Steger code, however, has been turned off for all computations presented here. The artificial dissipation function is commonly used in central-differencing algorithms like the Pulliam-Steger code to prevent decoupling and to damp high frequencies due to nonlinearities of the Navier-Stokes equations. The artificial dissipation function allows for more coupling between the computational grid points which tends to eliminate decoupling of the solution which can occur with central difference algorithms. It was found that when the aritificial dissipation function is used in the VSL computation, the spatial location of peaks of quantities such as u' are shifted away from experimental measurements. The experimental peak of u' is at about $y^- \approx 12$. The computations to be presented show a peak at about $y^- \approx 13$. (See figure 25) When dissipation was used the peak location moved out beyond a $y^- \approx 25$. If the dissipation was very large, then the peak was wiped out completely. Also dissipation was tried only in the energy equation to try to damp out high values of p', but this proved to be unstable. Localized dissipation near the boundaries was also investigated since the production of the high p' occurs at the boundaries. This was also unstable. Therefore, the dissipation function was not used for any of the computations of sublayer turbulence. The decoupling problem was not solved using dissipation, therefore, the boundary conditions were reconstructed to eliminate or minimize the decoupling problem. The

27

damping of high frequencies from the nonlinearities is hoped to be provided by the natural dissipation of the viscous terms.

Alternative boundary conditions were tried in an attempt to fix the decoupling problem. A characteristics type approach was used to more accurately follow the direction of the propagation of information. The signal direction was specified by the sign of the vertical velocity v_e^-. The boundary conditions for $v_e^- > 0$ are outflow for $u_e^-, v_e^-, w_e^-, p_e^-$, and θ_e^- specified. For $v_e^+ < 0$, $u_e^-, v_e^-, w_e^-, \theta_e^-$ were specified with outflow for p_e^-. Outflow is simple first order extrapolation. This set of boundary conditions is more physically correct for a compressible code; however, these boundary conditions did not help the decoupling; and for Prandtl number greater than .72, the code was more unstable. Other variations of this type of boundary condition were attempted, but, none of them helped solve the decoupling problem and some even did not capture the vortical dynamics needed for the present model.

The characteristic method imposes Neumann type (gradient) boundary conditions when outflow boundary conditions are needed. These boundary conditions, however, have been found to be much more unstable than the Dirichlet boundary conditions for this computation. A modified boundary condition was tried to see if the decoupling problem could be helped. A linear mixed type boundary condition of the form

$$au - b\frac{\partial u}{\partial y} = af_1 - bf_2 \qquad (4.14)$$

was implemented. This should help decoupling since the gradient term will couple the point next to the outer boundary to the applied boundary condition when one-sided differencing is used. This type of boundary condition proved to be stable, however it did not help any of the numerical problems compared to the Dircihlet boundary conditions and therefore was not used.

In view of these results, it was decided to stay with the imposition of Dirichlet boundary conditions for the velocity and the temperature at the outer edge of

the viscous sublayer. This requires, however, that the fifth boundary condition be reformulated to alleviate the numerical problems since the normal momentum equation initially used was inadequate. Note that the viscous terms give the equation set an elliptic character which may allow for a full Dirichlet boundary condition specification. The selection of the fifth boundary condition under these conditions is still unclear and must be chosen by computational experimentation. Many boundary conditions of various Dirichlet Neumann combinations were tried. For example, a radiative type (non-reflecting) energy boundary condition (Bayliss, Turkel 1981) was tried, but this boundary condition made the code unstable. All attempts to rectify the decoupling problem in this manner failed. Many combinations resulted in severe instabilities. It was found that with explicit boundary conditions, the decoupling could not be solved.

Since all formulations with an explicit boundary condition failed, an implicit boundary condition formulation was implemented. Implicit boundary conditions are said to be generally more stable and robust by Beam (1981). As with the explicit formulation, it was decided to go with the Dirichlet specification of the velocities and temperature. The fifth boundary condition which greatly minimized the decoupling problem was found to be the imposition of the full continuity equation at the wall and the outer boundary. This was implemented by expressing the time derivative $\frac{\partial \rho}{\partial t}$ using three-point backward time differencing, the normal flux term $\frac{(\partial \rho v)}{\partial y}$ using first-order one-sided differencing and the spanwise flux term $\frac{(\partial \rho u')}{\partial z}$ using second-order central-differencing. All profiles except for $\bar{e}$ were then found to be smooth and well-behaved, although e showed only slight decoupling near the wall of 1 part in 10^5 (see figure 15). Therefore the continuity equation as the fifth boundary condition is used instead of the normal momentum equation at the wall and the outer boundary to minimize the numerical problems.

29

With the decoupling problem essentially solved, some problems of stability still remained. Limitations on the range of values of the Prandtl number were encountered when the Pr was varied. In the physical world, gases do not have $Pr > 1$. Since the perfect gas law is being used for the equation of state, this limits in reality the Pr range to order one. However, since Pr dependence is a desired parameter to study, the Pr was varied from .72 to 6.0 to explore the effect of Pr. Code instability was encountered for Pr higher than 10.0. This may in some way be associated with the use of a perfect gas law together with Pr values corresponding to liquids. This is obviously unphysical.

Stability bounds also exist for the Courant number. There always seemed to be a minimum Courant number for stability. The minimum Courant munber is about 50. This limits the minimum time step allowed for a given grid. Run conditions have been chosen to be within all stability bounds. The Courant number did not seem to have a maximum bound; however, accuracy was very bad if the Courant number was too large (30000). (Remember that these Courant numbers are in wall variables.) The time step limitation shows that the stability region is of limited size and does not include the region near the origin.

By computational trial runs, the basic stability ranges of this code have been determined as discussed previously in this section. In summary, a basic list of these conditions is given.

(1)　　$M_\tau < 0.4$

(2)　　$Pr \leq 6.0$

(3)　　$(CFL)_{min} > 50.$

(4)　　$(CFL)_{max} < 30000.$

The viscous sublayer model implemented in the Pulliam-Steger Navier-Stokes code was then run on the CRAY-XMP, and computational results obtained for various turbulence quantities.

5. Computational Results and Discussion

In starting the VSL computation, initial conditions at time zero are required. Initial profiles for u and θ were imposed which are linear piecewise continuous and match the mean slope at the wall and the mean slope of the law of the wall at $y^- = 40$. The density is set so that the initial pressure is a constant using the perfect gas law. Initial values for v and w are set to zero. The boundary conditions on velocity and temperature (equations 3.7) are slowly turned on using an exponential growth cycle of two N_1 cycles. Periodic flow conditions developed in about six N_1 cycles. The code seems to be relatively insensitive to how the model boundary conditions are started up. An important requirement, however, is to set the correct mean values for u_e and $\bar{\theta}_e$ in the initial conditions. If this is not done, the mean profiles will not be correct even after periodic conditions are achieved. Computations were made for ten N_1 cycles. Averages over space and time starting from the seventh N_1 cycle were taken to provide the various turbulence statistics. Figures 16(a),(b),(c),and (d) show contour plots of the vertical velocity component v before any averaging is applied. It can be seen that the contours for v at $N_1 T = \frac{\pi}{4}$ and $\frac{3}{4}$ are consistent with contra-rotating vortical motion. This illustrates that the imposed outer edge boundary conditions are producing the desired vortical motion in the computational domain.

The typical run conditions were

(1)   360 time steps per N_1 cycle

(2)   39 grid points in the normal direction, 25 grid points in the spanwise direction

(3) $\theta_{wall} = 300$ degrees Kelvin, $\theta_e = 290$ degrees Kelvin

(4) $Re = 23,300$, $U_\infty = 50$ m/s.

Run times were about 600 seconds CPU time on the CRAY-XMP. To check flow periodicity and code stability, some longer runs were made with up to 4000

31

seconds CPU time with the grid essentially doubled to 79 points in the normal direction and 39 points in the spanwise direction, and with time step also refined.

Output quantities such as the mean velocities $\bar{u}, \bar{v}, \bar{w}$, mean density $\bar{\rho}$, mean temperature $\bar{\theta}$, mean pressure $\bar{p}$, velocity intensities, u', v', w', density intensity ρ', pressure intensity p', and temperature intensity θ'. Reynolds stresses, $\overline{uv}, \overline{uw}$, $\overline{vw}, \overline{v\theta}, \overline{u\theta}, \overline{w\theta}$, correlation coefficients, $R_{uv}, R_{v\theta}, R_{u\theta}$ and additional correlations such as flatness and skewness are computed as space and time averages. The results for these hydrodynamic and thermodynamic quantities in the VSL for $Pr = 0.72$ are presented graphically. (see figures 19-30) Before discussing these results, however, a brief outline is presented of two irregularities observed in the computations: near the boundaries, and in the pressure fluctuations.

5.1 Irregularities Near Outer Edge and Wall Boundary

In developing the computational model it has been found that control of the gradients of quantities near the outer edge is very difficult with the boundary condition parameters available. Variation of these parameters seem to effect the values most significantly in the region $y^- < 35$. From $y^- = 35 - 40$, there seems to be a "Stokes-type layer", where the physical quantities are adjusting to the artificially forced motion of the applied boundary conditions. This can been seen in figure 17 which shows the mean gradients of streamwise velocity and temperature. Anomalous variations exist just inside the outer boundary ($y^- = 40$), but relax to realistic variations at about a y^- of 35. This anomalous region extends slightly further towards the wall as Pr increases and if a mean favorable streamwise pressure gradient is imposed. The adverse pressure gradient does not seem to extend the anomalous region at all. In these situations the anomalous region will extend down to about $y^- \approx 30$. Because of the relaxation behavior of gradient type quantities in our model, and because Pr_T is made up of two gradients, values of the Pr_T will be restricted to $y^- \cdot 35$, since the values for $35 \cdot y^- \cdot 40$ are not physically realistic.

32

All profiles are smooth except for some of the correlations like $\overline{uv}$ and $\overline{v\theta}$ which exhibit a wiggle in their values very near the wall. ($y^- < .4$) This is a numerical problem which may still be associated with a boundary condition problem at the wall. Also slight decoupling exists in mean total energy $\bar{e}$ of 1 part in 10^5 as mentioned before (see figure 15). This decouping is localized near the wall and its region of influence increases as Pr increases. The final boundary conditions for the wall are the best that could be achieved for the present model, but still yield some wall boundary irregularities.

The computed turbulent Prandtl number involves two of the correlations which exhibits these "wiggles", and hence is affected by the near-wall numerical problems. Figure 18 shows the near wall behavior of Pr_T for $Pr = 0.72$ as the grid is refined by a factor of 2. The grid dependency shows up for the region $y^- < 0.4$. For $y^- > 0.4$ the results are the same. These wiggles can be eliminated with a coarser grid; however, the finer grid is desired for increased resolution near the wall. Because of the small grid dependence of the computed values near the wall, values plotted in the figures are restricted to $y^- > 0.4$.

Major effects of grid changes show up in the computation of the pressure. Also effected in a lesser degree are density and temperature. The velocity components are unaffected. When the grid is progressively refined, a sharp kink in pressure at the wall develops. This is another signal that there still may be a boundary condition problem at the wall. The wiggles of $\overline{uv}, \overline{v\theta}$ and e near wall are also thought to be partly caused by the artificially high pressure intentsity at the wall. Runs have been made where the pressure field fluctuations have been manually reduced each time step by equal proportions so that $p'_u \approx 5$ (reasonable experimental value). When this has been done, there is no decoupling in $\bar{e}$ and no wiggle in $\overline{uv}$. This shows that the high pressure intensity at the wall may contribute to the numerical problem at the wall. This method is not used since the pressure field damping is

33

arbitrary, and has no physical basis behind it. The results, however, illustrate quite well the effect of pressure on the near wall quantities.

5.2 Pressure Fluctuations

The computed intensities of pressure fluctuations in wall variables varies from 12 to 22 for Pr from .72 to 6.0 and for $\dfrac{dp^-}{dx}$ from $-.01$ to $-.01$ (See figures 29(c),31(d),33(d),35(d),38(b),40(b)). These values of p' are much higher than experimental measurements of $p'_{u\,all}$ which are in the range of $3 - 5$. However the computed values are close to the high end of a theoretical range developed by Kraichnan which is $p'_u \approx 12$ (Hinze 1975). The high values of p' are believed to be caused by pressure waves generated by boundary reflections of energy. At the outer boundary, very steep gradients of the velocity field also contribute to the high pressure intensity through the pressure gradient term of the normal momentum equation. A solution to this would appear to be the construction of a non-reflecting boundary condition for energy, and the minimization of the steep gradients of the velocity field at the outer boundary. This was attempted as discussed in the previous chapter: but, only the decoupling problem in the vertical velocity field was solved.

It is known that high values of p' can be a sign that there is a numerical or physical problem. High values of p' signaled the fact that mass was being pumped into the computational domain when the velocities u_e, v_e, w_e rather than the mass fluxes were being specified. The solution to this problem ,as noted earlier, was the change to mass flux specification, $\rho u_e, \rho v_e, \rho w_e$ at the outer boundary. It has been found that p' in the present computations is affected by grid spacing, time step, boundary conditions, M_∞, and Pr. These changes in p', however, seem to have negligible effect on the other thermodynamic and flow variables. When parameters were chosen near a stablilty bound (for example when a time step was getting too small), very large p' and θ' values were generated. In these cases, the very large values of p' affect the temperature field.

34

The value of p' can be checked at the wall to make sure its value is correct in relation to the other thermodynamic variables. This can be done by evaluating the equation of state for a perfect gas at the wall with an isothermal wall boundary condition on temperature. This relation for pressure intensity is

$$(p')_u = \frac{(\bar{\theta})_u (\rho')_u}{\gamma M_\tau^2} \tag{5.1}$$

The following table, using the values of $(\bar{\theta})_u$, $(\rho')_u$, and M_τ from the computational runs, shows that the computed values of p' are consistent with the equation of state.

		Table 5.1			
		Comparison of values of $(p')_u$			
Pr	$(\bar{\theta})_u$	M_τ	$(\rho')_u$	$(p')_u$ Eqn.	$(p')_u$ Comp.
0.72	549.3	0.1573	.00101	16.02	16.03
1.50	746.9	0.1834	.00082	13.01	12.98
3.0	1044.0	0.2169	.00088	13.95	14.00
6.0	1519.0	0.2616	.00097	15.38	15.44

It was also found that high values of p' can be generated if $M_\tau \ll 1$. This is evident by refering to equation (5.1) In these cases the high values of p' seem to have little effect on the other variables. Again, parameters for the present data runs are such that $p' \approx 12 - 22$. It is noted here that for all computational runs and for all boundary conditions, $\bar{p}$ is essentially constant throughout the VSL. This agrees with the conventional steady state two-dimensional boundary layer assumption that $\frac{\partial p}{\partial y} = 0$.

§5.3 Velocities, Temperature, and Turbulent Prandtl Number

The computational model has been constructed so that the four quantities which make up Pr_T, namely, $\overline{uv}, \overline{v\theta}, \frac{\partial u}{\partial y}$, and $\frac{\partial \theta}{\partial y}$ are as realistic as possible for the given boundary conditions. Model parameters were set up as described earlier in an

effort to have the values for $\bar{u}$, $\bar{\theta}$, and $\overline{uv}$ fit as well as possible the experimental values for $Pr = .72$ (Air) with zero pressure gradient. Most of the available experimental data for $\bar{\theta}$, θ', $R_{u\theta}$, and $R_{v\theta}$ are for $Pr = .72$. This Prandtl number allows for the most complete comparison of the model's results involving temperature terms. The computational and experimental data for $Pr = 0.72$ have been plotted in figures 19-26. Additional data for the VSL computation can be found in figures 27-30.

The mean gradients $\dfrac{\partial \bar{u}}{\partial y}$ and $\dfrac{\partial \bar{\theta}}{\partial y}$ are compared with experiment indirectly by looking at the profiles for $\bar{u}$ and $\bar{\theta}$. Both the computed mean streamwise velocity and mean temperature profiles follow the experimental data fairly well. (see figures 18 and 23) The slopes at the wall. $\left(\dfrac{\partial \bar{u}}{\partial y}\right)_{wall}$ and $\left(\dfrac{\partial \bar{\theta}}{\partial y}\right)_{wall}$. are within 5% of their theoretical values of 1.0 and $Pr = 0.72$. respectively. The mean gradients $\dfrac{\partial \bar{u}}{\partial y}$ and $\dfrac{\partial \bar{\theta}}{\partial y}$ are realistic up to about $y^+ \approx 36$.

The Reynolds stress $\overline{uv}$ is consistent with experimental measurements. (See figure 21) Values of $\overline{uv}$ seem to be slightly high near the outer boundary when compared to the experimental data shown. Overall. the profile for the Reynolds stress compares well with experiment.

Experimental data for $\overline{v\theta}$ is not directly available near a wall. but is indirectly available in the form of the correlation coefficient (See figure 26). The correlation coefficient $R_{v\theta} = \dfrac{\overline{v\theta}}{v'\theta'}$ has been experimentally measured to be about .45 at a $y^- \approx 40$. This value has been used as a boundary condition for the model. The experimental values of $R_{v\theta}$ had to be slightly extrapolated. The closest data points for $R_{v\theta}$ were from a y^+ of about 50 to 70. The two experimental data sets used to get extrapolated values of $R_{v\theta}$ decrease as the wall is approached $(50 < y^- < 100)$. If this trend is to continue in the viscous sublayer.it would be inconsistent with the computed results. The behavior of $R_{v\theta}$ can be expected to be similar to that of $- R_{uv}$. for a heated wall as long as θ is behaving as a passive scalar. (Refer to figures 22 and 26) The computed curves for both exhibit similar behavior.

36

Townsend (1976) states that in the VSL, the correlation $R_{v\theta}$ has an experimental range between .50 – .55. The computed results are in this range. Also, the curves for $\overline{uv}$ and $\overline{v\theta}$, like R_{ut} and $R_{v\theta}$, are similar as might be expected (See figures 21 and 28(d)). As an additional check, the correlation coefficient $R_{u\theta}$ can be seen in figure 25 to compare well with experimental measurements. Therefore all four quantities which make up the Pr_T seem physically reasonable for $Pr = .72$.

Once the VSL model boundary condition parameters $\mathcal{O}_{u2}$, $\mathcal{O}_{\theta2}$, and $\mathcal{O}_{u2}$ were set for $Pr = 0.72$ and zero pressure gradient, the model was held constant and the parameters of Pr and $\dfrac{d\bar{p}}{dx}$ were varied. Data for the varying Prandtl number and pressure gradient runs can be found in figures 31-40. Only computational results for quantities involving temperature ,pressure and density are shown for the different Prandtl number runs. This is because the hydrodynamic results are essentially constant as Prandtl number varies. The Pr range is from .72 to 6.0, and the mean streamwise pressure gradient was varied from $-.01$ to $-.01$. With changing $\dfrac{\partial \bar{p}}{\partial x}$ a corresponding change in the bursting frequency N_1 of the SSE was employed to conform to the experimental data by Schraub and Kline (1965). Values of the Bursting frequency N_1 with pressure gradient are tabulated below.

<div align="center">

Table 5.2

Values of N_1 with Pressure Gradient

$\dfrac{dp}{dx}$	N_1
-0.01	0.0358
0.0	0.0440
−0.01	0.0583

</div>

The turbulent Prandtl number Pr_T for each of the different runs can now be compared. The computed results for variations in molecular Prandtl number Pr for an isothermal wall are presented in figure 41. The results have similar characteristics with several existing theories for Pr_T (refer back to figures 3-6).

The Pr_T is about one for the whole Pr range examined. except near the wall. In the region $y^- < 3$. Pr_T is stongly affected by Pr. As Pr is increased. Pr_T near the wall increases almost proportionally. Of the theories listed. only the ones by Geshev (1978). P.L. Maksin et. al. (1977). and L.C. Thomas (1981) show an increase of Pr_T as Pr increases. The others show opposite behavior or no dependence on Pr. Geshev's model is from a formal Green's function solution to the linearized momentum and energy equations. Thomas' model is a modified surface renewal model. Maksin's model uses the transport equation for $\overline{v\theta}$. All of these models including the present model have been developed from very different viewpoints. however. all are qualitatively alike. The increase of Pr_T for the VSL model is much stronger than for the theories of Geshev. Maksin and Thomas. The model of Geshev has two different wall temperature boundary conditions, isothermal and adiabatic. Geshev's result for the adiabatic wall boundary condition indicates that Pr_T goes to zero at the wall for all Prandtl numbers. Geshev's result for the isothermal wall boundary condition shows Pr_T increasing at the wall with increasing molecular Prandtl number. Finite peak values of Pr_T are attained for finite Pr. For $Pr \rightarrow \infty$. then $Pr_T \rightarrow \infty$. Geshev's analysis indicates the near wall behavior of Pr_T to be dependent on the wall boundary condition. The wall temperature boundary condition for the present computation is isothermal. The computed Pr_T for the present model is in qualitative agreement with Geshev's model for isothermal wall boundary conditions. The computational models of Thomas and Maksin are also for isothermal wall boundary conditions. Again. these computed results of Pr_T are in qualitative agreement with the isothermal result of Geshev. For other turbulent Prandtl number models. various other temperature boundary treatments have been employed. For example. Cebeci also allows for isothermal wall boundary conditions. but in an indirect way by using damped wall functions for the eddy diffusivity ϵ_q. This is analogous to the damping functions developed for the eddy viscosity ϵ_m.

38

The high values for Pr_T near the wall for $Pr = 6.0$ are also in qualitative agreement with the results of Simonek (1983). He states that the behavior of $\overline{v\theta}$ near the wall changes from a third power behavior with y^- to a fourth power when Pr is greater than 7. This also will cause Pr_T to increase as the wall is approached. since this will give Pr_T a $\dfrac{1}{y^-}$ behavior. This study does not have any Pr greater than 7. however a check can be made with the $Pr = 6.0$ computation since it it is close the the "transition" Pr of 7.

The power law log-log plots for $Pr = 0.72$ in figures 43-45 show behavior close to. but not precisely. as $u' \sim y^-.v' \sim y^{-2}.w' \sim y^+.\theta' \sim y^-.\overline{uv} \sim y^{-3}$ and $\overline{v\theta} \sim y^{-3}$. In figures 46-48. the correlation $\overline{v\theta}$ is plotted logarithmically to show the near-wall behavior as Pr is increased. Figure 48 for $Pr = 6.0$ shows a definite increase in the slope of the correlation $\overline{v\theta}$ to $\sim y^{-4}$. The other quantities $u'.v'.w'.\theta'.\overline{uv}.\overline{u\theta}$ do not change with Pr. Only $\overline{v\theta}$ is affected. As Prandtl number is increased. $\overline{v\theta}$ shows a gradual increase of slope. indicating a smooth transition from the third power law to the fourth power law.

The following tables show values of Pr_T at the wall for the present computation and three other models which are qualitatively similar. The listed wall value of Pr_T for the present computations is the value at $y^- = 0.4$. This is the closest point which is not grid dependent. as previously noted.

39

Table 5.3

Values of Pr_T at the wall

Pr	Present Computation		Pr	Geshev
0.72	0.83		1.00	1.00
1.50	1.10		2.00	1.50
3.00	1.76		5.00	2.30
6.00	4.62		10.0	3.10

Pr	Maksin		Pr	Thomas
0.70	0.60		0.72	1.00
2.00	1.30		1.00	1.00
3.00	1.50		2.00	1.40
8.00	1.80		5.00	2.40

The wall values of Pr_T are tabulated for values of Pr somewhat different from the values used in the present computations due to the fact that the results for some models were reported only for certain Pr and analytic equations were not available.

For the present model,there is a common intersection point near $y^- \approx 3$ where Pr_T is nearly independent of the Pr. Only one other theory exhibits a crossover point like this. and that is the model of Thomas. However in this case the crossover is not at a common point and is near $y^- \approx 20$. In the outer region of the viscous sublayer ($y^+ > 25$). the effect of Pr on Pr_T is relatively small. This is anticipated since turbulent transport in this region is greater than molecular transport. The trend of the behavior of Pr_T with Pr in the region away from the wall is consistent with the general rules of Reynolds and Jischa (mentioned in chapter 1) which are $Pr_T > 1$ for $Pr < 1$ and, $Pr_T < 1$ for $Pr > 1$. The theories of Geshev and Maksin do not show this behavior.

The computed effect of a mean streamwise pressure gradient on Pr_T for air ($Pr = .72$) with an isothermal wall boundary condition is relatively small for

both adverse and favorable pressure gradients. as as illustrated in figure 42. These can be compared with the computational and experimental data shown previously in figure 2. The effect of $\frac{d\bar{p}}{d\bar{x}}$ on Pr_T near the wall is the same as near the outer edge. Near the outer edge. the trend of increasing Pr_T with increasing favorable pressure gradient deduced form experimental data (Launder 1978. Blackwell 1972). and stated as a general rule by Reynolds and Jischa, is not seen. The opposite trend of decreasing Pr_T with increasing favorable pressure gradient is observed and this agrees with the behavior indicated by the recent theory of Thomas (1982). The following two tables illustrate the trend of decreasing Pr_T with with increasing favorable pressure gradient for the present model and for Thomas' model. The first table is for the near wall region ($y^- = 5$). and the second for the outer region of the viscous sublayer ($y^- = 20$). Both tables are for $Pr = 0.72$. The experimental data of Blackwell. also included in the tables. are seen to show the opposite behavior.

Table 5.4			
Values of Pr_T at $y^- = 5$			
$\dfrac{d\bar{p}^-}{d\bar{x}^-}$	Present Computation	Thomas Computation	Blackwell Experiment
-0.01	0.93	—	—
-0.00	0.98	0.85	1.80
-0.01	1.04	1.00	1.60

Table 5.5			
Values of Pr_T at $y^- = 20$			
$\dfrac{d\bar{p}^-}{d\bar{x}^-}$	Present Computation	Thomas Computation	Blackwell Experiment
-0.01	0.87	—	—
-0.00	0.99	0.90	0.85
-0.01	1.04	1.10	0.75

Some of the boundary condition parameters were found to effect the temperature results. For example, the maximum temperature intensity seems most strongly influenced by the applied u_ϵ and v_ϵ intensity levels. The higher those intensity levels, the higher θ'_{max}. The applied θ_ϵ could be set to zero, however, and the θ'_{max} is still about the same. Similarly, the $R_{v\theta}$ and $R_{u\theta}$ boundary conditions' main effect is on the $\theta(y)$ profile, however, the variations due to these boundary conditions are small.

Figures 23 for $Pr = 0.72$ and 34(a) for $Pr = 6.0$ show the mean temperature profiles for the different Prandtl numbers. As the molecular Pr number is increased, the temperature profiles become imbedded closer to the wall as is expected. Numerical problems occur, however, at $Pr > 6$. Gradients of mean temperature start to oscillate, causing positive gradients with a heated wall when the mean gradients should be negative. Adjustment of the boundary condition parameters, $\sigma_{u2}, \sigma_{u2}, \sigma_{\theta2}$ helps a little but at $Pr > 10$, the mean temperature starts developing major inflecton points in its profile. The inherent steep gradient of $\bar\theta$ near the outer boundary becomes an increasingly major numerical problem as the Pr increases.

There is considerable uncertainty about the dependence of the outer edge temperature boundary conditions on Pr. In this study, no dependence of the quantities θ'_ϵ, $(R_{u\theta})_\epsilon$, and $(R_{v\theta})_\epsilon$ on Pr is included. For the mean temperature $\bar\theta_\epsilon$ in the temperature boundary condition, Kader's empirical equation (1981) was used to formulate a Pr dependence. Its applicability is from $.001 < Pr < 1000$ well within the Pr range of this study. Kader's equation is

$$\theta^- = Pr\, y^- \exp(-\Gamma) + 2.12 \ln\left((1 - y^-)\frac{2.5(2 - \frac{y}{\delta})}{1 - 4(1 - \frac{y}{\delta})^2}\right) + \chi(Pr)\, \exp(-1/\Gamma) \quad (5.2a)$$

with

$$\chi(Pr) = (3.85 Pr^{\frac{1}{3}} - 1.3)^2 - 2.12\ln Pr \qquad (5.2b)$$

$$\Gamma = \frac{.01(Pry^-)^4}{1 - 5Pr^3 y^-} \qquad (5.2c)$$

As regards the $R_{v\theta}$ correlation at the outer edge. Lawn (Launder 1978) has suggested that this correlation is independent of Pr, and that Pr effects are only to be seen in the θ' values. The present computed results do not conform with this. At the outer boundary ($y^- = 40$), $R_{v\theta}$ decreases with increasing Pr as does $R_{u\theta}$. Temperature intensity θ' increases with increasing Pr. When a Prandtl number dependence in the boundary conditions was attempted, the quantities involving temperature would vary slightly. Because no experimental results were available for $R_{u\theta}$ and $R_{v\theta}$ at higher Pr, it was decided not to try to construct such a dependence.

Fulachier (1984) states that the mean temperature intensity is determined by the mean turbulent kinetic energy. This was shown to be plausible by the similarity of the spectral distributions of temperature and kinetic energy. Some computational runs were made with a temperature boundary condition proportional to kinetic energy.

$$\theta_e = cq \qquad (5.3)$$

It was found that $c = 1.0$ gave good results for mean temperature and temperature intensity very similar to the two component model. With this temperature boundary condition. there is no control over $(R_{v\theta})_e$ and $(R_{u\theta})_e$. With this model, $(R_{v\theta})_e = 0.45$ and $(R_{u\theta})_e = 0.98$. Results for Prandtl numbers up to 6 gave similar results to the two component model for temperature. Fulachier did not include any Prandtl number dependence which should also be included in the expression 5.3. This shows that this may be a boundary condition for temperature which may

be physically correct. This boundary condition yielded results very close t'e two component model.

Behavior of the computed mean streamwise velocity at the wall is consistent with experiment when there is an imposed mean streamwise pressure gradient (See figures 19.37(a).39(a)). The mean temperature gradient is essentially unchanged. (See figures 23.37(e).39(e)). These pressure gradient runs are for $Pr = 0.72$. With a favorable pressure gradient. the mean velocity gradient increased slightly. With $\frac{d\bar{p}}{dx} = -.01$. the mean velocity gradient increased by 4% and the mean temperature gradient increased by 1.0%. The adverse pressure gradient had the opposite effect with the mean velocity. With $\frac{d\bar{p}}{dx} = .01$. the mean velocity gradient decreased by 11% and the mean temperature gradient increased by 1.0%. Experiment shows that $\bar{u}^-$ and $\bar{\theta}^-$ are relatively insensitive to pressure gradient for the region $y^- < 30$. The changes of $\bar{u}^-$ and $\bar{\theta}^-$ for the present computation are small and within experimental data scatter (Thomas and Benton 1982).

The values of u' and θ' for $Pr = 0.72$ are considerably higher than experimental measurements (See figures 20 and 24). These values are a strong function of the applied intensity of v_ϵ. The high u' does not seem to effect $\overline{uv}$ much. However. since $u\bar{v}$ and $\frac{\partial \bar{u}}{\partial y}$ both scale with u'. and their ratio appears in the defining equation for Pr_T. some of the problem with u' will tend to be cancelled out. A similar argument can be made for the high θ' values since $\overline{v\theta}$ and $\frac{\partial \bar{\theta}}{\partial y}$ also occurs as a ratio in the equation for Pr_T.(Tennekes and Lumley 1972)

Some qualitative statements can be made about $u'.\theta'$, and ρ'. Using two-dimensional boundary layer analysis as outlined by Cebeci and Bradshaw (1984). two relations can be derived with the assumptions

$$v << u. w = 0. \frac{p'}{\bar{p}} << \frac{\rho'}{\bar{\rho}} \tag{5.4a}$$

which are

$$\frac{\theta'}{\theta_{wall} - \theta_\epsilon} \sim \frac{u'}{u_\epsilon} \tag{5.4b}$$

44

$$\frac{\rho'}{\rho_e} \sim \frac{u'}{u_\epsilon} \qquad\qquad (5.4c)$$

These two relations show that both θ' and ρ' behave similarly to u'. Figures 20.24.30(d) show that this is qualitatively true for Pr = .72.

Remarks on some of the other turbulent quantities can be made. The flow being computed has a two-dimensional main flow. That means $\bar{u} = f(y)$, $\bar{v} = 0$, and $\bar{w} = 0$. Figures 27(a) and 33(b) show that $\bar{v}$ and $\bar{w}$ are small but not zero. Using the homogeneity and the symmetry condition of the flow in planes perpendicular to the spanwise z direction, the correlations involving the spanwise velocity w have to be zero. Figures 28(a).28(b).28(e) show that the correlations $\overline{uw}.\overline{vw}$. and $\overline{w\theta}$ for $Pr = 0.72$ are small but again not exactly zero. It can be seen that the higher order correlations do not match experimental values all that well. This can be seen by looking at the plots for the skewnesses of u,θ. and $\overline{uv}$ and the flatnesses of $u.\theta$. and $\overline{uv}$. These are presented in figures 29(a) to 29(f) for $Pr = 0.72$.

§5.4 **Effect on Heat Transfer**

The computed Pr_T was inserted into the one dimensional mean temperature equation (equation 1.5). This was done to see what effects the numerically computed variations with molecular Prandtl number would have on the mean temperature profile and the convective heat transfer coefficient relative to the corresponding effects of some reference model. For this comparison the base model used for Pr_T is that of Kays and Crawford (1980). Qualitatively this model is different from the present model in that Pr_T for the Kays-Crawford model decreases with Pr. whereas it increases in the present model. Also. this is an established model for Pr_T known to give good results for temperature profiles in fluids of different Prandtl numbers. The numerically computed Pr_T compared to the model of Kays-Crawford gives somewhat different temperature profiles as shown in figures 49-52 and hence would yield a corresponding difference in the convective heat transfer coefficient . Again. only an approximate heat transfer coefficient can be obtained using the

values of temperature at the outer boundary instead of the freestream temperature. The differences Δh in heat transfer are 5.4% for Pr = .72.8.2% for Pr = 1.5. 9.4% for Pr - 3.0. and 10.7% for Pr = 6.0. These differences are not very large and increase slightly with Pr for the given Pr range. It must be noted that the temperature differences even for Pr = 6.0 are still within the experimental error range of the temperature measurements for Pr = .72 of about 15% (see figure 23). All the temperature profiles using the computed Pr_T fall below the profiles of the Kays-Crawford model.

To see the effect on heat transfer of the computed variations of Pr_T with pressure gradient. some similar computations were made using equation 1.5. Refering to figure 53. it can be seen that the effect on temperature of the computed variations of Pr_T with streamwise pressure gradient is negligible. The change in the convective heat transfer coefficient is less than 1.5%.

Figures 41 and 42 show that for the cases of varying molecular Prandtl *number and pressure gradient the turbulent Prandtl* number is essentially a constant (0.9) throughout most of the viscous sublayer. The only region where this is not true is $y^- < 3$ and only at $Pr > 1.0$. Once again. the one-dimensional temperature analysis is employed to compare the temperature profiles using the computed Pr_T with those using a constant Pr_T of 0.9. Figures 54 and 55 show that. for Pr = 0.72 and Pr = 6.0. the temperature profiles for variable and constant Pr_T are very similar. with differences in the approximate heat transfer coefficient being less than 5%. This should not be surprising since the turbulent Prandtl number variations occur at a y^- well within the y^- shown earlier to give significant variations in the temperature profile (refer to chapter 2). For Pr = 6.0, this interface value was found to be at $y^- - 7.5$. For higher Pr. the interface value is even farther out.

It appears that the assumption of constant Pr_T = 0.9 across the viscous sublayer works very well for the Prandtl number range (0.72 − 6.0). Launder (1978) states that the assumption of constant turbulent Prandtl number with $Pr_T - 0.9$

46

yields good heat transfer results for a wide range of Pr from 0.6 to 2000. Since the model of constant turbulent Prandtl number gives temperature profiles which agree with the temperature profiles of the present model well within experimental uncertainty ($\approx 5\%$), it appears adequate in practical heat transfer computations to neglect the variations in Pr_T across the viscous sublayer.

§5.5 Effect of a Second Component in the v_e Boundary Condition

For one set of computations, a second component was added to the v_e boundary conditions to represent medium scale eddies (MSE). The v_e boundary condition was

$$v_e = -\beta_1 \sin(N_1 - \phi_{v1})T \sin\zeta - \sqrt{2(\beta^2 - \beta_1^2)} \sin(3N_{u2}T - \phi_{v2}) \sin(\frac{\zeta}{3}) \qquad (5.5)$$

This provides a more realistic value for $\frac{\beta_1}{\beta}$ which experimentally is measured to be about 0.6 (Ota and Chapman 1983). With only a SSE component it is forced to be 1.0. Additionally this second component allows for more free parameters for adjusting the computational values. When this model was run, however, problems with generated pressure waves were increased to the point where the temperature profile was severely affected in an unrealistic manner. The additional component aggravated the boundary condition problem at the outer edge. This seems to confirm the fact that the high pressure intensity is related to the oscillating v_e boundary condition. Additional MSE components were added to the other boundary conditions, u, w, and θ, to try to alleviate the severe pressure build-up. These additional components did not improve the temperature profile, and aggravated the pressure build-up. The energy boundary condition with an imposed oscillating v_e at the boundary would have to be improved before a more complex (realistic) v_e boundary condition can be applied.

§5.6 Solid-Fluid Interface Boundary Condition

Thus far an isothermal wall boundary condition has been employed, in part because of its simplicity in implementation and also because most theories and

47

experiments for turbulent heat transfer assume this boundary condition. Such a boundary condition is not exact in physical experiments. since wall temperature fluctuations can be measured (Meek and Baer 1973). Meek and Baer have concluded that that the wall temperature boundary condition is very important in determining turbulent heat transfer physics. For this reason a more complete specification of the solid-fluid temperature boundary condition was investigated. and used as implicit boundary conditions in the VSL computation. The conventional solid-fluid interface boundary conditions were used to see if the abnormally high temperature intensity peak was due to the imposition of the isothermal wall temperature boundary condition.

The solid-fluid boundary conditions for continuity of temperature and heat flux are

$$\theta(y^+ = 0)_{fluid} = \theta(y^+ = 0)_{solid} \qquad (5.6a)$$

$$k_{fluid} \frac{\partial \theta}{\partial y}(y^+ = 0)_{fluid} = k_{solid} \frac{\partial \theta}{\partial y}(y^+ = 0)_{solid} \qquad (5.6b)$$

With these boundary conditions. a stable algorithm similar to the present one was developed by Degani and Brosh (1983). This solid-fluid interface boundary condition was run with three different material interfaces: air-copper.air-glass. and water-copper. The computed values are reasonable compared to the experimentally measured values of θ'_u of Meek and Baer. however the values cannot be compared directly since their fluid was an oil (tetralin) which has a Pr number beyond the stable range for the present computational code. Meek and Baer had $\theta'_u \approx 0.2$ for their oil flow. The following table shows the values of θ'_u for the different interfaces.

Table 5.6

Values of θ'_u

Interface	θ'_u
air copper	0.027
air glass	0.053
water copper	0.142

It can be seen in figures 56(a)-56(c) that use of the solid-fluid interface condition does not have a major effect on the temperature intensity. Thus, wall temperature fluctuations seem to have only a very localized effect when compared to the isothermal results. The relatively high peak computed for temperature intensity, therefore, does not seem to be a consequence of the wall temperature boundary condition. Other turbulence terms involving temperature quantities are similarly unaffected in the region away from the wall in the presence of wall temperature fluctuations. The wall temperature fluctuations do not seem to have the importance that Meek and Baer have suggested. It is believed that the high temperature intensity is due to some unrealistic aspect of the outer boundary condition at $y^- = 40$ and not due to the isothermal wall temperature boundary condition.

6. Concluding Remarks

A two component model has been developed for computing the distribution of turbulent Prandtl number in the compressible viscous sublayer for flows of varying mean streamwise pressure gradient and varying molecular Prandtl number. The principal problem encountered involved finding a set of boundary conditions that yields stable numerical solutions without numerical decoupling. A comparison of computed results with available experiments has been made for the four quantities $(\overline{uv}, \overline{v\theta}, \frac{\partial \bar{u}}{\partial y}, \frac{\partial \bar{\theta}}{\partial y})$ that determine Pr_T. The agreement is satisfactory, although it is noted that data presently available for $\overline{v\theta}$ exist only near the outer edge of the viscous sublayer.

The range of values for the computed Pr_T is about in the middle of the wide range of predicted values of Pr_T from various experiments and existing theories. The theories of Thomas, Maksin and Geshev are qualitatively consistent with the present computed trends of the variations of Pr_T with molecular Pr. All the rest surveyed (6 theories) show differing trends.

There is a strong dependence of Pr_T on Pr near the wall ($y^+ < 3$), but the dependence of Pr_T on $\frac{\partial \bar{p}}{\partial x}$ is very slight throughout the viscous sublayer. For $y^+ > 3$, the turbulent Prandtl number is essentially a constant, in the range 0.9-1.0. The small effect of mean pressure gradient on Pr_T is consistent with the available experimental data. The behavior of computed Pr_T with pressure gradient agrees with the trend predicted by Thomas. The present computation agrees qualitatively with the computational model of Thomas both for the case of varying Prandtl number and pressure gradient.

Molecular Prandtl numbers between 0.7 and 6.0 affect the turbulent Prandtl number only in a region so close to the wall that the temperature profiles and heat transfer are essentially unaffected. In view of this, and of the small effect of streamwise pressure gradient on turbulent Prandtl number, the assumption of

50

constant $Pr_T = 0.9$ across the viscous sublayer appears adequate for practical computations of heat transfer.

It has been shown that the temperature profile and convective heat transfer coefficient computed using the present Pr_T model for both varying mean streamwise pressure gradient and molecular Prandtl number differ only slightly from the temperature profiles computed with the Pr_T model of Kays and Crawford. The small temperature-profile differences between the two models are somewhat larger for the cases of varying Pr than for varying pressure gradient.

A solid-fluid interface boundary condition was investigated in addition to an isothermal wall boundary condition to see if the wall temperature boundary condition was critical in determining the fluctuating temperature intensity. It was found the the solid-fluid interface condition produced wall temperature fluctuations as expected. however. their effect was not large and was very localized near the wall. Therefore. it is concluded that the wall temperature boundary condition is not a critical factor in determining the intensity of temperature fluctuations across the viscous sublayer.

The main problem encountered in developing the computational model stems from the numerical boundary condition for energy in the presence of an oscillating normal velocity at the outer edge boundary. If this problem can be fully resolved. a more versatile model could be developed using the present compressible-flow algorithm. The numerical problems encountered in this research are believed to be representative of those to be encountered when a compressible code is run at low Mach number and a central differencing algorithm is run without dissipation.

References

1 Antonia, R. A. (1980): Behavior of the Turbulent Prandtl near the wall. Int. J. Heat and Mass Transfer,23, pp. 906-908.

2 Antonia, R. A., Rajagopalan, S.,Subramanian, C. S., Chambers, A. J. (1982): Reynolds Numbers dependence of the structure of a turbulent boundary layer. J. F. M. ,121,pp. 123-140.

3 Back, L. H.,Cuffel, R. F.,Massier, P. F. (1970): Effect of Wall cooling on the mean structure of a turbulent boundary layer in low-speed gas flow. Int. J. Heat Mass Transfer,13, pp. 1029-1047.

4 Bayliss, A., Turkel, E. (1981): Far Field Boundary Conditions for Compressible Flows. Numerical Boundary Condition Procedures Symposium Oct. 19-20. 1981. NASA Conference Publication 2201, pp.1-19.

5 Beam, R. M., Warming, R. F. (1978): An Implicit Factored Scheme for the Compressible Navier-Stokes Equations. AIAA Journal, 16, pp. 393-402.

6 Beam, R. M., Warming, R. F.,Yee, H. C. (1978): Stability Analysis for Numerical Boundary Conditions and Implicit Difference Approximations of Hyperbolic Equations. Numerical Boundary Condition Procedures Symposium Oct. 19-20. 1981. NASA Conference Publication 2201, pp.1-19.

7 Blackwelder, R. F., Eckelmann, H. (1979): Streamwise Vortices Associated with the Bursting Phenomenon. J.F.M.,94, Pt. 3, pp. 577-594.

8 Blackwelder, R. F., Kaplan, R. E. (1976): On the Wall Structure of the Turbulent Boundary Layer. J.F.M., 76, Pt. 1, pp. 89-112.

9 Blackwell, B. F. (1972): The Turbulent Boundary Layer on a Porous Plate: An Experimental Study of the Heat Transfer Behavior with Adverse Pressure Gradients. Report HMT-16, Dept. of Mech. Eng., Stanford University.

10 Blom, J. (1970): Experimental Determination of the turbulent Prandtl Number in a developing boundary layer. Proc. IV Int. Heat Transfer Conf. Paris.

11. Bradshaw, P. (1967): "Inactive" Motions and Pressure Fluctuations in Turbulent Boundary Layers. J.F.M.,30,Pt. 2, pp. 241-258.

12. Cantwell, B.J. (1981): Organized Motion in Turbulent Flow. Ann. Rev. Fluid Mech., 13, pp. 457-515.

13. Cebeci, T. (1973): A Model for Eddy Conductivity and Turbulent Prandtl Number. Jour. Heat Transfer,95,pp. 227-234.

14. Chapman, D. R. (1980): Trend and Pacing Items in Computational Aerodynamics. Lecture Notes in Physics, Springer-Verlag,141, pp. 1-11.

15. Chapman, D. R., Kuhn, G. D. (1981): Two-component Navier-Stokes Computational Model of Viscous Sublayer Turbulence. AIAA Fifth CFD Conf. Palo Alto, CA, Paper 81-1024.

16. Chen, C. P., Blackwelder, R. F. (1978): Large scale motion in a turbulent boundary layer: a study using temperature contamination. J.F.M., 89, Pt. 1. pp. 1-31.

17. Chen, C. P. (1973): Determination Experimentale du Nombre de Prandtl Turbulent Pres D'une Paroi Lisse. Int. J. Heat Mass Transfer, 16, pp. 1849-1862.

18. Cheng, R. K., Ng, T. T. (1982): Some aspects of strongly heated turbulent boundary layer flow. Phys. Fluids, 25, pp. 1333-1341.

19. Coles, D. (1978): A model for the Viscous Sublayer. AFOSR/Leigh Univ. Workshop, pp.462-475.

20. Degani, D., Brosh, A. (1983): Numerical Simulation of a Compressible Turbulent Boundary Layer over a Conductive Wall with Line Heat Source. Computers and Fluids,11, pp. 85-93.

21. Dinkelacker, A., Langeheineken, Th. (1982): Relations Between Wall Pressure Fluctuations and Velocity Fluctuations in Turbulent Flow. Structure of Complex Turbulent Shear Flow. IUTAM Symposium Marseille 1982, pp. 1-9.

22 Elena. M. (1977): Etude Experimentale de la turbulence Au voisinage de la Paroi d'un tube legerement chauffe. Int. J. Heat Mass Transfer,20, pp. 935-944.

23 Elena. M., Fulachier, L.,and Dumas, R. (1979): Etude Experimentale des Apports et des Ejections de Fluid Dans une Couche Limite Turbulent. AGARD CPP271, pp. 2-1 - 2-21. Transfer,20,pp. 935-944.

24 Fulachier, L., Antonia, R. A. (1984): Spectral Analogy between Temperature and Velocity Fluctuations in several Turbulent Flows. Int. J. Heat Mass Transfer,27, pp. 987-997.

25 Fulachier, L. (1972): Contribution a L'Etude des Analogies des Champs Dynamique et Thermique dans une Couche Limite Turbulent. Effet de L'Aspiration. Thesis, University of Provence, France.

26 Geshev. P. I. (1978): Influence of Heat Conduction of the wall on the turbulent Prandtl Number in the viscous sublayer. Inzhenerno-Fizicheskii Zhurnal,35. pp. 292-296.

27 Hinze. J. O. (1975): Turbulence. McGraw-Hill, pp. 586-770.

28 Gibson. M. M., Verriopoulos, C. A., and Nagano, Y. (1981): Measurements in the Heated Turbulent Boundary Layer on a Mildly Curved Convex Surface. Turbulent Shear Flow, Third Int. Symp., pp. 80-89.

29 Gupta. A. K., Kaplan, R. E. (1972): Statistical Characteristics of Reynolds Stress in a Turbulent Boundary Layer. Phys. Fluids, 15. No. 6, pp. 981-985.

30 Hatziavramidis. D. T., Hanratty, T. J. (1979): The Representation of the Viscous Wall Region by a Regular Eddy Pattern. J.F.M.,95,Pt. 4, pp. 655-679.

31 Hishida. M., Nagano, Y. (1978): Simultaneous Measurements of Velocity and Temperature in Nonisothermal flows. Jour. of Heat Transfer, 100. pp. 340-345.

54

32 Hishida, M., Nagano, Y. (1979): Structure of Turbulent Velocity and Temperature fluctuations in fully developed Pipe Flow. Jour. of Heat Transfer, 101, pp. 15–22.

33 Iritani, Y., Kasagi, N., Nagano, H. (1981): Transport Mechanism in a Turbulent Boundary Layer– Visualized Behavior of Wall Temperature be Liquid Crystal. Submitted to Trans JSME (B).

34 Iritani, Y.,Kasagi, N., Hirata, M. (1983): Heat Transfer Mechanism and Associated Turbulence Structure in the Near Wall Region of a Turbulent Boundary layer. Fourth Symposium Turbulent Shear Flows, pp. 17.31–17.36.

35 Jischa, M.,Rieke H. B. (1978): Turbulent Heat Transfer in Duct flow. Sixth Int. Heat Transfer Conf., pp. 543–548.

36 Jischa, M., Rieke, H. B. (1979): About the Prediction of turbulent Prandtl and Schmitt Numbers for Modelled Transport equations. Int. J. Heat Mass Transfer, 22, pp.1547–1555.

37 Johansson, A. V., Alfredsson, D. H. (1982): On the structure of turbulent channel flow. J. F. M., 122,pp. 295–314.

38 Johnson, D. S. (1959): Velocity and Temperature fluctuation Measurements in a Turbulent Boundary Layer Downstream of a Stepwise Discontinuity in Wall Temperature. Jour. Appl. Mech.,pp. 325–336.

39 Johnk. R. E., Hanratty, T. J. (1982): Temperature Profiles for Turbulent Flow of air in a pipe. Chem. Eng. Sci.,17,pp. 867–881.

40 Kader, B. A. (1981): Temperature and Concentration Profiles in fully turbulent boundary layers. Int. J. Heat Mass Transfer, 24. pp. 1541–1544.

41 Kays, W. M., Moffat, R. J. (1975): The Behavior of Transpired Turbulent Boundary Layers. Studies in Convection,Vol. 1,pp 223–319.

42 Kays, W. M., Crawford, M. E. (1980): Convective Heat and Mass Transfer. McGraw-Hill, pp. 204-234.

43 Kearney, D. W., Kays, W. M.,Moffat, R. J. (1973): Heat Transfer to a strongly accelerated Turbulent Boundary layer: some experimental results including transpiration. Int. J. Heat Mass Transfer,16,pp.1289-1305.

44 Khabakhpasheva, E. M.,Perepelitsa, B. V. (1974): Measurements of Temperature, Velocity fields and Turbulent Prandtl Number in Near-wall flow region. Fifth Int. Heat Transfer Conf. Tokyo, pp. 134-136.

45 Kim, J. (1982): On the Structure of Wall Bounded Turbulent Flows. Paper presented at Amer. Phys. Soc. Div. Fluid Dyn. Meeting, Rutgers Univ., Nov. 21-23, 1982.

46 Kim, J. (1984): Vortical Structures Associated with the Bursting Event. APS Abstract no. AH 1, Paper presented at Amer. Phys. Soc. Div. Fluid Dyn. Meeting, Brown Univ., Nov. 18-20, 1984.

47 Kim, H. T., Kline, S. J., Reynolds, W. C. (1971): The Production of Turbulence Near a Smooth Wall in a Turbulent Boundary Layer. J.F.M.,50,Pt. 1,pp.133-160.

48 Kreplin, H. P.,Eckelmann, H. (1979): Behavior of the three fluctuating velocity components in the wall region of a turbulent channel flow. Phys. Fluids,22, pp. 1233-1239.

49 Landau, L. D., Lifshitz, E. M. (1959): Fluid Mechanics. Course of Theoretical Physics,6,Pergamon Press,pp.523-529.

50 Laufer, J. (1950): Investigation of Turbulent Flow in a Two-Dimensional Channel. NACA TN 2123.

51 Laufer, J. (1953): The Structure of Turbulence in Fully Developed Pipe Flow. NACA TN 2954.

52 Launder, B. E. (1978): Heat and Mass Transport. Topics in Applied Physics, 12, Springer-Verlag,pp. 231-287.

53 Maksin, P. L., Petukhov, B. S., and Polyakov, A. F. (1977): Calculation of Turbulent Eddy Heat Transfer in Stabilized Pipe Flow. Heat Transfer-Soviet Research. 9, pp. 1-10.

54 McEligot, D. M., Pickett, P. E.,Taylor, M. F. (1976): Measurement of Wall region Turbulent Prandtl Numbers in small tubes. Int. J. Heat Mass Transfer, 19, pp. 799-803.

55 Meek, R. L.,Baer, A. D. (1973): The Periodic Viscous Sublayer in Turbulent Flow. Int. J. Heat Mass Transfer, 16, pp. 841-848.

56 Meek, R. L.,Baer, A. D. (1973): Turbulent Heat Transfer and the Periodic Viscous Sublayer. Int. J. Heat Mass Transfer, 16, pp. 1385-1396.

57 Mizushina, T.,Ito, R.,Ogino F. (1970): Eddy Diffisivity near the wall. Proc. IV Int. Heat Transfer Conf. Paris.

58 Meroney, R. N. (1968): Turbulent Sublayer Temperature Distribution including wall injection and Dissipation. Int J. Heat Mass Transfer, 11,pp. 1406-1408.

59 Moser. R. (1984): Near Wall Structures in Curved Turbulent Channel Flow. APS Abstract no. BB 5. Paper presented at Amer. Phys. Soc. Div. Fluid Dyn. Meeting. Brown Univ., Nov. 18-20, 1984.

60 Nakagawa. H.,Nezu. I. (1981): Structure of space-time correlations of bursting phenomena in an open-channel flow. J. F. M., 104, pp. 1-43.

61 Offen. G. R., Kline, S. J. (1974): Combined Dye-Streak and Hydrogen Bubble Visual Observations of a Turbulent Boundary Layer. J.F.M.,62,Pt. 2,pp. 223-239.

62 Ohji. M. (1967): Statistical Theory of Wall Turbulence. Phys. Fluids, 10, pp. S153-S154.

63 Ota. D.. Chapman , D. R. (1983): Coherent Structure Modeling of Viscous Sublayer Turbulence for Incompressible Flow with Heat Transfer and for

Compressible Flow. Second Annual Scientific Report, AFOSR Contract No. 81-NA-256.

64 Pereplitsa. B. V.,Khabakhpasheva. Y. M. (1981): Correlations between Temperature and Velocity fluctuations in the wall region of turbulent flow. Heat Transfer,13, pp. 46-55.

65 Popovich. A. T. (1969): Statistical Analysis of fluid flow fluctuations in the viscous layer near a solid wall. I&EC Fundamentals,8, pp. 609-614.

66 Popovich. A. T.,Hummel, R. L. (1967): Experimental Study of the Viscous Sublayer in Turbulent Pipe flow. AIChE Journal, pp. 854-860

67 Pulliam. T. H., Steger. J. L. (1980): Implicit Finite Difference Simulations of Three-Dimensional Compressible Flow. AIAA Journal,18, pp. 149-158.

68 Reynolds. A. J. (1975): The Prediction of Turbulent Prandtl and Schmidt Numbers. Int. J. Heat and Mass Transfer,18, pp. 1055-1069.

69 Rotta. J. C.. (1964): Temperaturverteilungen in der turbulenten Grenzschicht an der ebenen Platte. Int. J. Heat and Mass Transfer,7, pp. 215-228.

70 Schildnecht. M., Miller, J. A., Meier. G. E. A. (1979): The Influence of Suction on the Structure of Turbulence in Fully Developed Pipe Flow. J.F.M., 90. Pt. 1, pp. 67-107.

71 Schlichting. H. (1979): Boundary Layer Theory. McGraw-Hill. pp. 706-724.

72 Schraub. F. A., Kline, S. J. (1965): A Study of the Structure of the Turbulent Boundary Layer with and without Longitutinal Pressure Gradients. Thermosciences Div. Report MD-12, Stanford University.

73 Simon. T. W., Moffat. R. J. (1982): Convex Curvature Effects on the Heated Turbulent Boundary Layer. Heat Transfer 1982 Proc. of the Seventh Int. Heat Transfer Conf.. Vol. 3. pp. 295-300.

74 Simonek. J. (1983): A Model of Eddy Viscosity and Eddy Diffusivity. Int. J. Heat and Mass Transfer.26. pp. 479-508.

75 Simpson, R. L. (1970): Characteristics of turbulent boundary layers at low Reynolds numbers with and without transpiration. J. F. M.,42,part 4, pp. 769-802.

76 Simpson, R. L.,Whitten, D. G.,Moffat, R. J. (1973): An experimental study of the turbulent Prandtl Number of air with injection and suction. Int. J. Heat Mass Transfer, 13, pp. 123-143.

77 Smith, C. R., Schwartz S. P. (1983): Observation of streamwise rotation in the near-wall region of a turbulent boundary layer. Phys. Fluids, 26, pp.641-652.

78 Smith, C. R., Metzler, S. P. (1983): The Characteristics of low-speed streaks in the near-wall region of a turbulent boundary layer. J. F. M.,129, pp. 27-54.

79 Snijders, A. J., Koppius, A. M., Nieuwvelt C. (1983): An Experimental Determination of the Turbulent Prandtl Number in the Inner Boundary Layer for Air Flow over a flat plate. Int. J. Heat and Mass Transfer,26, pp. 425-431.

80 Subramanian, C. S.,Antonia R. A. (1981): Effect of Reynolds Number on a slightly Heated turbulent boundary layer. Int. J. Heat and Mass Transfer,24, pp. 1833-1846.

81 Tennekes, H., Lumley, J. L. (1972): A First Course in Turbulence, MIT Press, pp.50-52.

82 Tien, C. L.,Wasan, D. T. (1963): Law of the Wall in Turbulent Channel flow. Phys. Fluids,6,pp.144-145.

83 Thomas, L. C. (1981): A Model of the Turbulent Burst Phenomena: Predictions for turbulent Prandtl Number.Letters in Heat and Mass Transfer,8,pp. 357-369.

84 Thomas, L. C. (1982): A Turbulent Burst Model for Energy Transfer in the wall region. Heat Transfer 1982 Proc. of the Seventh Int. Heat Transfer Conf.. Vol. 3, pp. 307-312.

85 Thomas, L. C.. Benton D. J. (1982): A Turbulent Burst Model for Boundary Layer Flows with Pressure Gradient. Heat Transfer 1982 Proc. of the Seventh Int. Heat Transfer Conf., Vol. 3, pp. 313-318.

86 Townsend, A. A. (1976): The Structure of Turbulent Shear Flow. Cambridge Univ. Press. pp. 334-392.

87 Townsend, A. A. (1961): Equilibrium Layers and Wall Turbulence. Journal of Fluid Mechanics ,11.pp. 97-120.

88 Ueda, H.. Hinze, J. O. (1975): Fine Structure Turbulence in the Wall Region of a Turbulent Boundary Layer. J.F.M.,67, Pt. 1, pp. 125-143.

89 Wallace. J. M.. Eckelmann. H., Brodkey, R. S. (1972): The Wall Region in Turbulent Flow. J.F.M.,54,Pt. 1, pp. 39-48.

90 Wassel. A. T.. Catton, I. (1973): Calculation of Turbulent Boundary layers over flat plates with different phenomenological theories of turbulence and variable turbulent Prandtl Number. Int. J. Heat Mass Transfer,16. pp. 1547-1563.

APPENDIX I

DECOMPOSITION OF JACOBIAN AND VISCOUS MATRICES

The Jacobian and viscous matrices $(\hat{B} - J^{-1}\hat{B}_v J) = \partial \hat{F} / \partial q - \partial \hat{F}_v / \partial q$ and $(\hat{C} - J^{-1}\hat{C}_v J) = \partial \hat{G} / \partial q - \partial \hat{G}_v / \partial q$ obtained in the time linearization of $\hat{F} - \hat{F}_v$ and $\hat{G} - \hat{G}_v$ are each decomposed into two matrices, one (subcript 0) that does not contain any cross derivative terms and another(subcript x) that contains all such terms.

$$(\hat{B} - J^{-1}\hat{B}_v J) = A_0 + A_x$$

$$(\hat{C} - J^{-1}\hat{C}_v J) = B_0 + B_x$$

The matrix A_0 is

$$A_0 = - \begin{pmatrix} 0 & 0 & 0 & \eta_y & 0 \\ -\eta_y uv & \eta_y v & \eta_y u & 0 & 0 \\ \eta_y(\phi^2 - v^2) & -\eta_y(\gamma-1)u & -\eta_y(\gamma-3)v & -\eta_y(\gamma-1)w & \eta_y(\gamma-1) \\ -\eta_y vw & 0 & \eta_y w & \eta_y v & 0 \\ \eta_y v \left(2\phi^2 - \gamma\frac{e}{\rho}\right) & \eta_y(\gamma-1)uv & \alpha_1 & -\eta_y(\gamma-1)vw & \eta_y\gamma v \end{pmatrix}$$

$$-J^{-1} \begin{pmatrix} 0 & 0 & 0 & 0 & 0 \\ -s_1\delta_\eta(\frac{u}{\rho}) & s_1\delta_\eta(\frac{1}{\rho}) & 0 & 0 & 0 \\ -s_2\delta_\eta(\frac{v}{\rho}) & 0 & s_2\delta_\eta(\frac{1}{\rho}) & 0 & 0 \\ -s_1\delta_\eta(\frac{w}{\rho}) & 0 & 0 & s_1\delta_\eta(\frac{1}{\rho}) & 0 \\ \alpha_2 & (s_1-s_5)\delta_\eta(\frac{u}{\rho}) & (s_2-s_5)\delta_\eta(\frac{v}{\rho}) & (s_1-s_5)\delta_\eta(\frac{w}{\rho}) & s_5\delta_\eta(\frac{1}{\rho}) \end{pmatrix} J$$

with

$$\alpha_1 = -\eta_y(\gamma-1)v^2 + \eta_y\left(\gamma\frac{e}{\rho} - \phi^2\right)$$

$$\alpha_2 = (s_5-s_1)\delta_\eta\left(\frac{u^2 + w^2}{\rho}\right) + (s_5-s_1)\delta_\eta\left(\frac{v^2}{\rho}\right) - s_5\delta_\eta\left(\frac{e}{\rho^2}\right)$$

$$\phi^2 = .5(\gamma-1)(u^2 + v^2 + w^2)$$

$$s_1 = \mu\eta_y^2 \quad s_2 = \frac{4}{3}s_1 \quad s_5 = \frac{\gamma}{Pr}s_1$$

61

$$J = Jacobian = \frac{1}{\Delta y^+ \Delta z^+}$$

and the matrix A_x is

$$A_x = J^{-1} \begin{pmatrix} 0 & 0 & 0 & 0 & 0 \\ 0 & 0 & 0 & 0 & 0 \\ -s_4\delta_\varsigma(\frac{u}{\rho}) & 0 & 0 & s_4\delta_\varsigma(\frac{1}{\rho}) & 0 \\ -s_3\delta_\varsigma(\frac{v}{\rho}) & 0 & s_3\delta_\varsigma(\frac{1}{\rho}) & 0 & 0 \\ \alpha_3 & 0 & [s_4\frac{1}{\rho}\delta_\varsigma w + s_3 w\delta_\varsigma(\frac{1}{\rho})] & [s_4 v\delta_\varsigma\frac{1}{\rho} + s_3\frac{1}{\rho}\delta_\varsigma v] & 0 \end{pmatrix} J$$

with

$$\alpha_3 = -s_3[\frac{w}{\rho}\delta_\varsigma v - w\delta_\varsigma(\frac{v}{\rho})] - s_4[\frac{v}{\rho}\delta_\varsigma w + v\delta_\varsigma(\frac{w}{\rho})]$$

$$s_3 = \mu\eta_y\varsigma_z \quad s_4 = -\frac{2}{3}s_3$$

The matrix B is

$$B \begin{pmatrix} 0 & (& 0 & \varsigma_z & 0 \\ -\varsigma_z u w & \varsigma_z w & 0 & \varsigma_z u & 0 \\ \varsigma_z v w & 0 & \varsigma_z w & \varsigma_z v & 0 \\ \varsigma_z(\sigma^2 - w^2) & -\varsigma_z(\gamma-1)u & -\varsigma_z(\gamma-1)v & -\varsigma_z(\gamma-3)w & \varsigma_z(\gamma-1) \\ w \cdot 2\sigma^2 - \gamma\frac{\epsilon}{\rho} & -\varsigma_z(\gamma-1)uw & -\varsigma_z(\gamma-1)vw & \alpha_4 & \varsigma_z\gamma w \end{pmatrix}$$

$$-J^{-1} \begin{pmatrix} 0 & 0 & 0 & 0 & 0 \\ -t_1\delta\cdot(\frac{u}{\rho}) & t_1\delta\cdot(\frac{1}{\rho}) & 0 & 0 & 0 \\ -t_1\delta\cdot(\frac{v}{\rho}) & 0 & t_1\delta_\varsigma(\frac{1}{\rho}) & 0 & 0 \\ -t_2\delta\cdot(\frac{w}{\rho}) & 0 & 0 & t_2\delta_\varsigma(\frac{1}{\rho}) & 0 \\ \alpha_5 & (t_1-t_5)\delta\cdot(\frac{u}{\rho}) & (t_1-s_5)\delta\cdot(\frac{v}{\rho}) & (t_2-s_5)\delta_\varsigma(\frac{w}{\rho}) & t_5\delta_\varsigma(\frac{1}{\rho}) \end{pmatrix} J$$

with

$$\alpha_4 = -\varsigma_z(\gamma-1)w^2 + \varsigma_z\gamma\frac{e}{\rho} - \phi^2$$

62

$$\alpha_5 = (t_5 - t_1)\delta_\varsigma \frac{u^2 - v^2}{\rho} + (t_5 - t_1)\delta_\varsigma(\frac{w^2}{\rho}) - t_5\delta_\varsigma(\frac{e}{\rho^2})$$

$$t_1 = \mu\varsigma_y^2 \quad t_2 = \frac{4}{3}t_1 \quad t_5 = \frac{\gamma}{Pr}t_1$$

and the matrix B_x is

$$B_x = J^{-1} \begin{pmatrix} 0 & 0 & 0 & 0 & 0 \\ 0 & 0 & 0 & 0 & 0 \\ -s_3\delta_\eta(\frac{w}{\rho}) & 0 & 0 & s_3\delta_\eta(\frac{1}{\rho}) & 0 \\ -s_4\delta_\eta(\frac{v}{\rho}) & 0 & s_4\delta_\eta(\frac{1}{\rho}) & 0 & 0 \\ \alpha_6 & 0 & [s_3\frac{1}{\rho}\delta_\eta w - s_4 w\delta_\eta(\frac{1}{\rho})] & [s_3 v\delta_\eta\frac{1}{\rho} - s_4\frac{1}{\rho}\delta_\eta v] & 0 \end{pmatrix} J$$

with

$$\alpha_6 = s_4[\frac{w}{\rho}\delta_\eta v - w\delta_\eta(\frac{v}{\rho})] - s_3[\frac{v}{\rho}\delta_\eta w + v\delta\eta(\frac{w}{\rho})]$$

APPENDIX II

Temperature Solution for
Oscillating Shear Flow

An exact analytical solution has been derived for oscillating shear flow (OSF) with heat transfer in an incompressible fluid with constant properties. Since the momentum equations are independent of the thermal energy equation in incompressible flow, the velocity field is the same as for the case without heat transfer derived by Chapman and Kuhn (1981). With y as the coordinate normal to the infinite flat surface. and u and v as the velocity components in the streamwise and spanwise directions. respectively, we have

$$u = A\left[\sin nt - e^{-k_n y}\sin(nt - k_n y)\right] + cy$$

$$w = B\left[\sin(mt - \phi) - e^{-k_m y}\sin(mt - k_m y)\right]$$

where

$$k_n = \sqrt{\frac{n}{2\imath}} \qquad k_m = \sqrt{\frac{m}{2\nu}}$$

The oscillating frequencies are n in the streamwise direction and m in the spanwise direction. and the mean velocity profile is $\bar{u} = cy$. For this velocity field, the solution to the thermal energy equation

$$\rho c_1 \frac{\partial \theta}{\partial t} = k\frac{\partial^2 \theta}{\partial y^2} + \mu\left[\left(\frac{\partial u}{\partial y}\right)^2 + \left(\frac{\partial v}{\partial y}\right)^2\right]$$

is

$$\theta(y.t) = B_1 y^2 + C_1 y + C_2 - B_2 e^{-2k_n y} - B_3 e^{-2k_m y}$$
$$+ A_2 e^{-k_n y}\left[\sin(nt - k_n y) - \cos(nt - k_n y)\right] - A_3 e^{-2k_n y}\cos 2(nt - k_n y)$$
$$+ A_4 e^{-2k_m y}\cos 2(mt - \phi - k_m y) - A_2 e^{-\beta_1 y}\sin(nt - \beta_1 y)$$
$$- A_2 e^{-\beta_1 y}\cos(nt - \beta_1 y) + A_3 e^{\beta_2 y}\cos(2nt - \beta_2 y)$$
$$+ A_4 e^{-\beta_3 y}\cos(2mt - 2\phi - \beta_3)$$

64

with

$$\beta_1 = \sqrt{\frac{n}{2\nu}Pr} \quad \beta_2 = \sqrt{\frac{n}{\nu}Pr} \quad \beta_3 = \sqrt{\frac{m}{\nu}Pr}$$

$$B_1 = -\frac{Prc^2}{2c_p} \quad A_2 = \frac{2cAk_n}{c_pRe(n - \frac{2k_n^2\nu}{Pr})}$$

$$B_2 = -A^2\frac{Pr}{4c_p} \quad A_3 = \frac{A^2k_n^2}{c_pRe(2n - \frac{8k_n^2\nu}{Pr})}$$

$$B_3 = -\beta^2\frac{Pr}{4c_p} \quad A_4 = \frac{B^2k_m^2}{c_pRe(2m - \frac{8k_m^2\nu}{Pr})}$$

$$C_1 = \frac{1}{y_e}\theta_\infty - C_2 + \frac{Prc^2y_e^2}{2c_p}$$

$$C_2 = \theta_w - \frac{Pr(A^2 - B^2)}{4c_p}$$

65
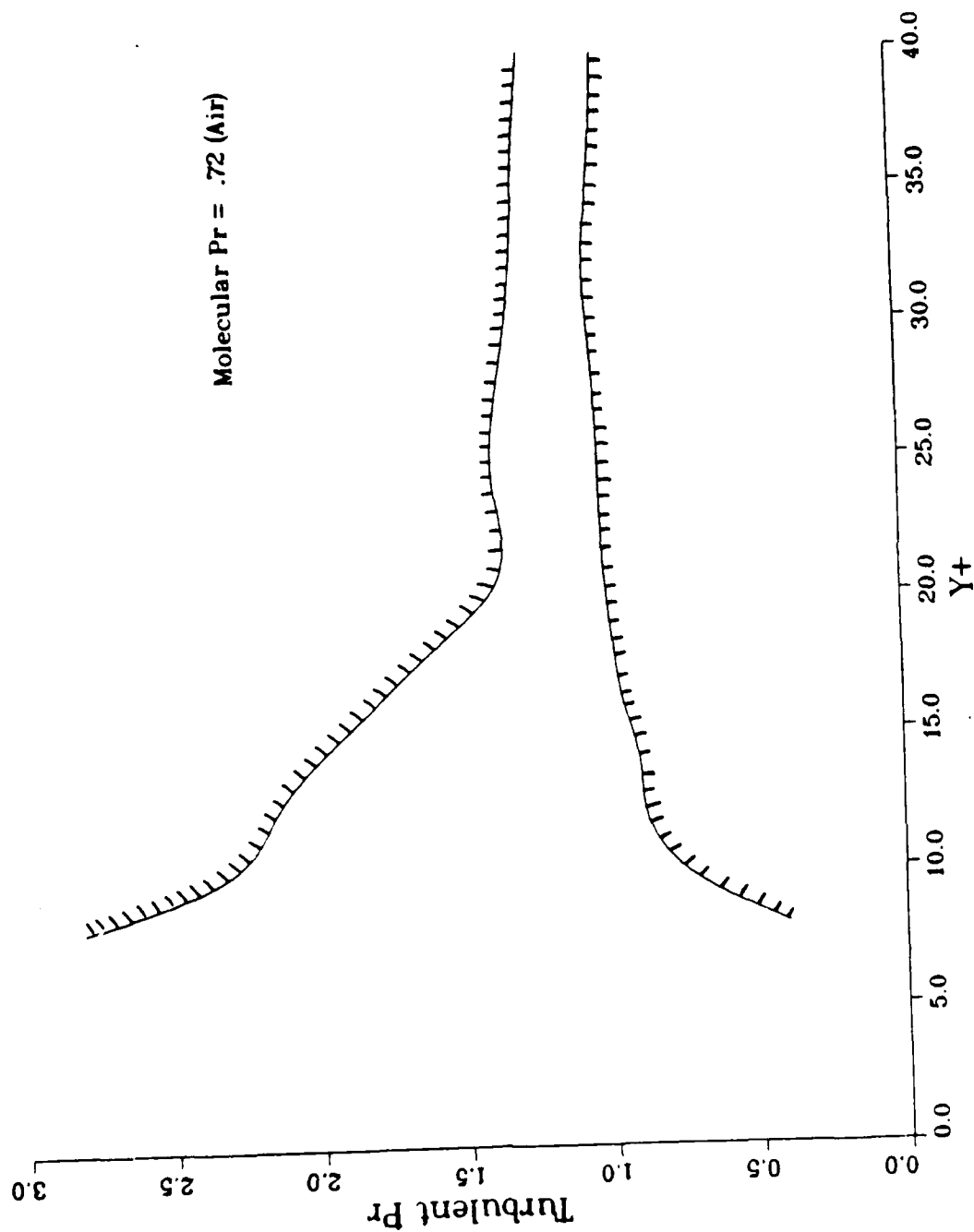
Figure 1 Experimental uncertainty envelope for the turbulent Prandtl number for Pr 0.72 (Air) and zero pressure gradient. From paper by Simpson, et.al. 1969.
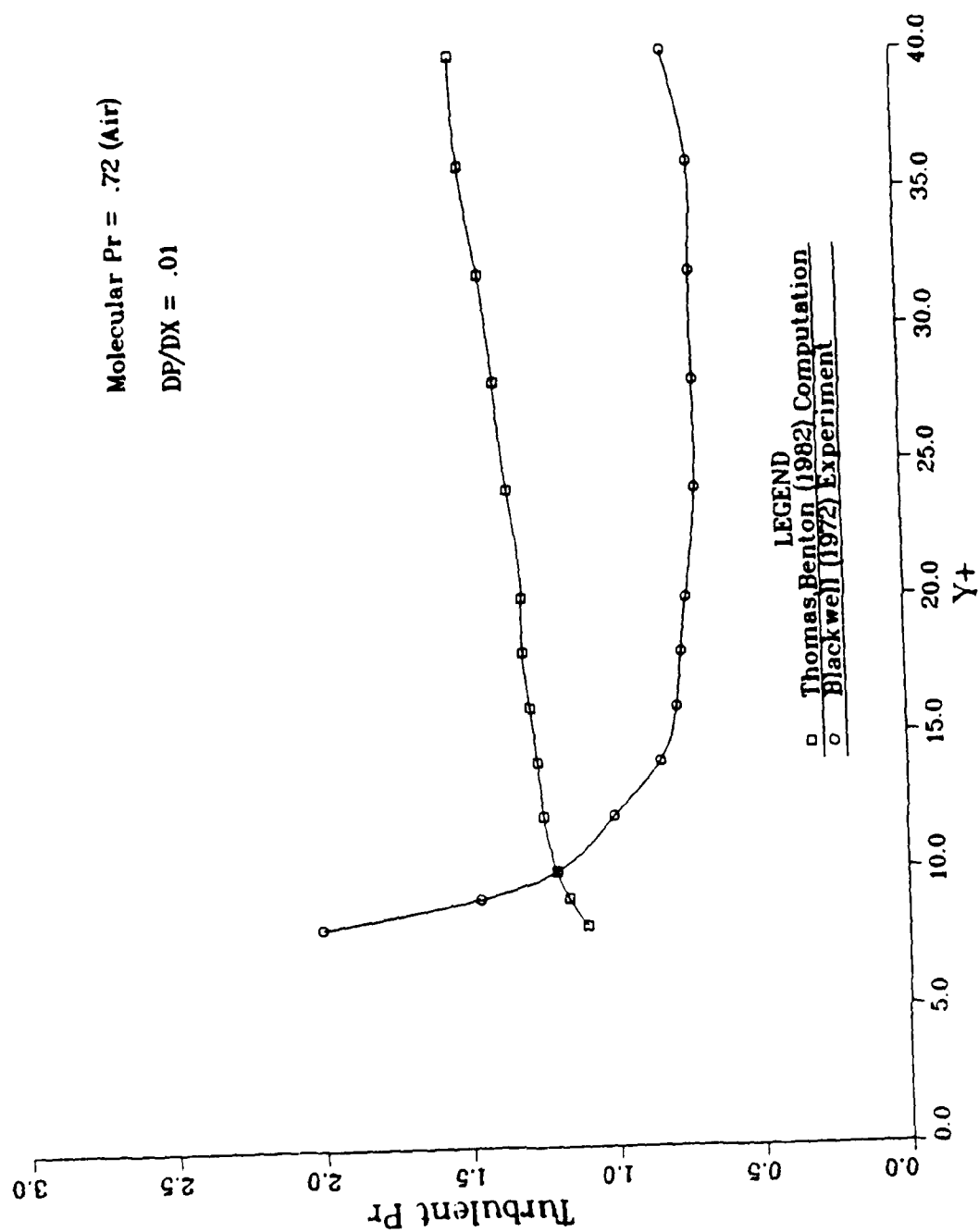
Figure 2 A computed and an experimental representation of the turbulent Prandtl number

for $Pr = 0.72$ (Air) with an adverse pressure gradient. $|(\frac{dp}{dx})^+ = .01|$.
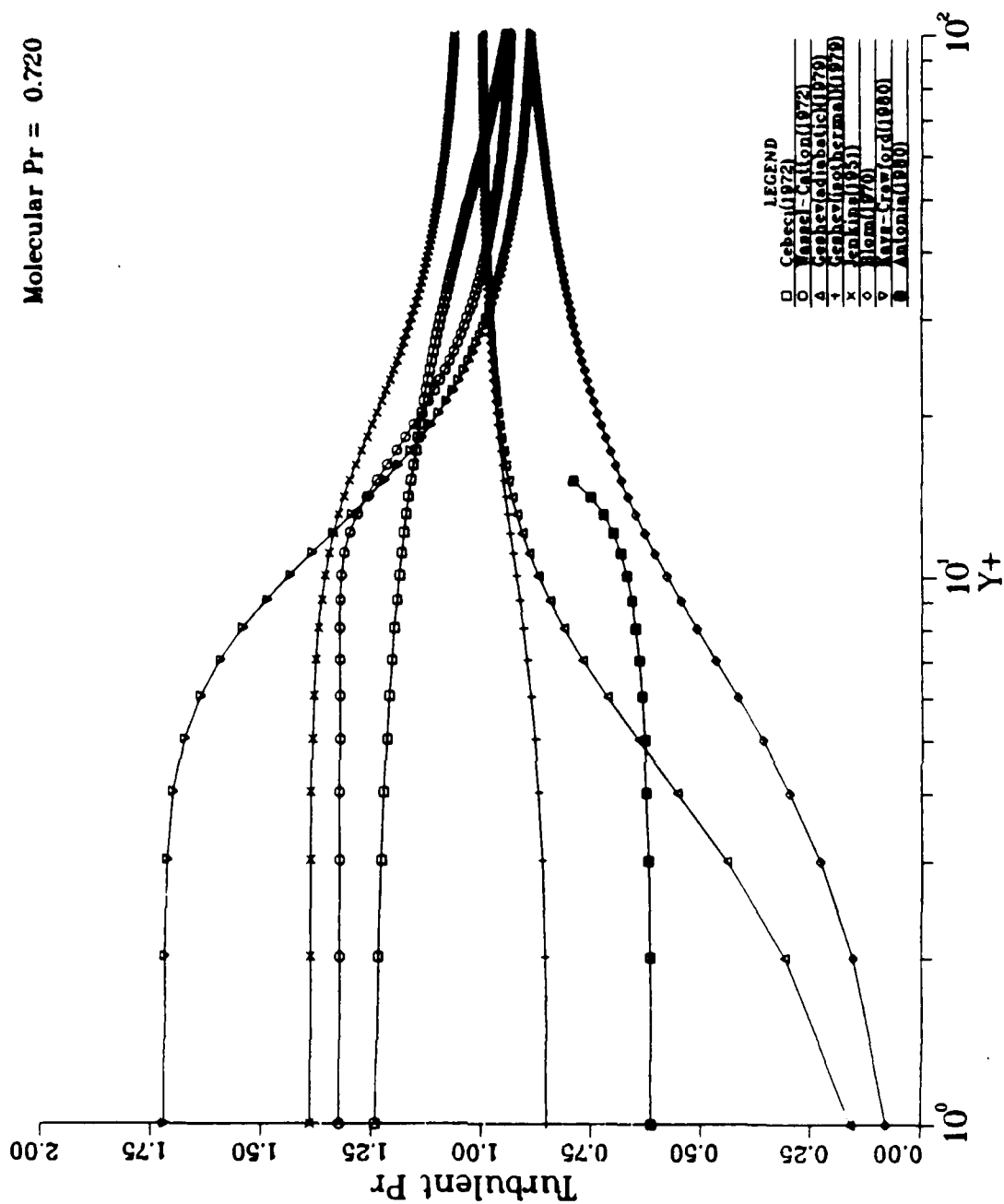
Figure 3 Theoretical uncertainty envelope for the turbulent Prandtl number for $Pr = 0.72$ (Air) and zero pressure gradient. Eight models for Pr_T shown.

68

Molecular Pr = 6.000
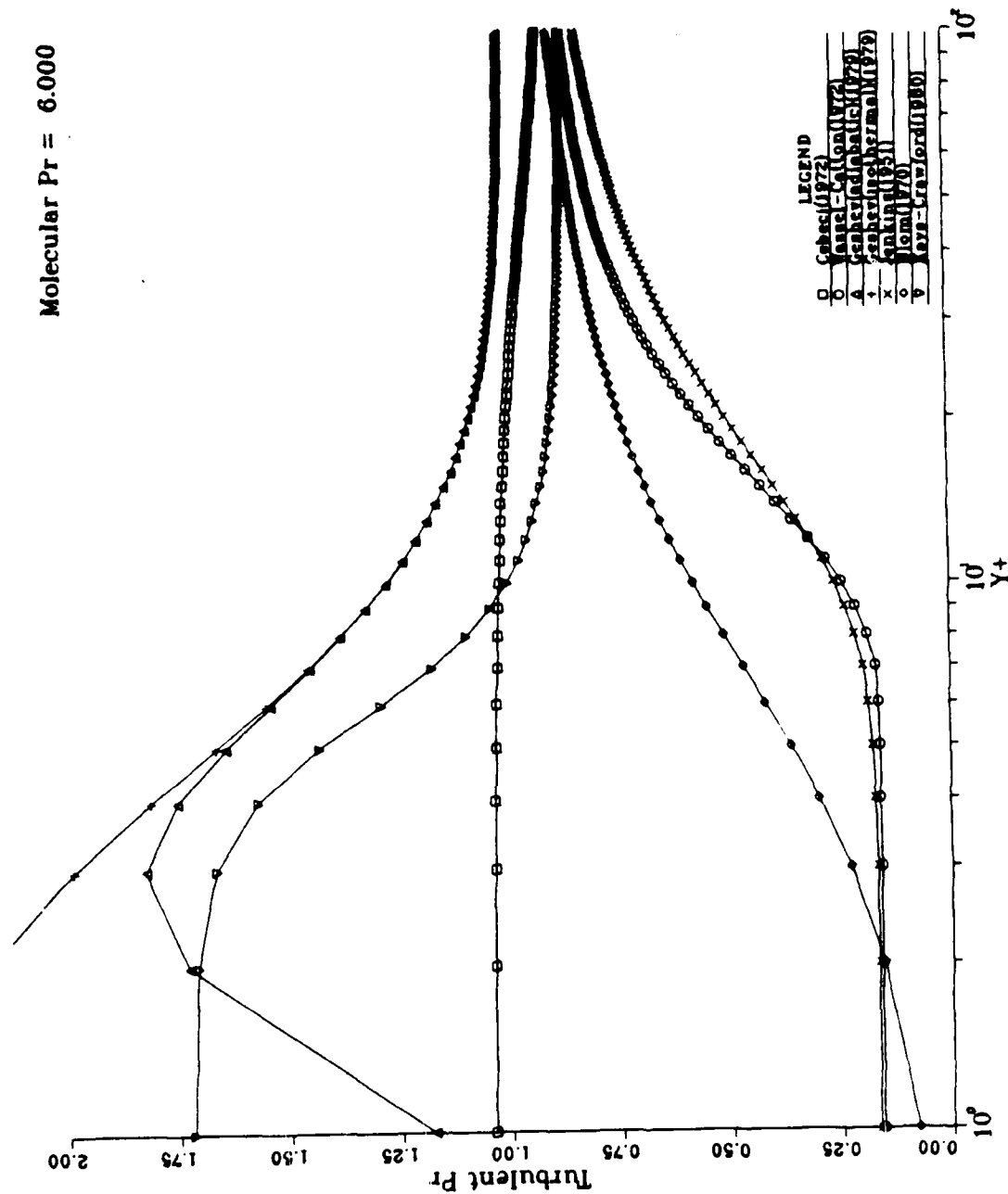
Figure 4 Theoretical uncertainty envelope for the turbulent Prandtl number for $Pr = 6.0$ (Water) and zero pressure gradient. Seven models for Pr_T shown.

69
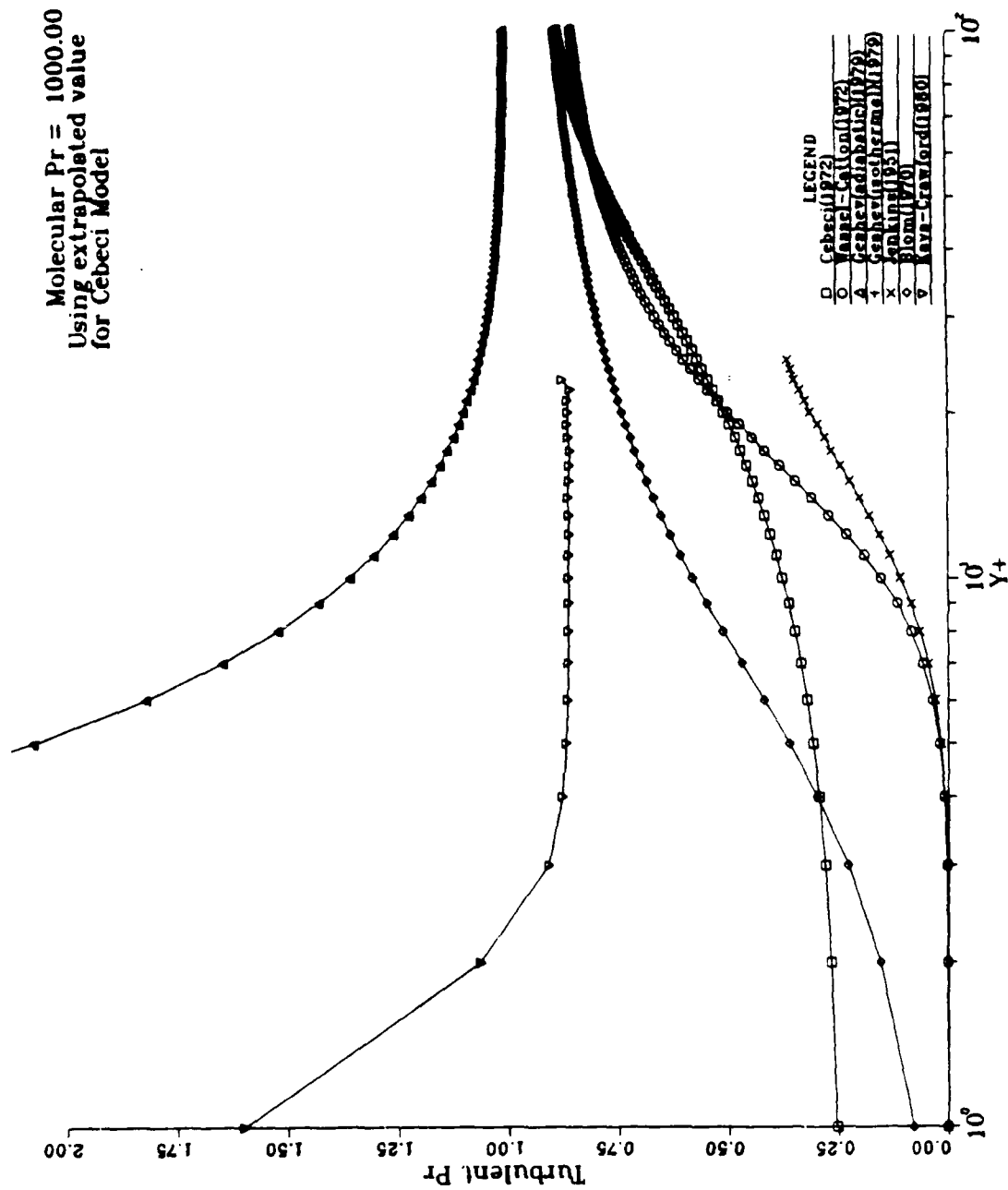
Figure 5 Theoretical uncertainty envelope for the turbulent Prandtl number for $Pr =$ 1000.0 (Oil) and zero pressure gradient. Seven models for Pr_T shown.

70
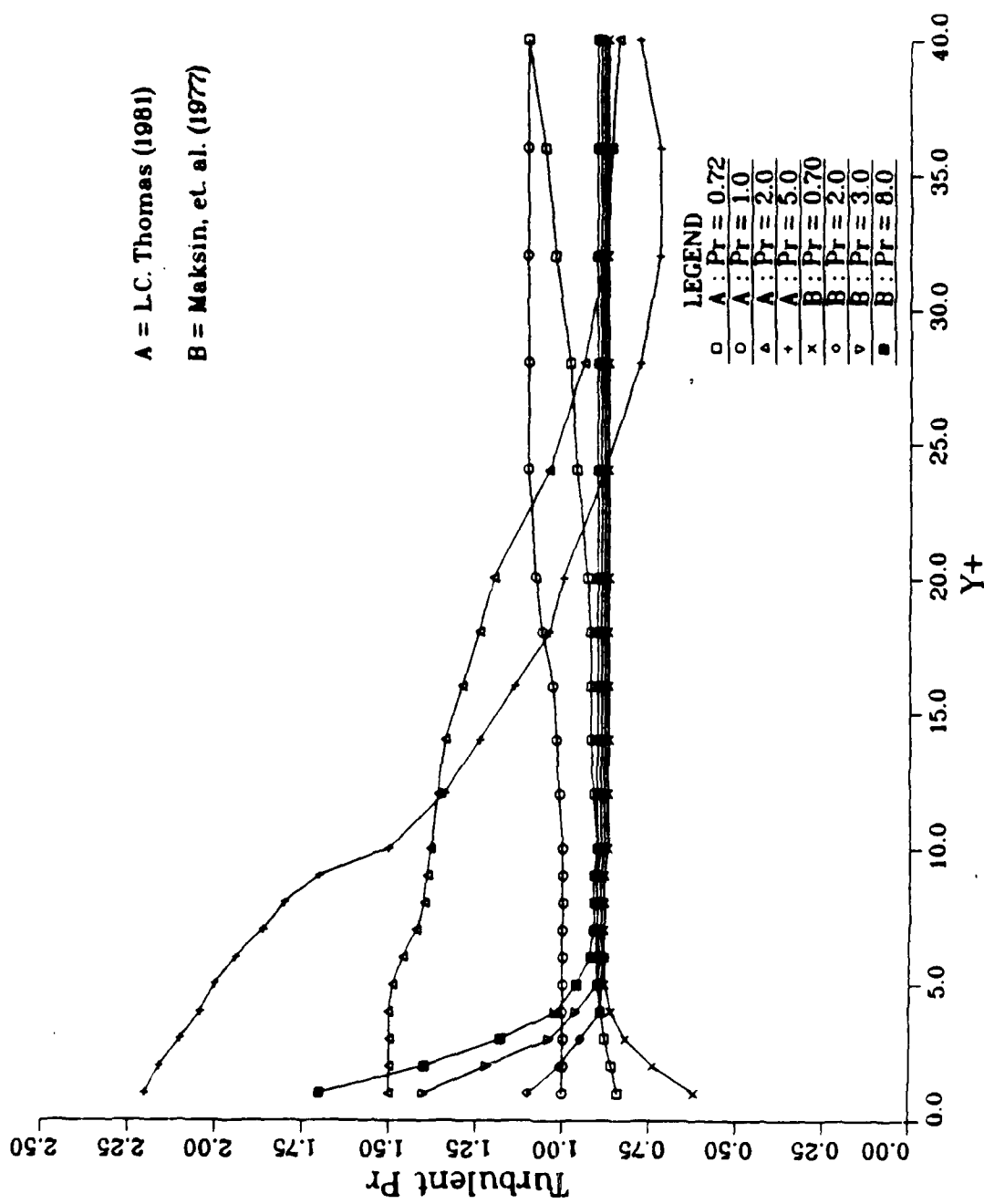
Figure 6 Theoretical uncertainty envelope for the turbulent Prandtl number for various molecular Prandtl number and zero pressure gradient. Two models for Pr_T shown.

71
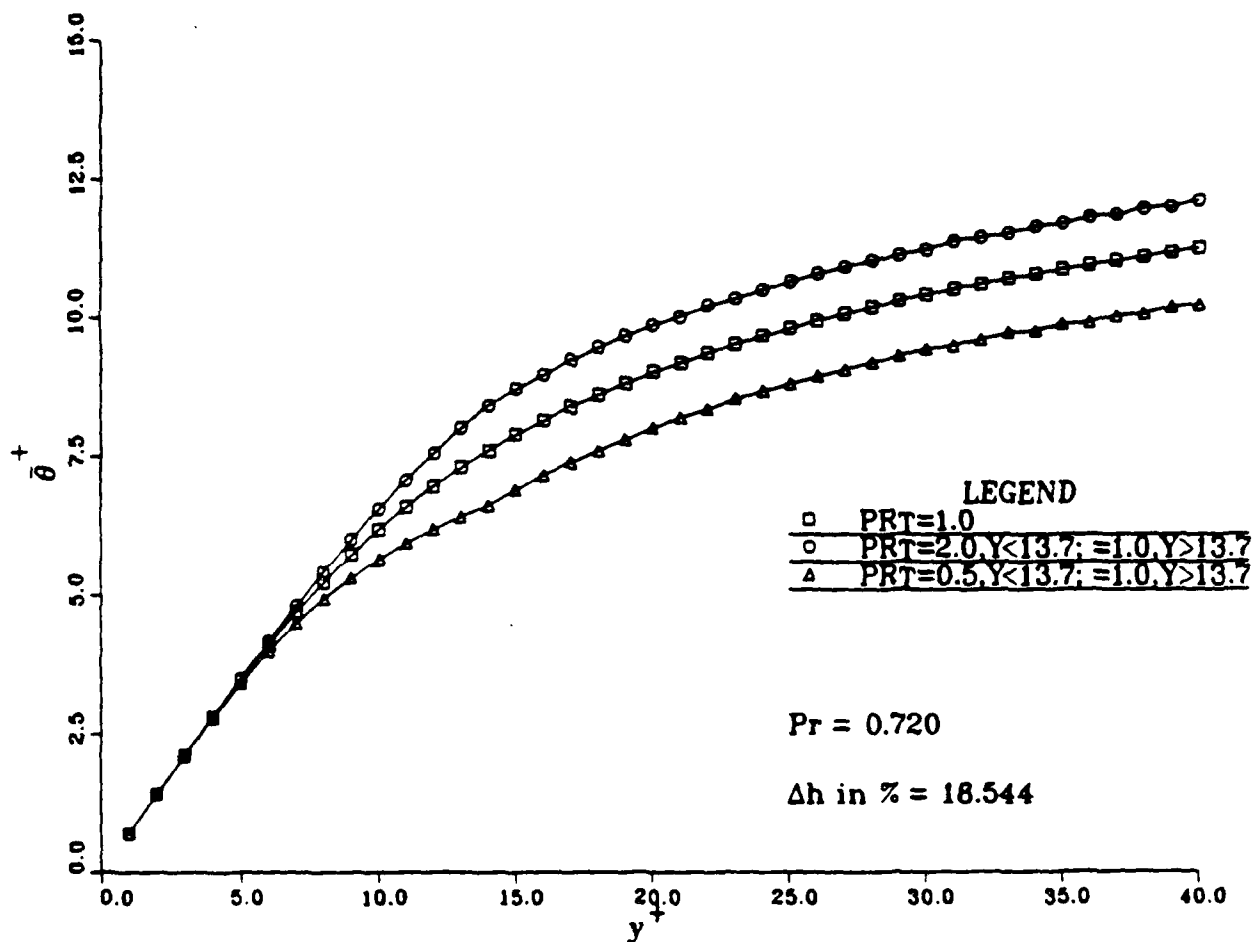
Figure 7 Temperature profiles for a two-layer step model of the turbulent Prandtl number and zero pressure gradient. This shows the effect of the value of Pr_T near the wall. For $Pr = 0.72$, value of Pr_T is switched at $y^+ = 13.7$. Δh is an approximate change in the convective heat transfer coefficient in per cent.

72
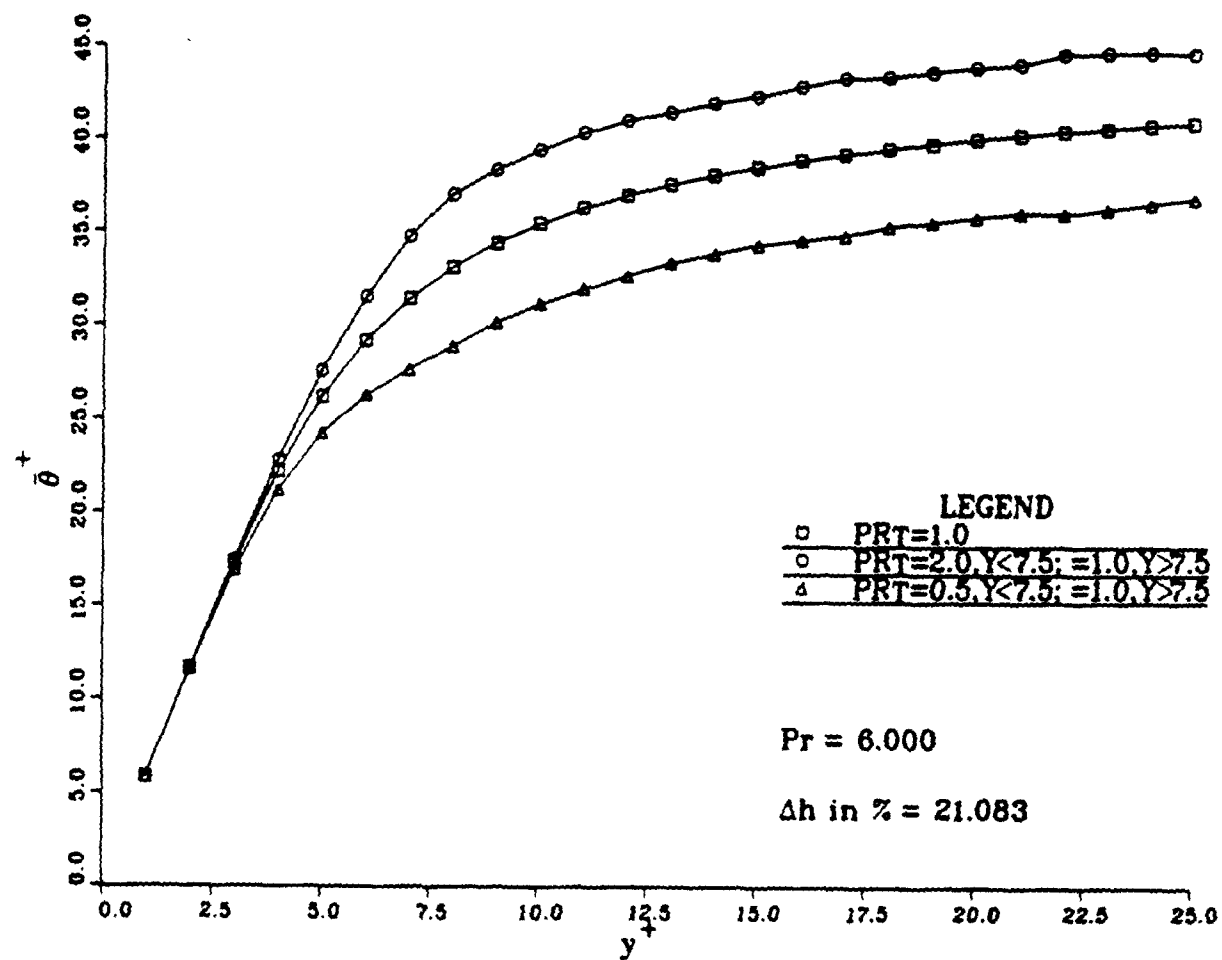
Figure 8 Temperature profiles for a two-layer step model of the turbulent Prandtl number and zero pressure gradient. This shows the effect of the value of Pr_T near the wall. For $Pr = 6.0$, value of Pr_T is switched at $y^+ = 7.5$. Δh is an approximate change in the convective heat transfer coefficient in per cent.

73

Vortices associated with the bursting phenomenon
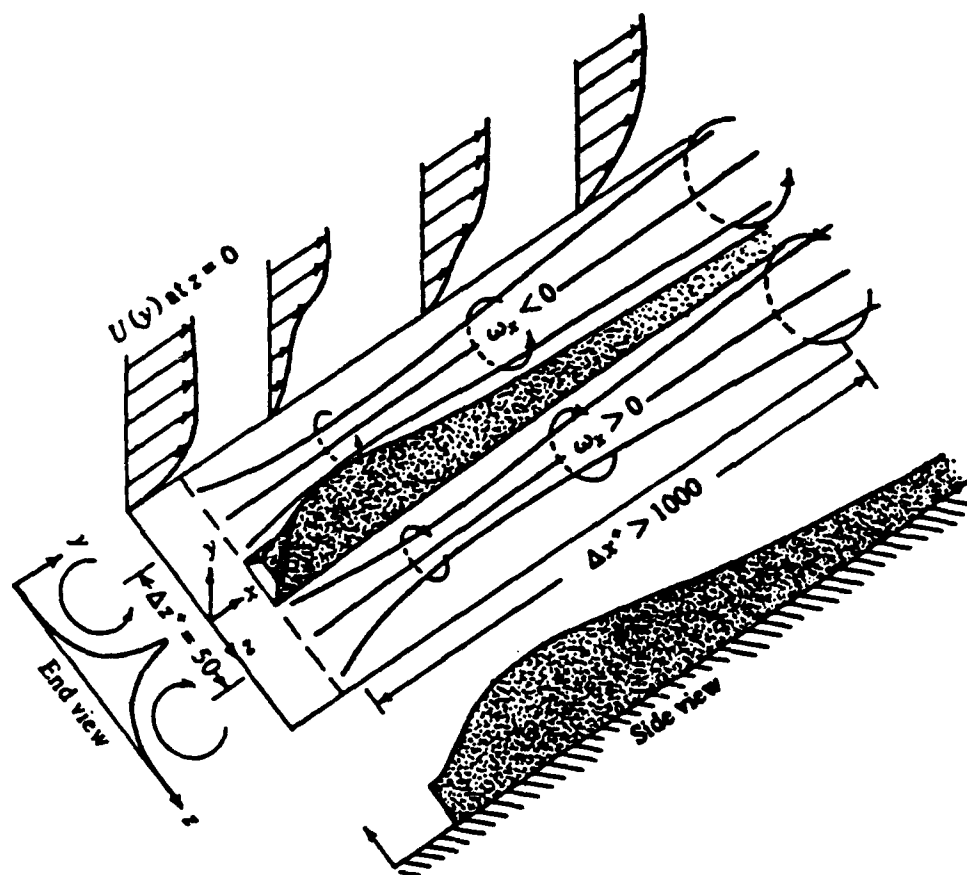
Figure 9 Model of the counter-rotating streamwise vortices with corresponding low-speed streak. From Blackwelder and Eckelmann (1979).

74
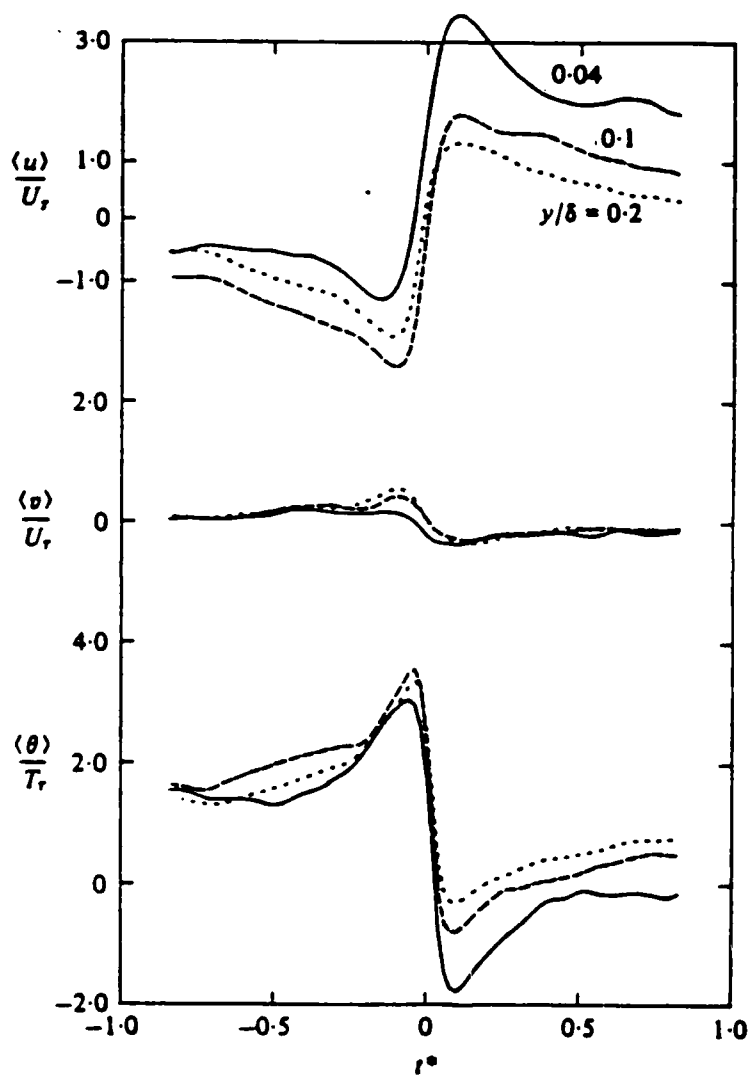
Conditional averages of u, v, θ in the inner layer at $R_m = 990$. ——, $y/\delta = 0.04$, $y^+ = 15$; — —, 0·1, 37; - - -, 0·2, 75.

Figure 10 Phase relationships of conditional averaged signals of $u.v$, and θ during ejecton/sweep event. From Antonia et.al. (1980).

75
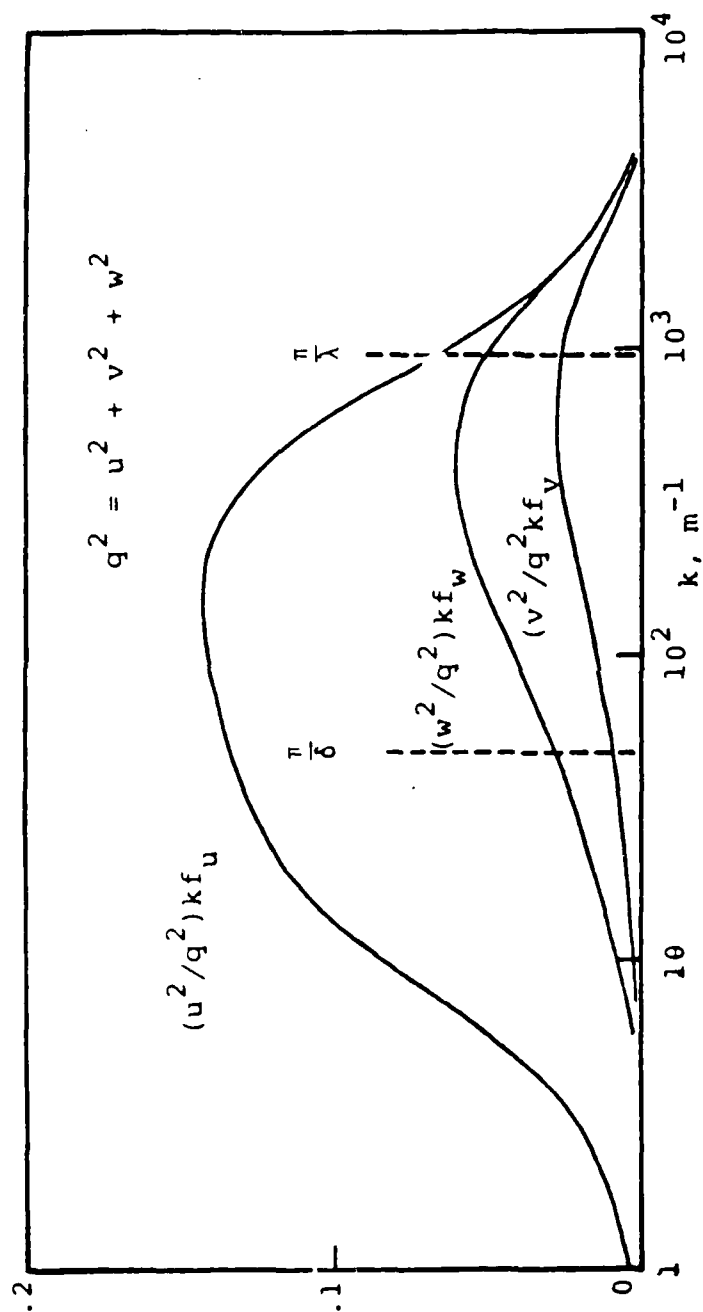
Figure 11 Spectral Density of the three components of velocity and temperature fluctuation at $y^+ = 40$ from data of Fulachier (1972).

76
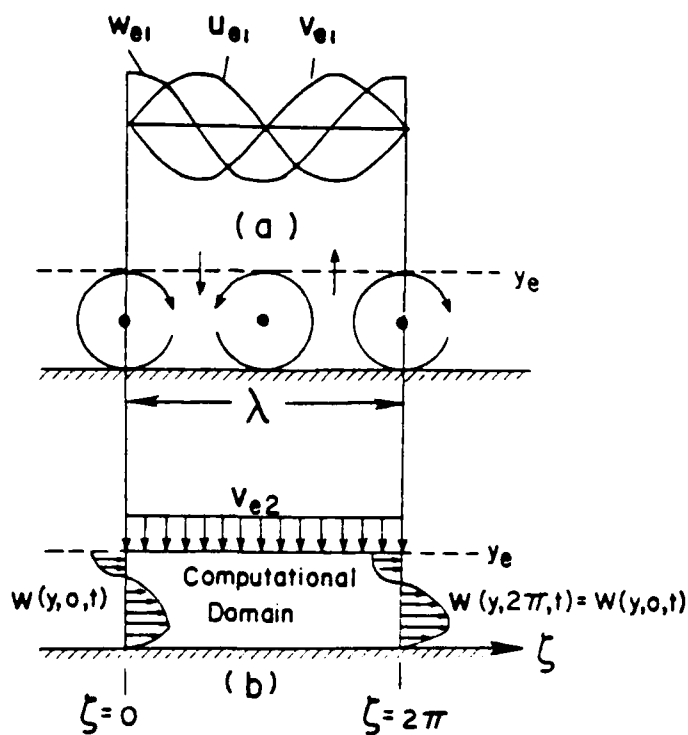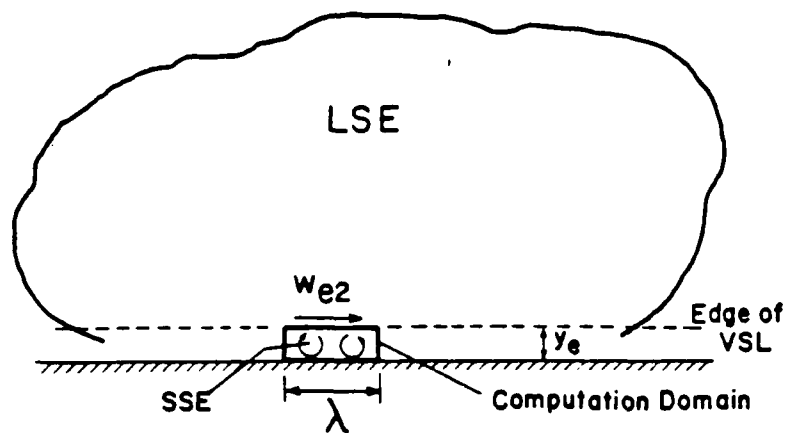
Figure 12 Spanwise view of computational domain for VSL model with contra-rotating vortices.

77
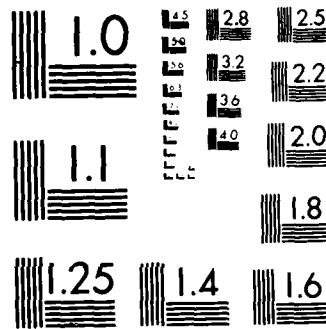
MICROCOPY RESOLUTION TEST CHART
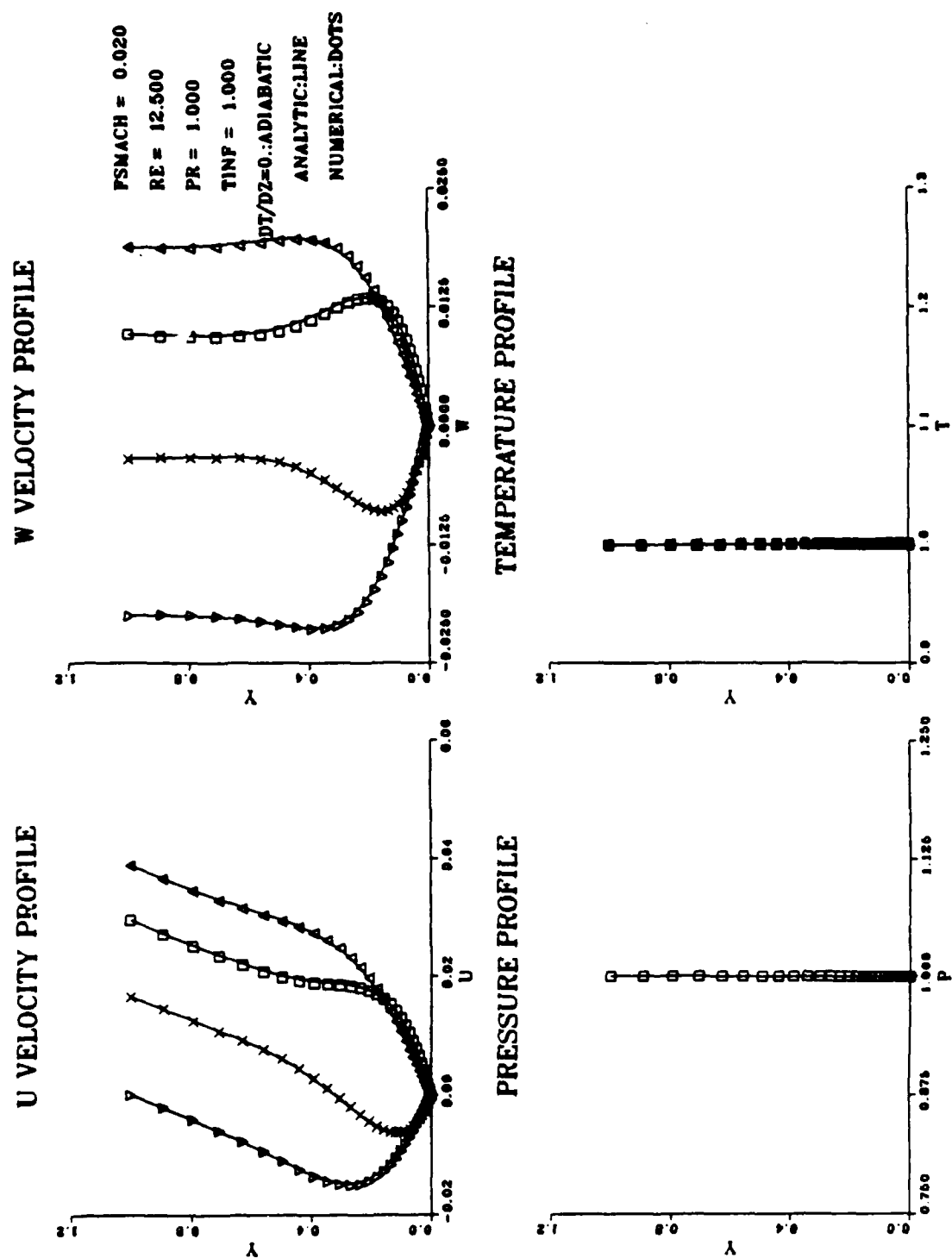
Figure 13 Code verification test with oscillating shear flow and an adiabatic wall temperature boundary condition. Computed values plotted as symbols. (Different symbols for different times.) Analytic solution shown as solid line.

78
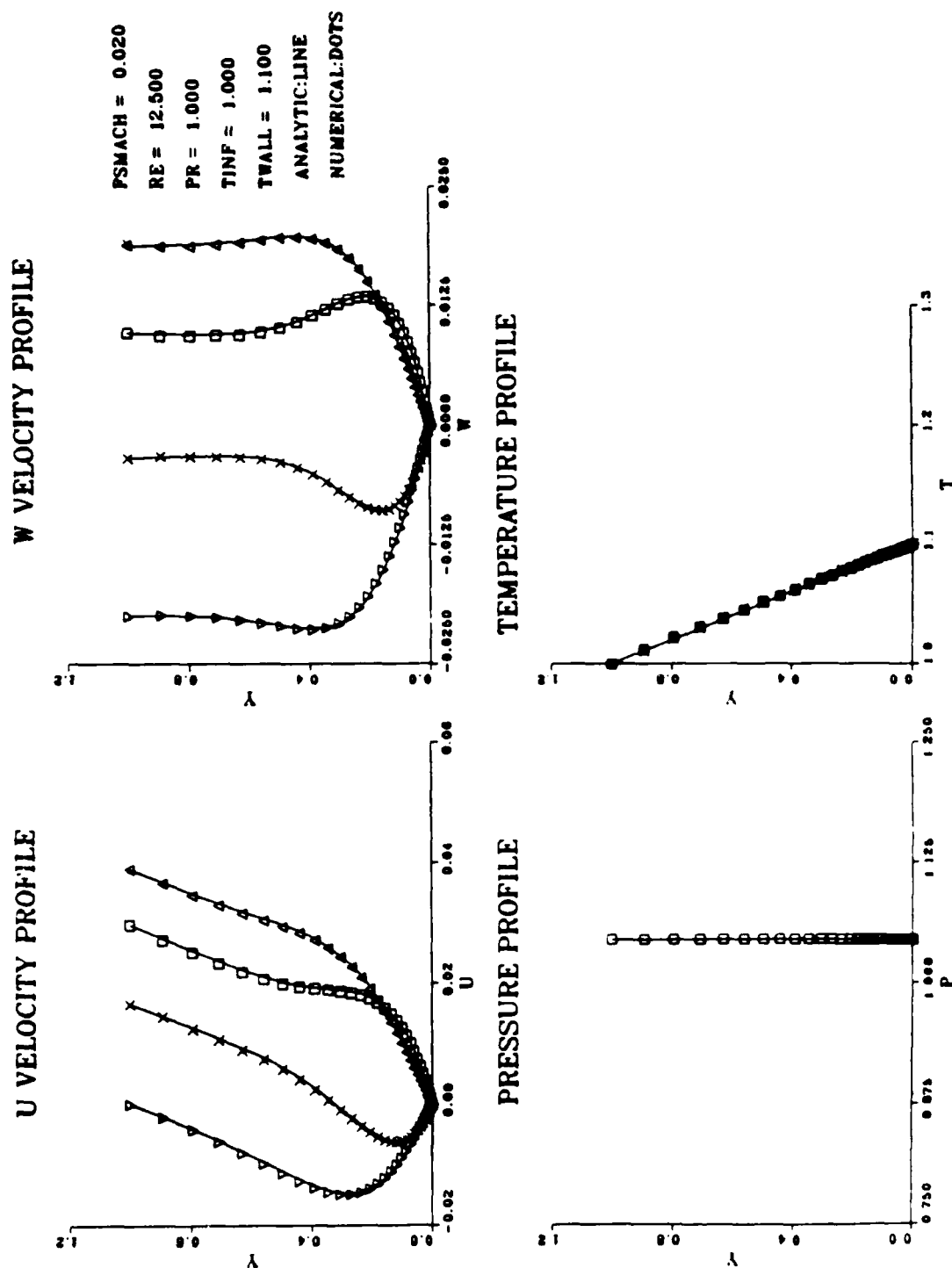
Figure 14 Code verification test with oscillating shear flow and an isothermal wall temperature boundary condition. Computed values plotted as symbols. (Different symbols for different times.) Analytic solution shown as solid line.

79
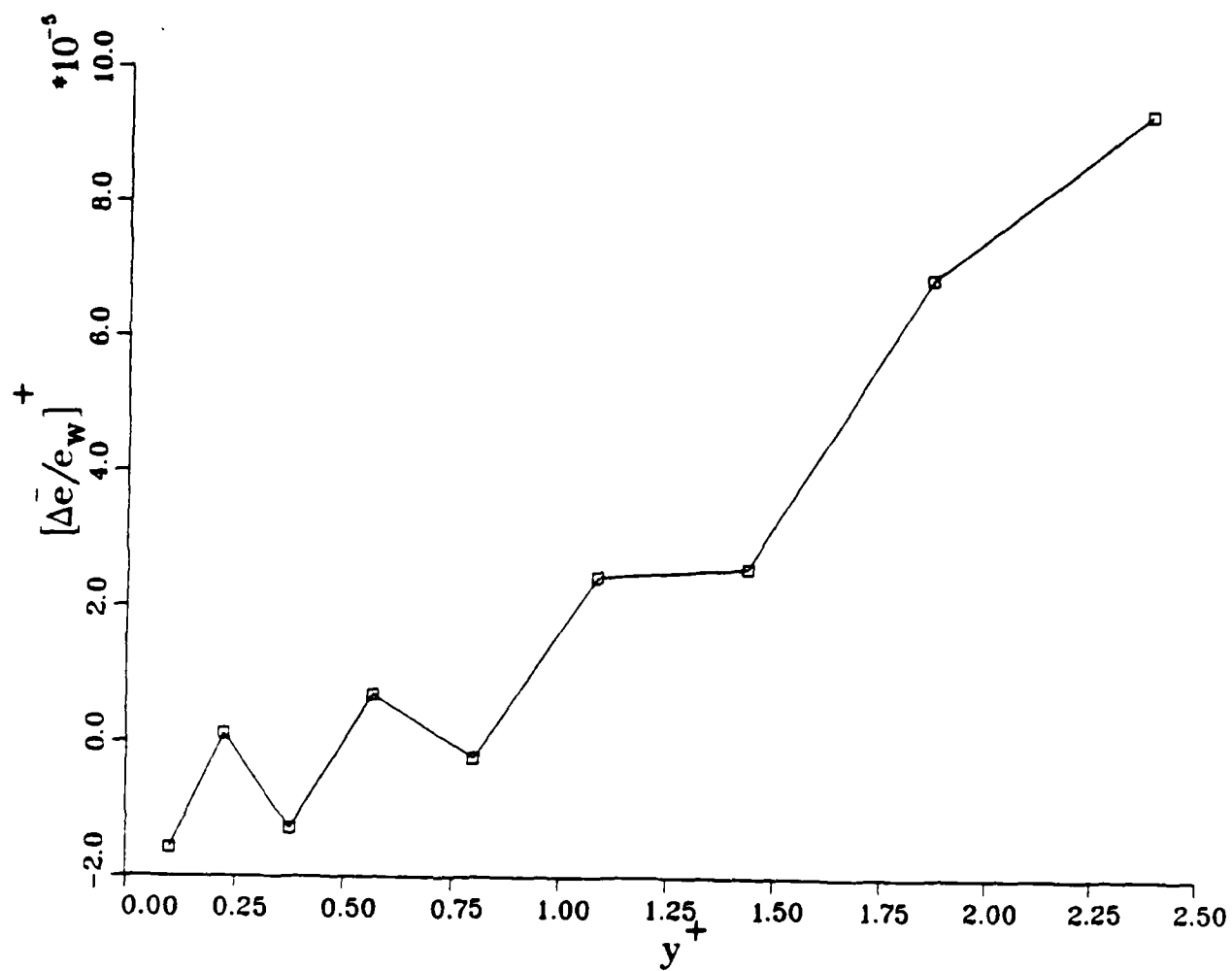
Figure 15 Near wall decoupling of $\dfrac{\Delta \bar{e}}{\bar{e}_w}$ with $\Delta \bar{e} = e - \bar{e}_w$.

80
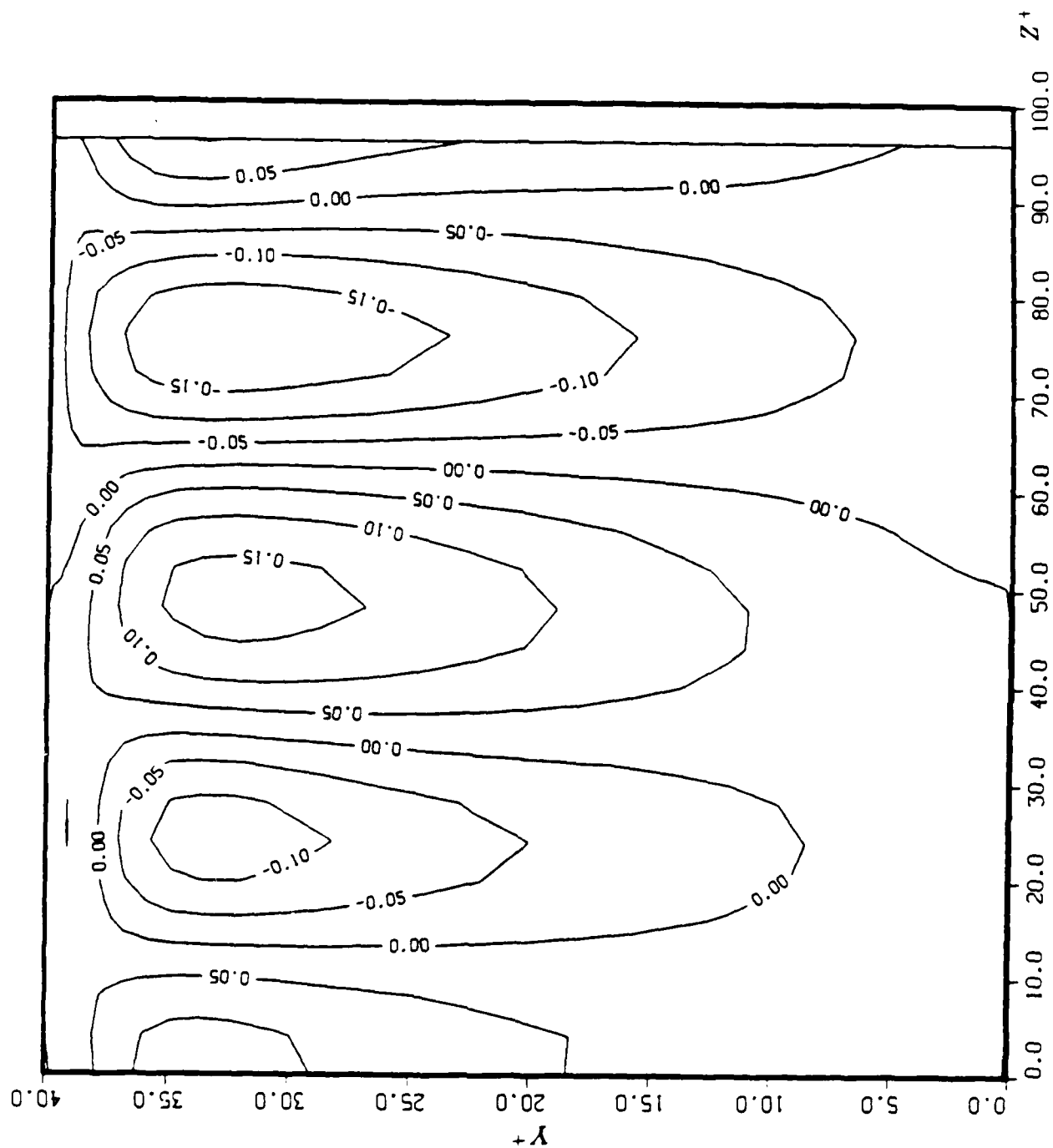
Figure 16(a) Contour plot of the vertical velocity component v before any averaging is applied $N_1 T = 0$.

81
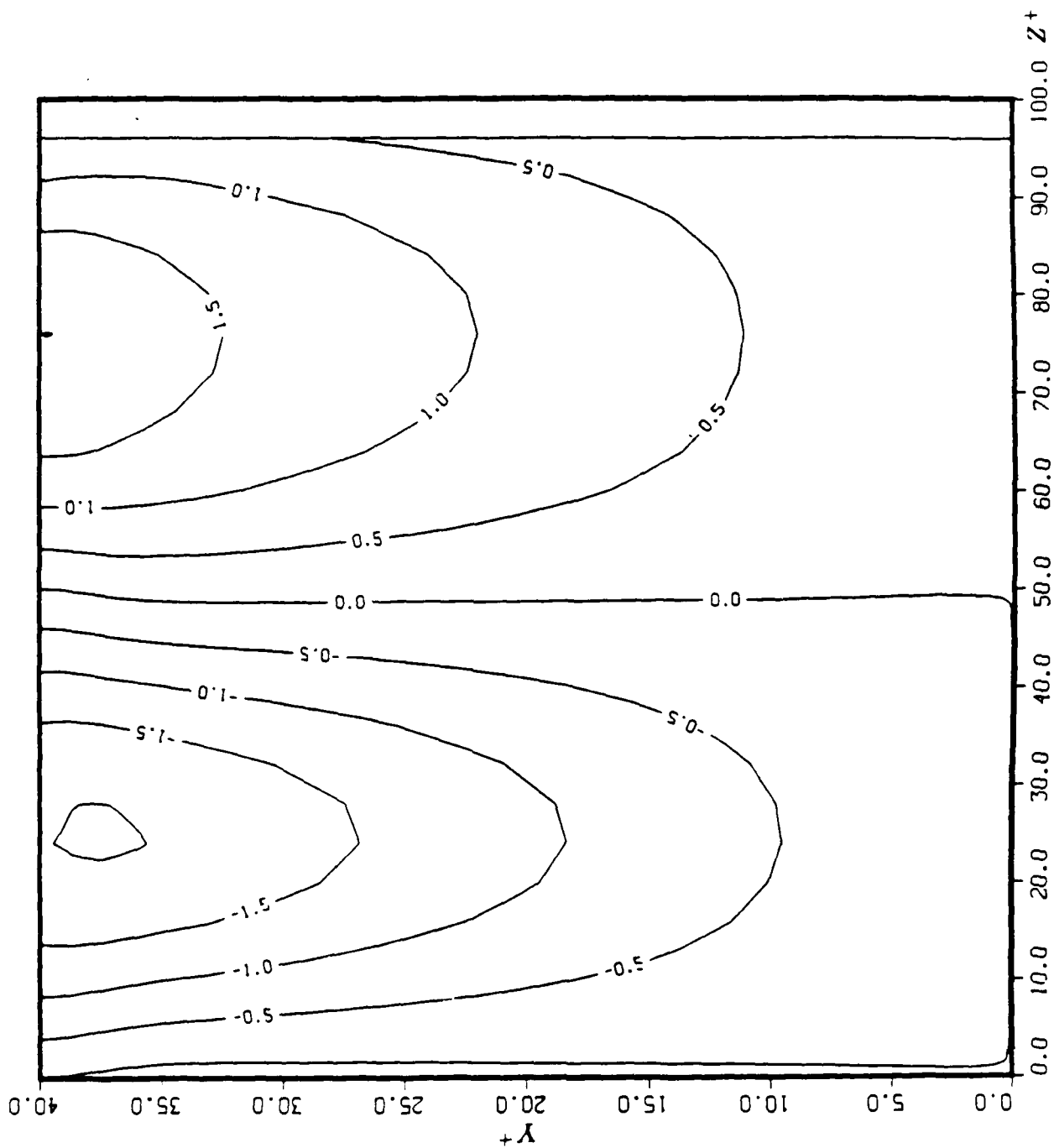
Figure 16(b) Contour plot of the vertical velocity component v before any averaging is applied $N_1T = \dfrac{\pi}{4}$.

82
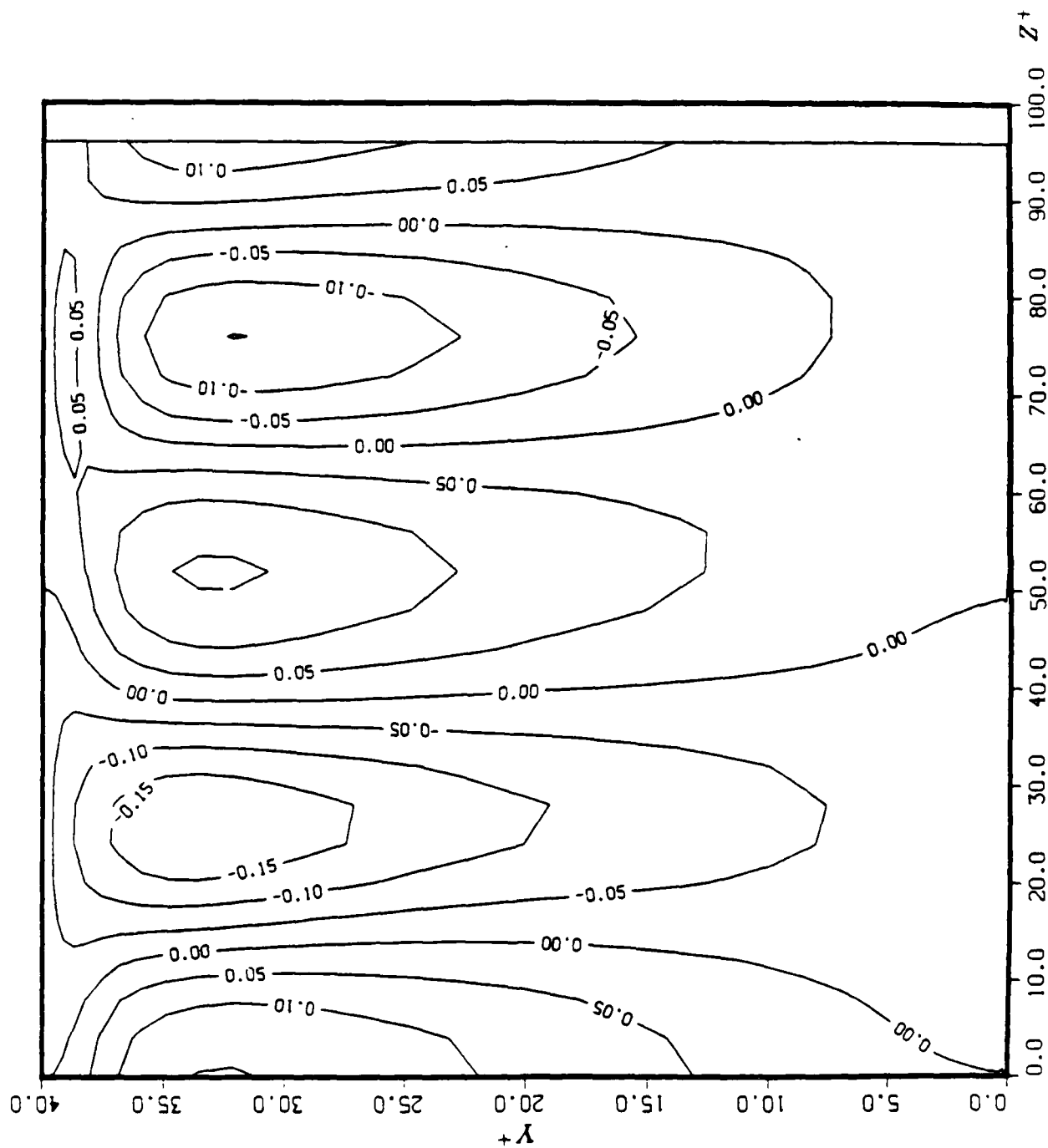
Figure 16(c) Contour plot of the vertical velocity component v before any averaging is applied
$N_1 T = \dfrac{\pi}{2}$.

83
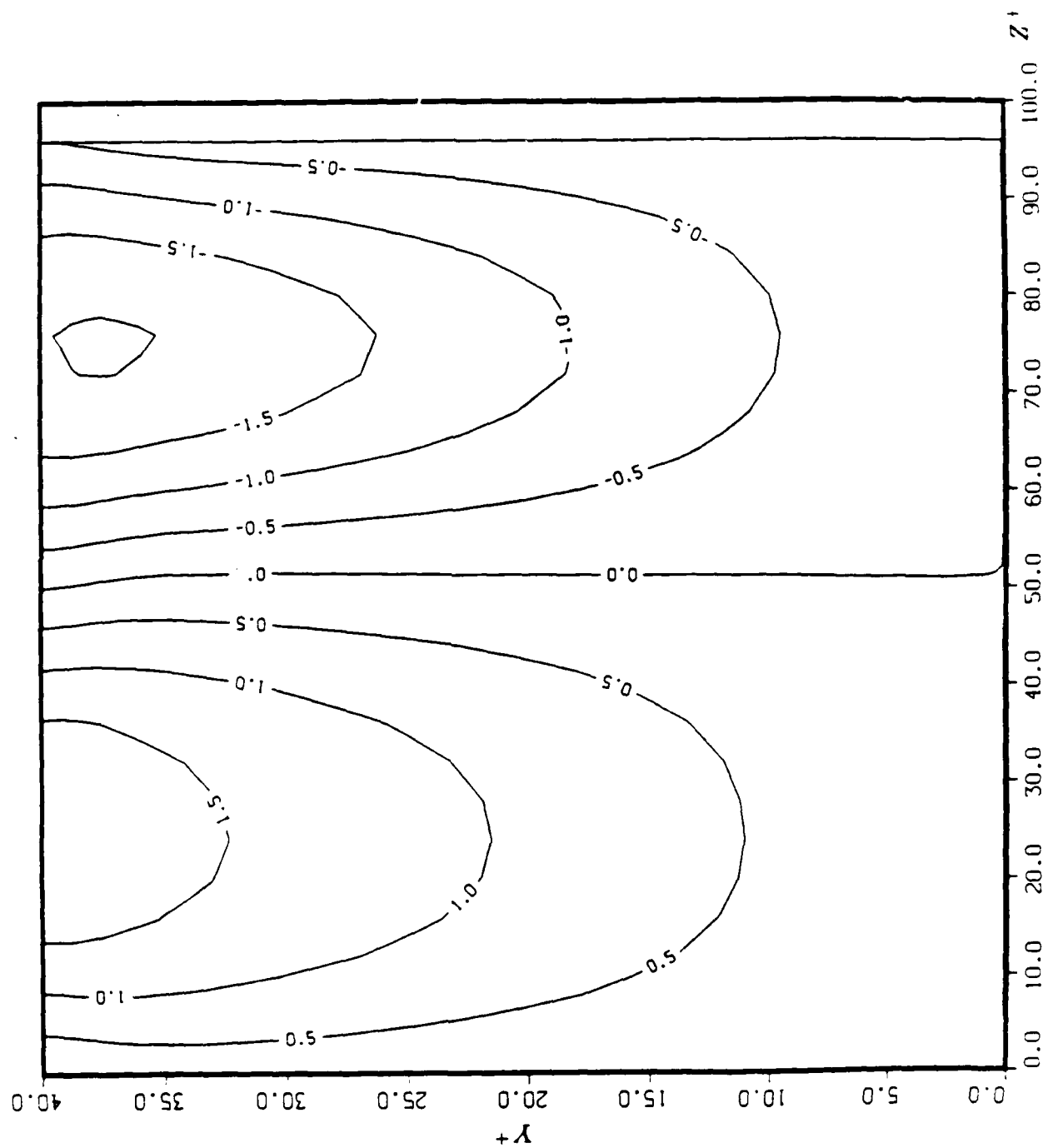
Figure 16(d) Contour plot of the vertical velocity component v before any averaging is applied $N_1 T = \frac{3\pi}{4}$.

84
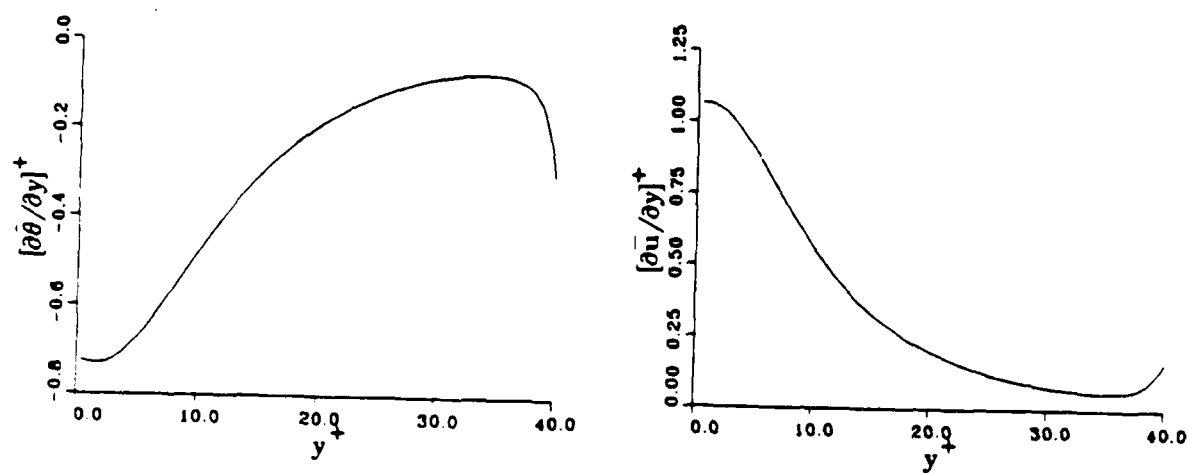
Figure 17 Computed mean temperature and streamwise velocity gradient showing anomoly near outer boundary.

85
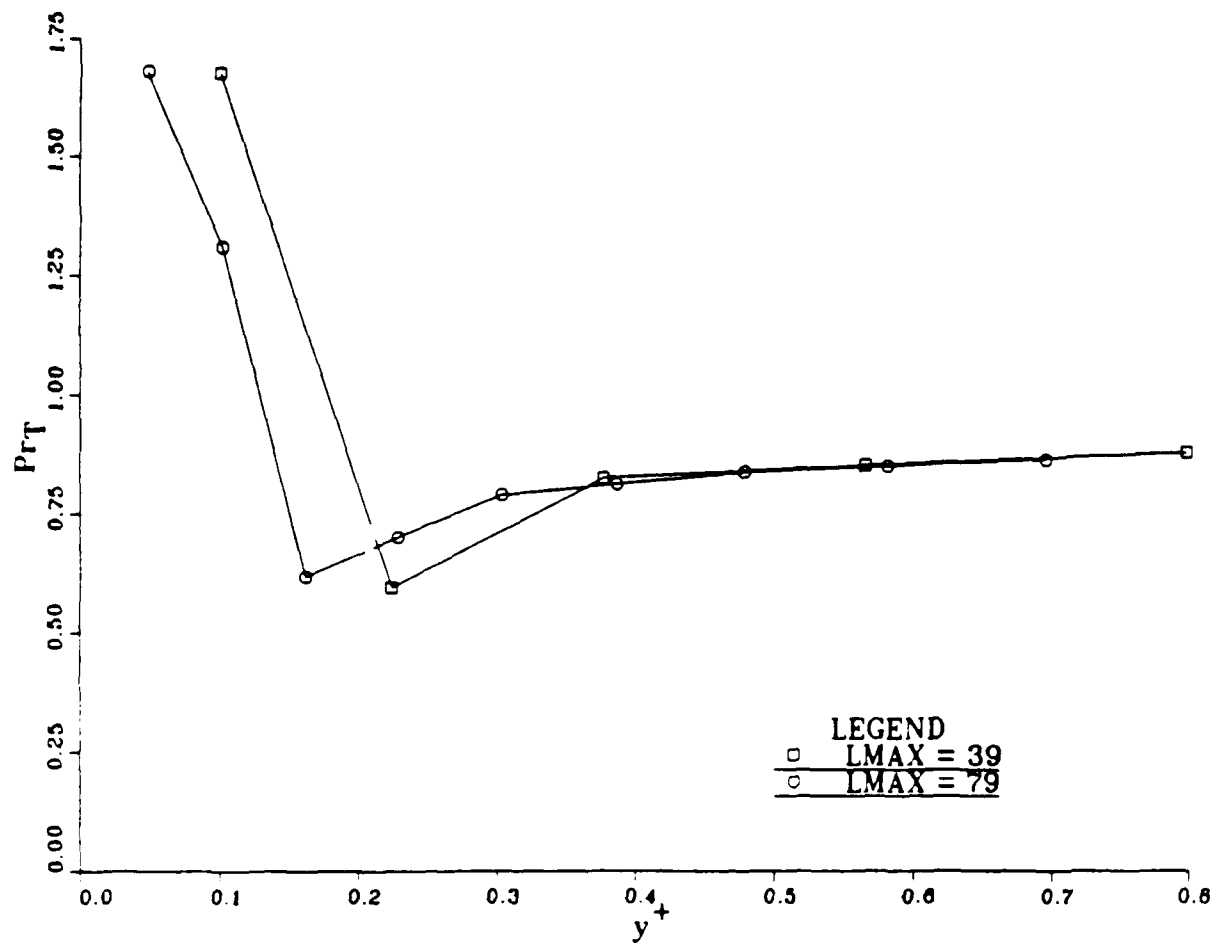
Figure 18 Grid dependency illustrated near wall with Pr_T as grid is refined.

86
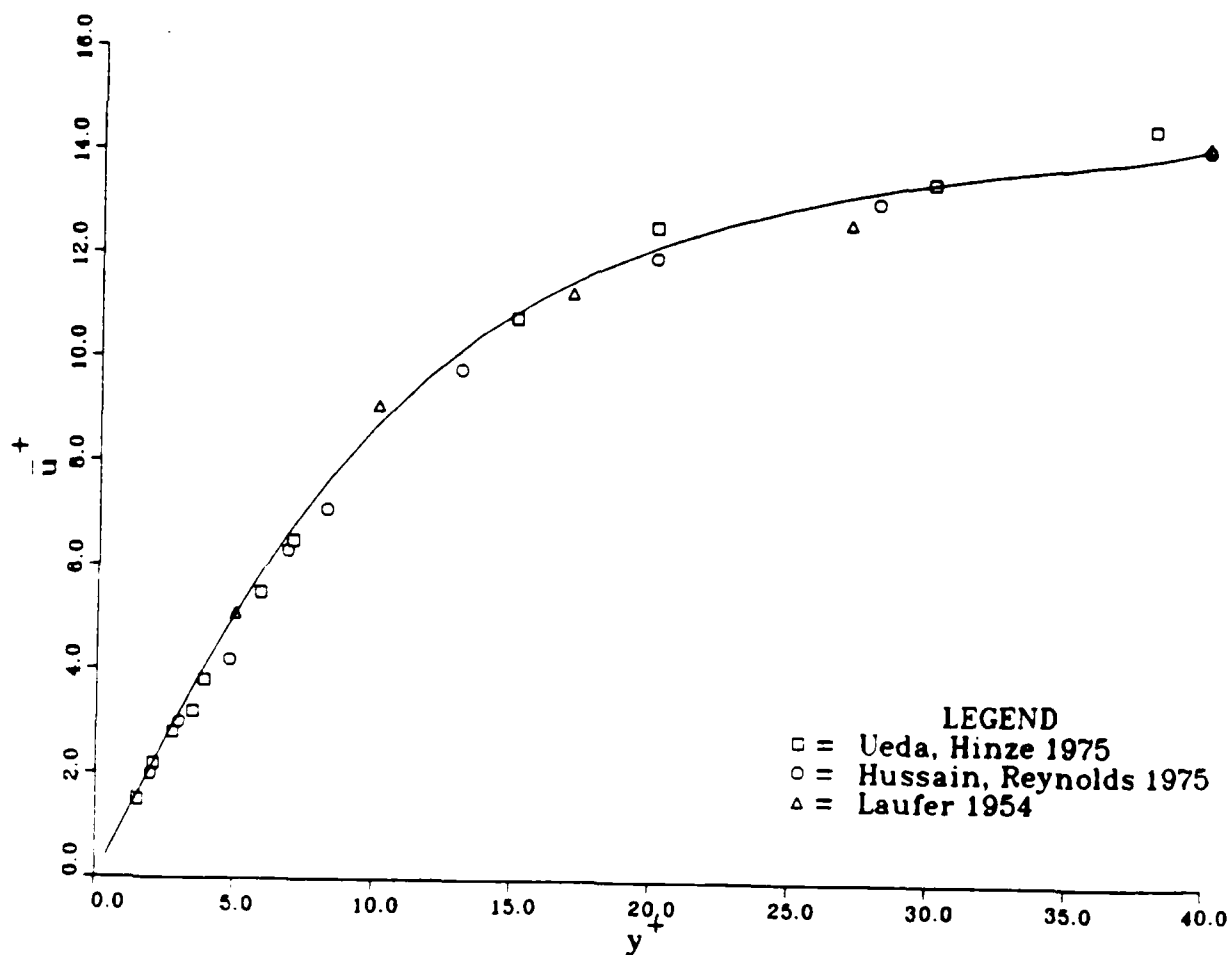
Figure 19 Computed mean streamwise velocity $\bar{u}^+$ for $Pr = 0.72$, isothermal wall temperature boundary condition, zero mean streamwise pressure gradient. Symbols represent experimental data.

87
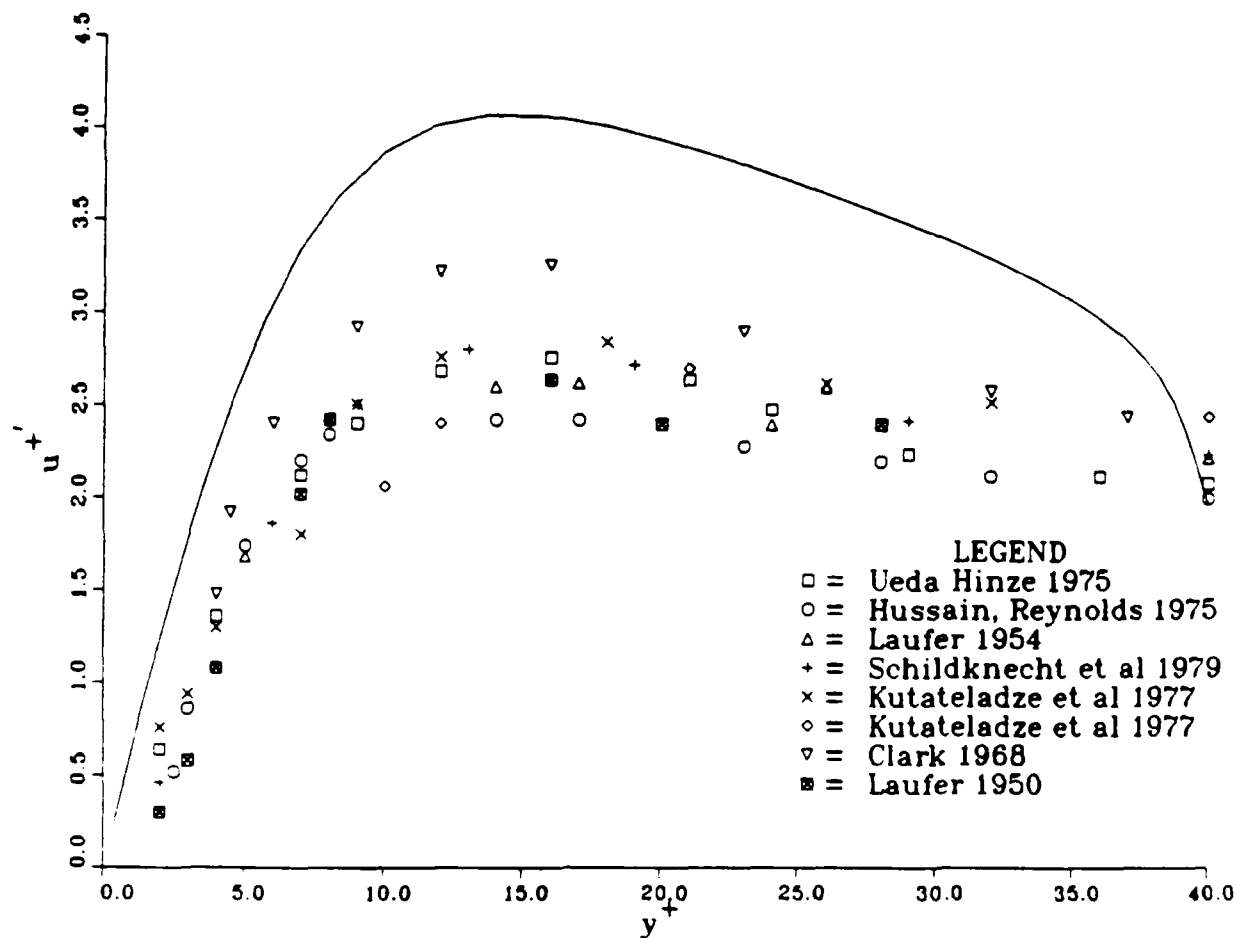
Figure 20 Computed streamwise velocity intensity $u^{+'}$ for $Pr = 0.72$,isothermal wall temperature boundary condition,zero mean streamwise pressure gradient. Symbols represent experimental data.
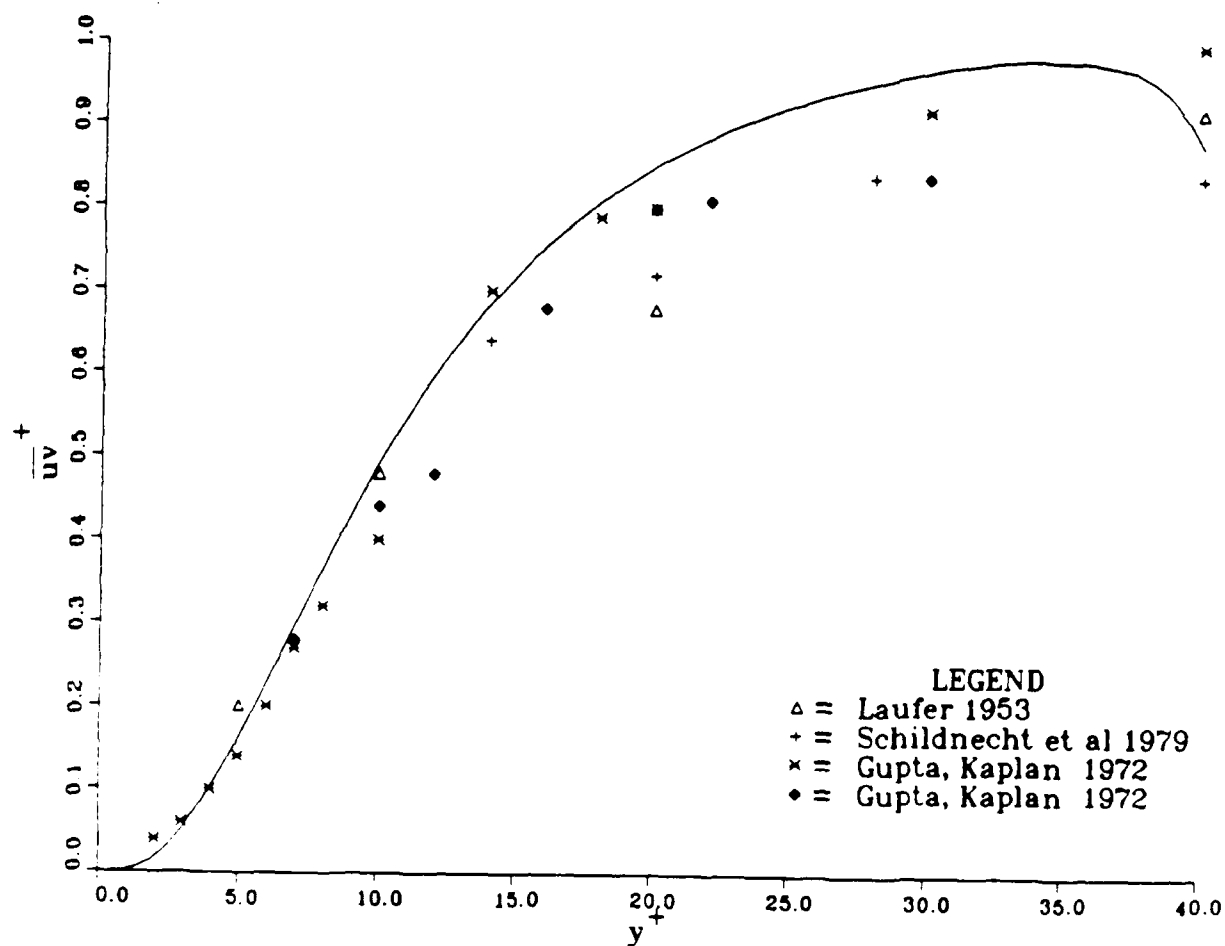
Figure 21 Computed Reynolds stress $\overline{uv}^+$ for $Pr = 0.72$,isothermal wall temperature boundary condition.zero mean streamwise pressure gradient. Symbols represent experimental data.
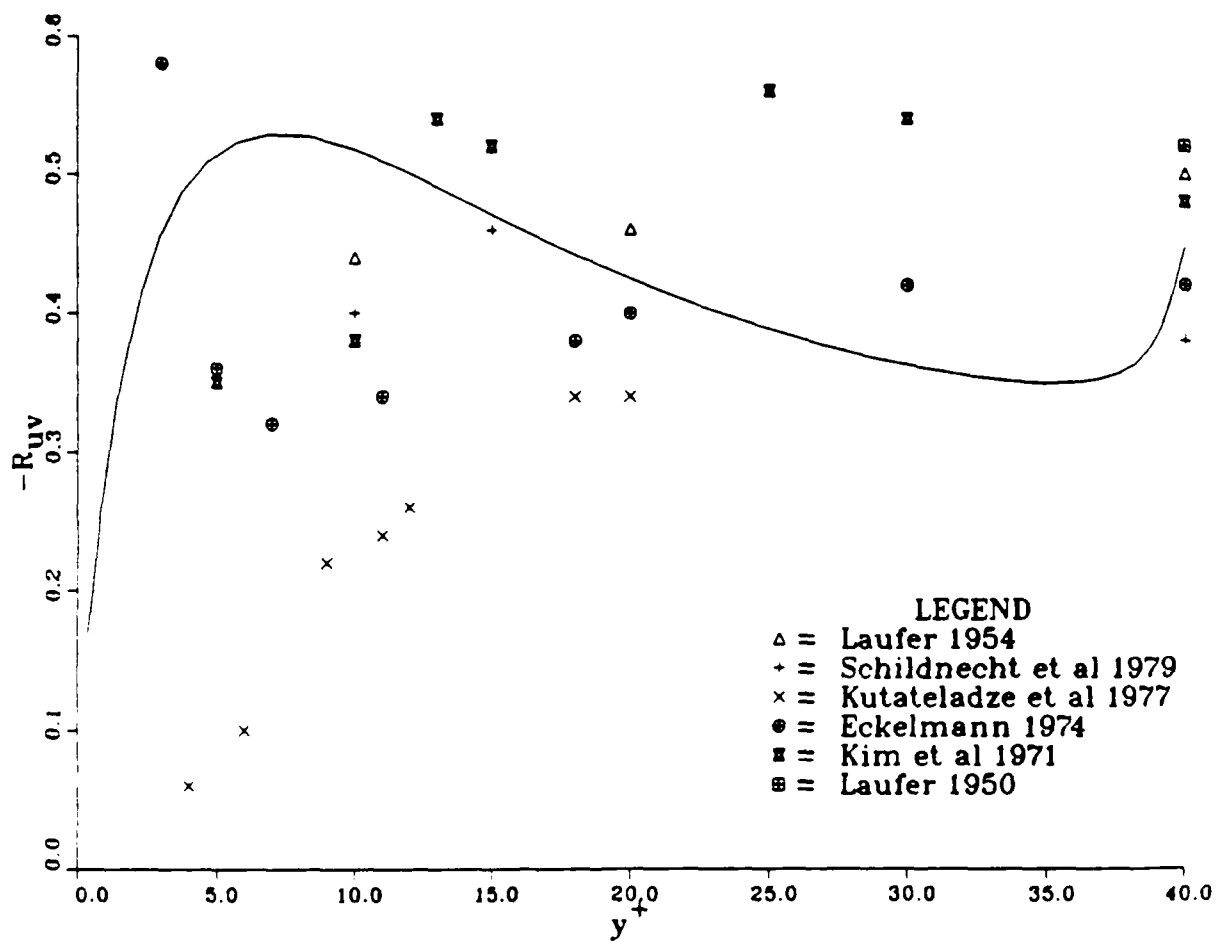
Figure 22 Computed correlation coefficient R_{uv} for $Pr = 0.72$, isothermal wall temperature boundary condition, zero mean streamwise pressure gradient. Symbols represent experimental data.

90
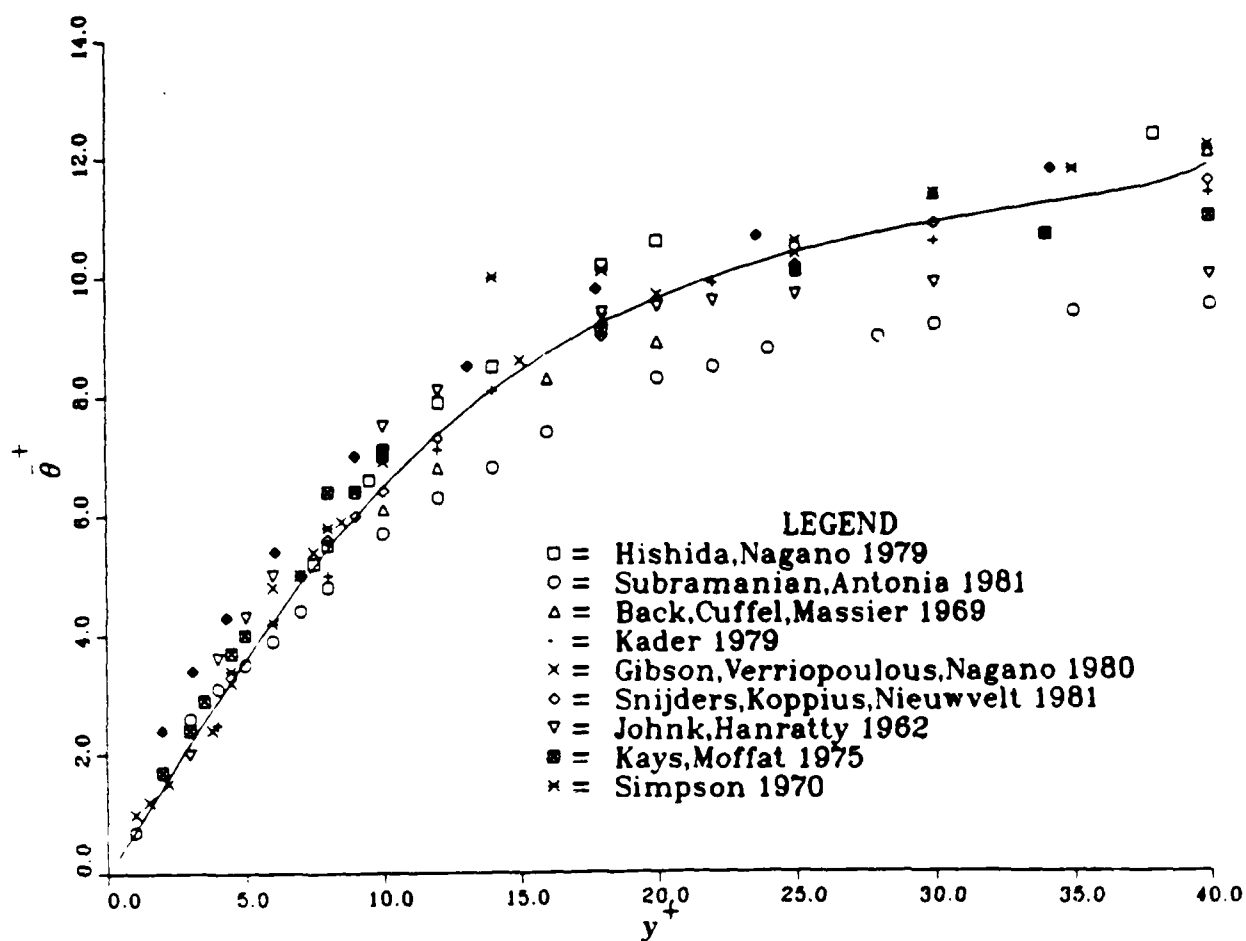
Figure 23 Computed mean temperature $\tilde{\theta}^+$ for $Pr = 0.72$,isothermal wall temperature boundary condition,zero mean streamwise pressure gradient. Symbols represent experimental data.
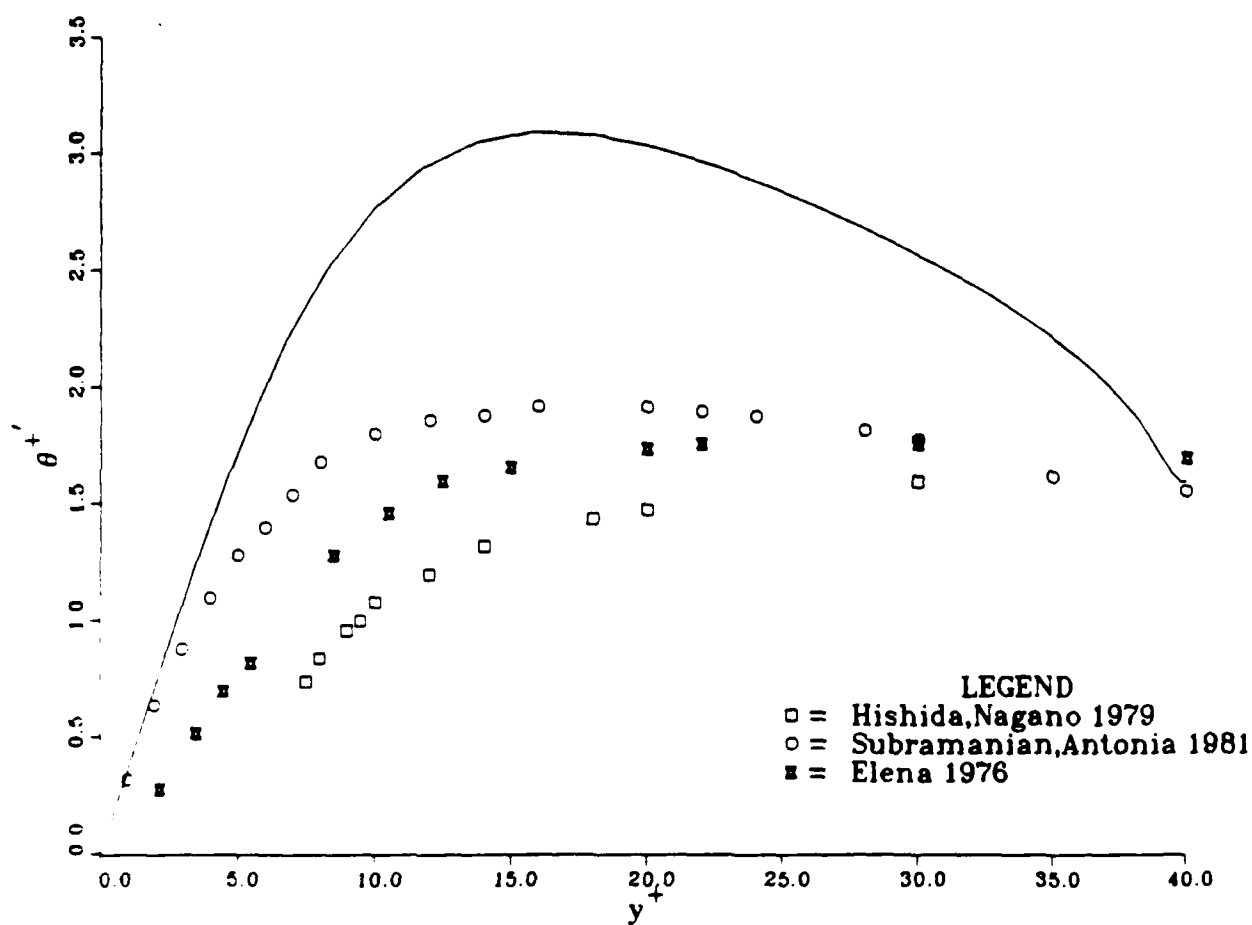
Figure 24 Computed temperature intensity $\theta^{+\prime}$ for $Pr = 0.72$.isothermal wall temperature boundary condition.zero mean streamwise pressure gradient. Symbols represent experimental data.

92
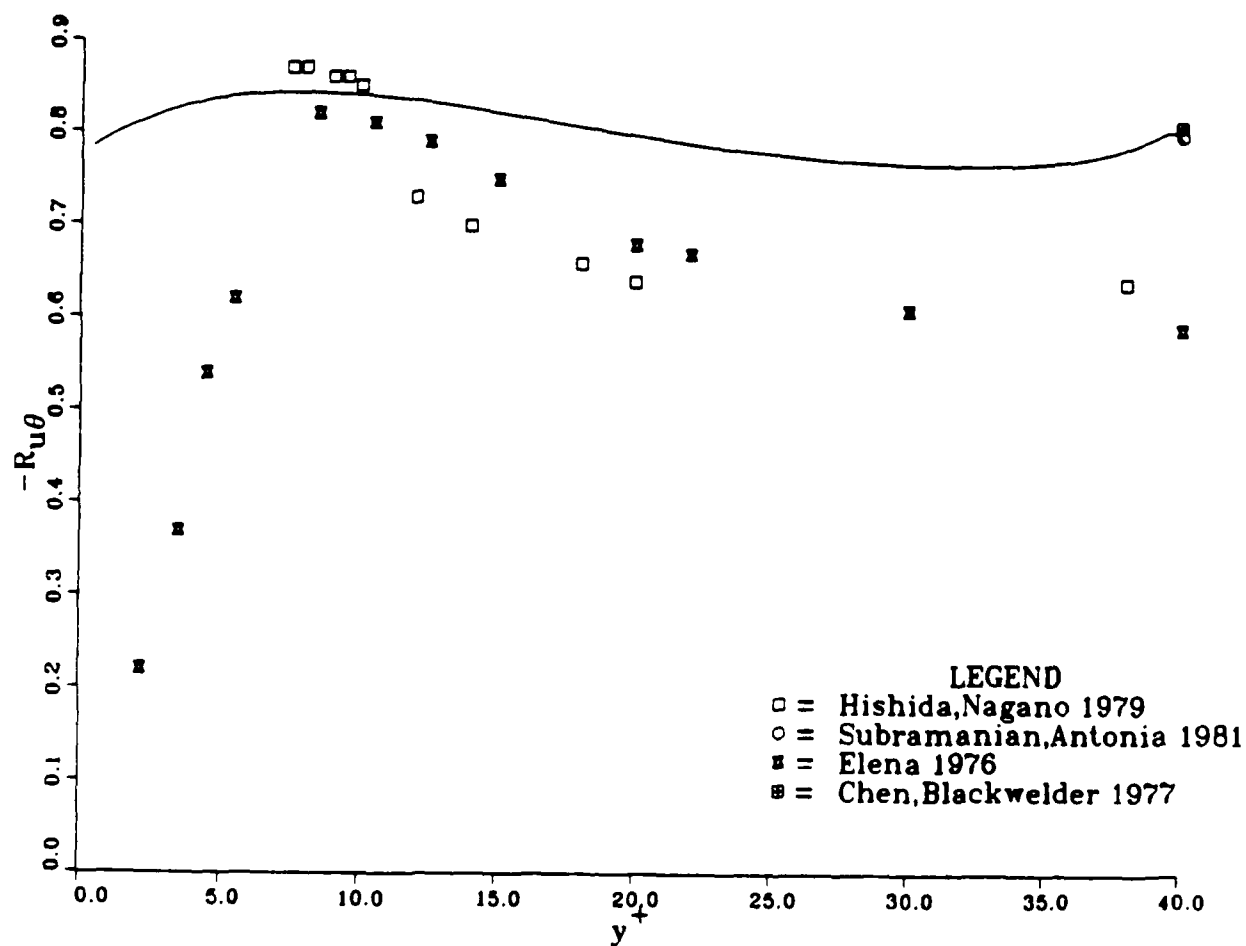
Figure 25 Computed correlation coefficient $R_{u\theta}$ for $Pr = 0.72$,isothermal wall temperature boundary condition,zero mean streamwise pressure gradient. Symbols represent experimental data.

93
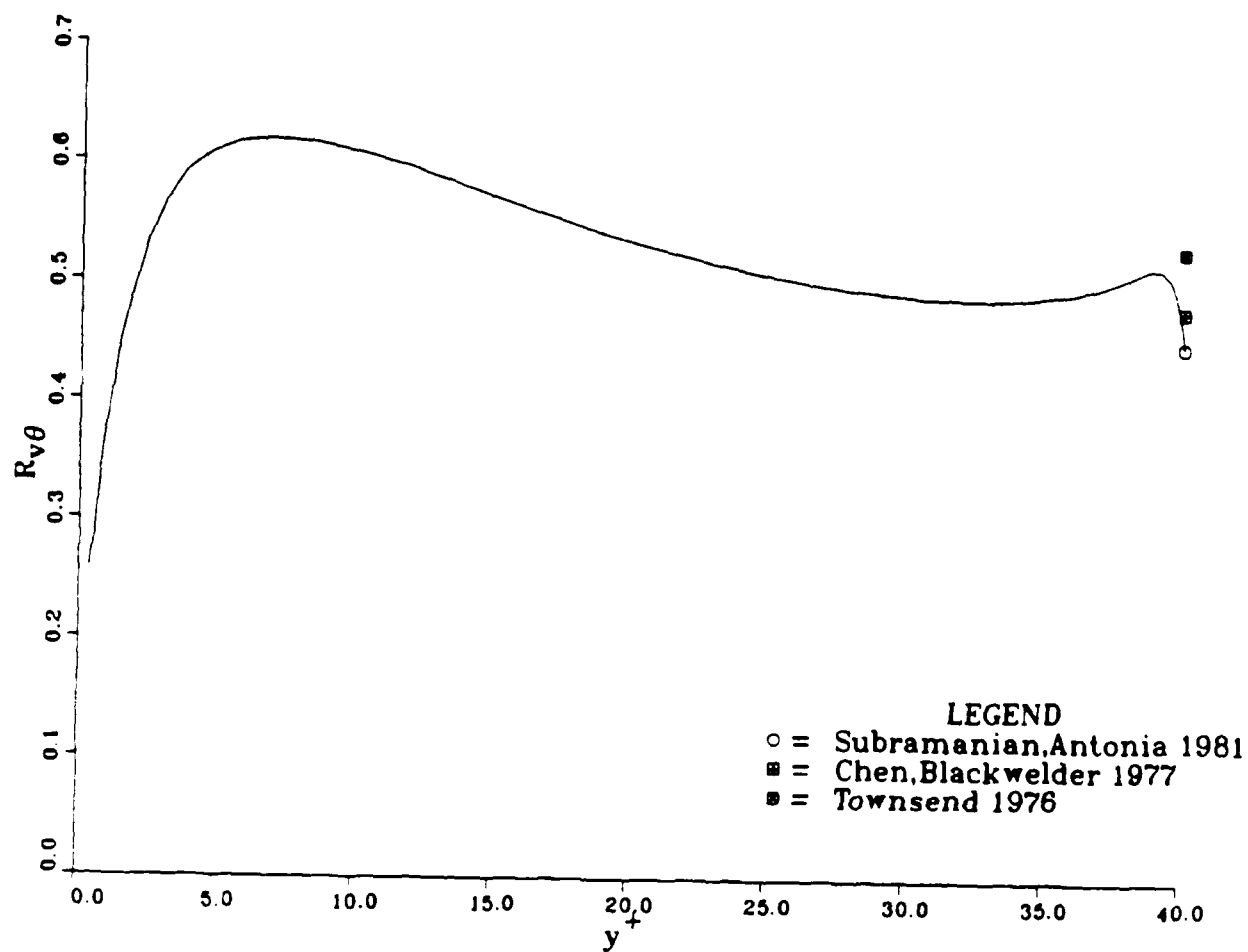
Figure 26 Computed correlation coefficient $R_{v\theta}$ for $Pr = 0.72$,isothermal wall temperature boundary condition,zero mean streamwise pressure gradient. Symbols represent experimental data.

94
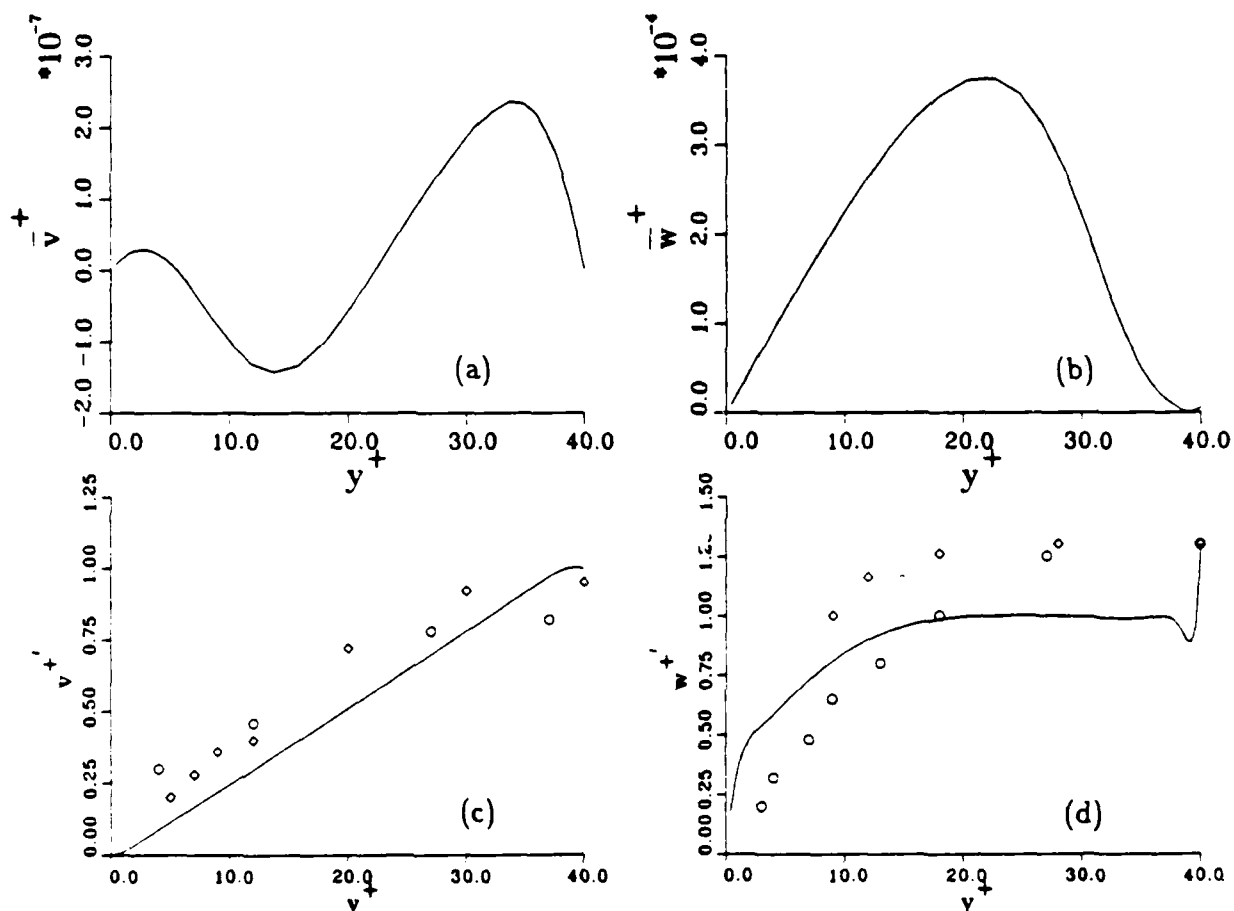
Figure 27 (a) Mean normal velocity $\bar{v}$,(b) Mean spanwise velocity $\bar{w}$,(c) Normal velocity intensity v'. $\diamond$ = Schildnecht (1979), $\circ$ = Laufer (1953), (d) Spanwise velocity intensity w'. Symbols same as (c), for $Pr = 0.72$ and zero pressure gradient.

95
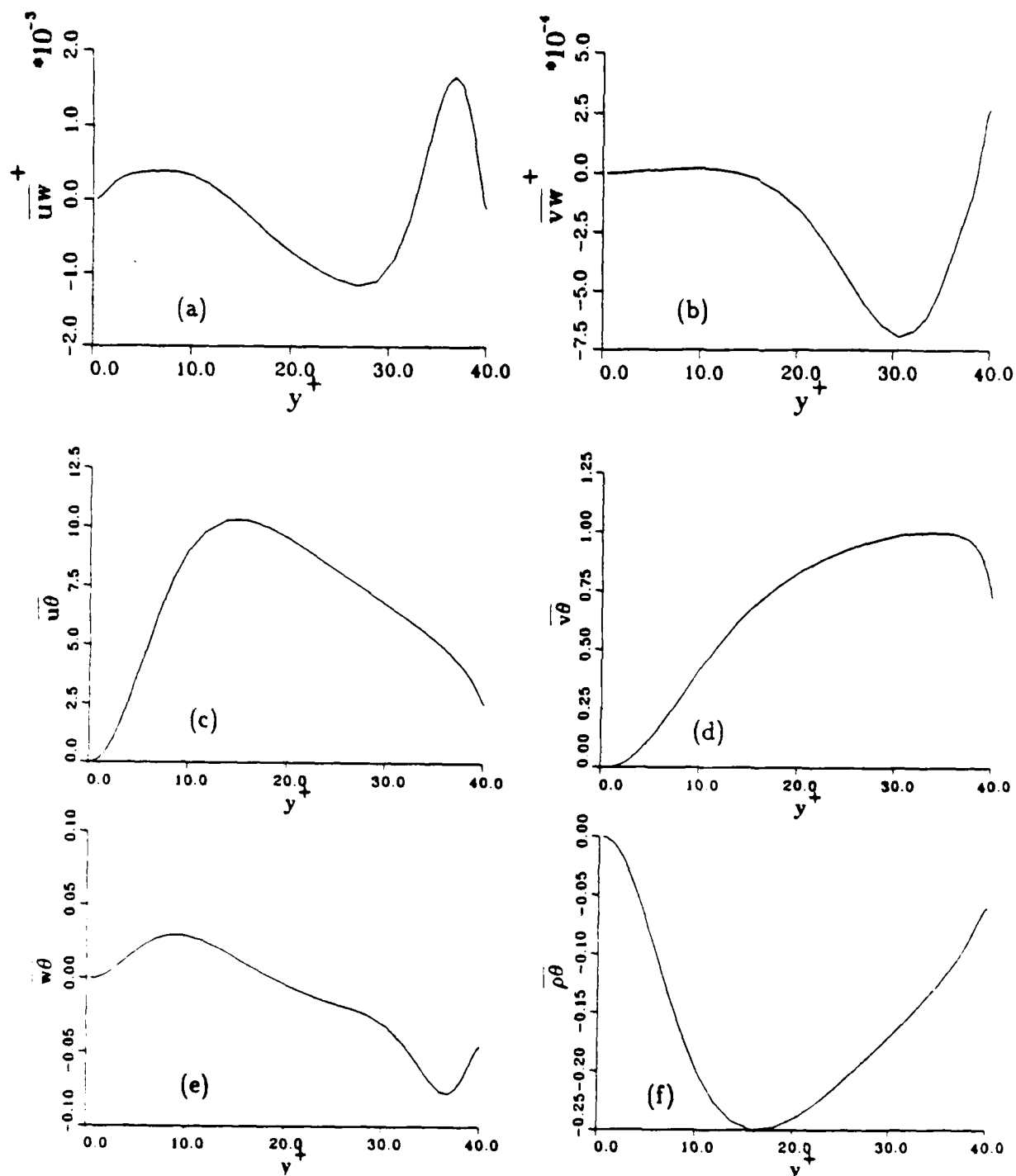
Figure 28 (a) Correlation $\overline{uw}$,(b) Correlation $\overline{vw}$,(c) Correlation $\overline{u\theta}$, (d) Correlation $\overline{v\theta}$, (e) Correlation $\overline{w\theta}$,(f) Correlation $\overline{\rho\theta}$, for $Pr = 0.72$ and zero pressure gradient.

96
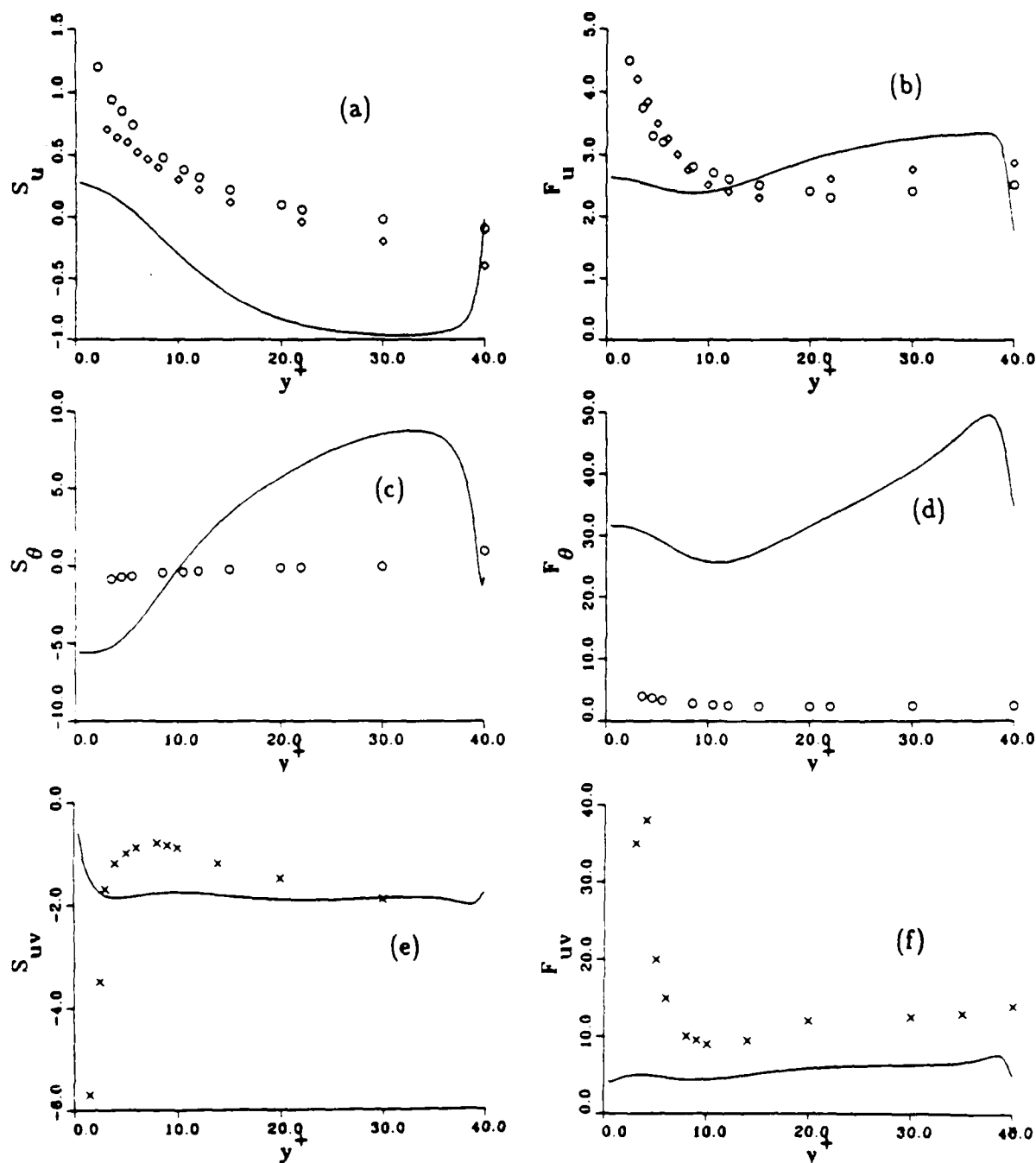
Figure 29 (a) Skewness of u, $\diamond$ = Ueda (1975), $\circ$ = Elena (1979), (b) Flatness of u, Symbols same as (a), (c) Skewness of θ, Symbols same as (a), (d) Flatness of θ, Symbols same as (a),(e) Skewness of uv, $\times$ = Gupta (1972), (f) Flatness of uv, Symbol same as (e), for $Pr = 0.72$ and zero pressure gradient.

97
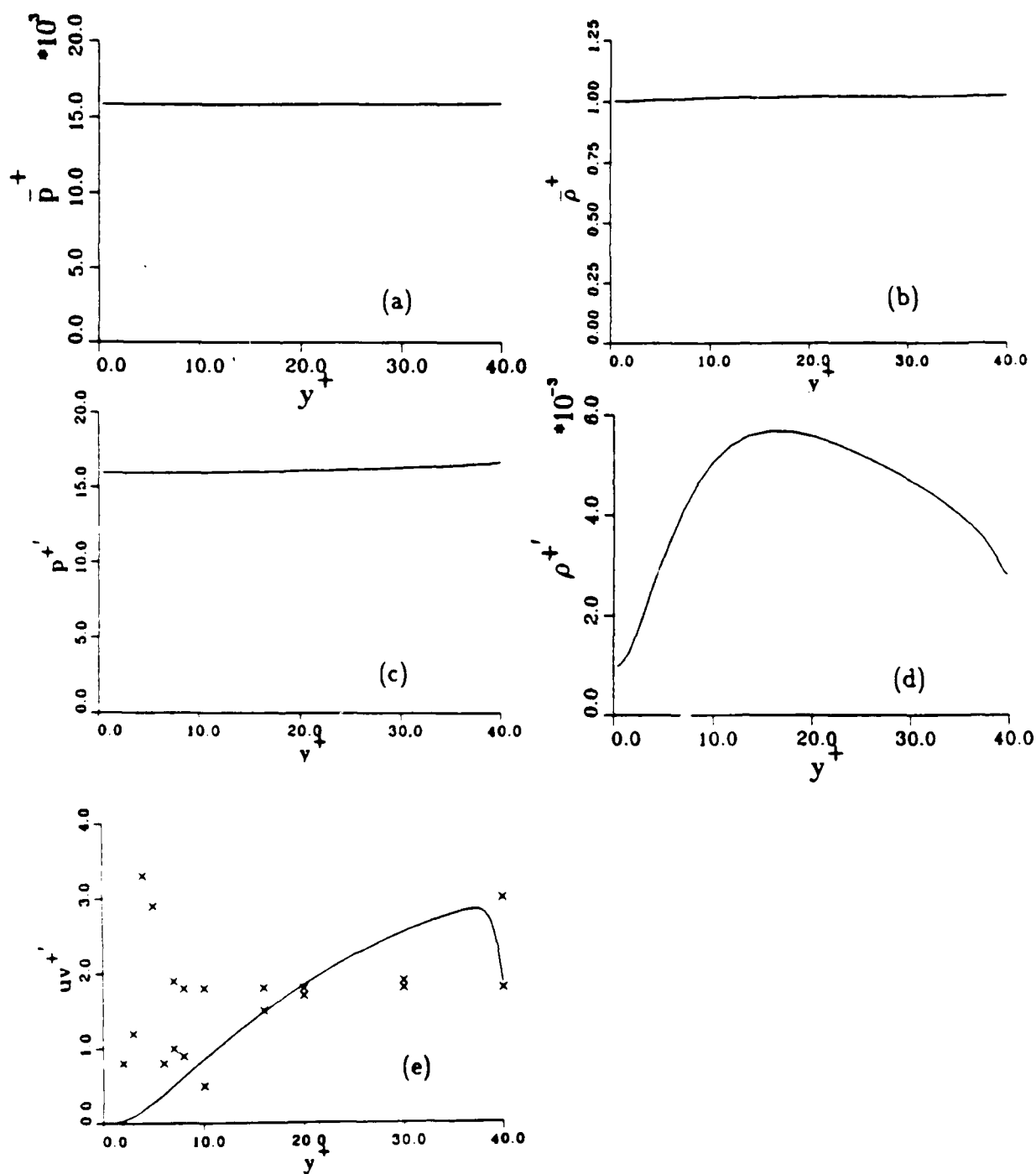
Figure 30 (a) Mean pressure $\bar{p}$.(b) Mean density $\bar{\rho}$,(c) Pressure intensity p', (d) Density intensity ρ' (e) Reynolds stress intensity $(uv)'$, $\times$ = Gupta (1972), for $Pr = 0.72$ and zero pressure gradient.

98
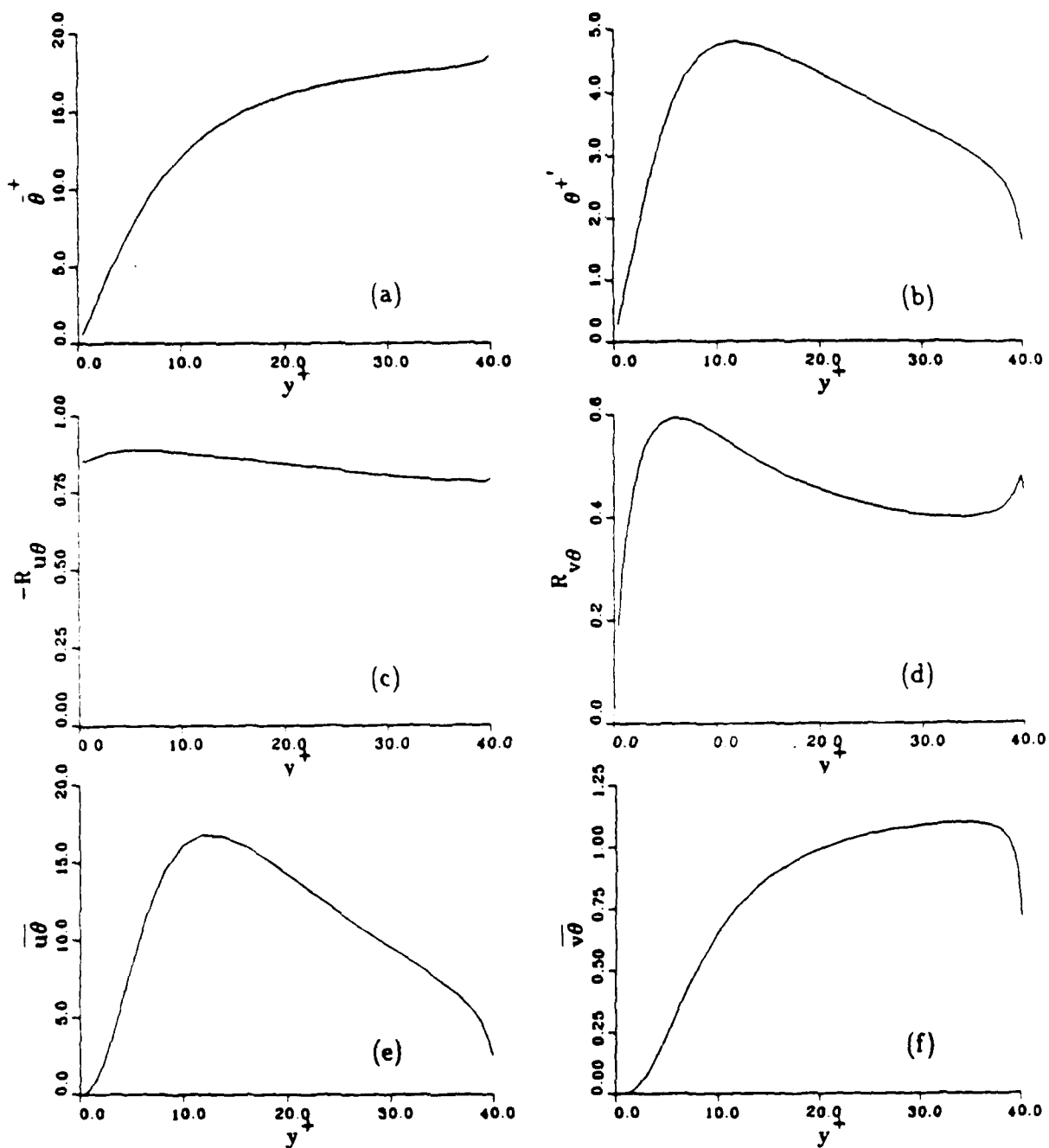
Figure 31 (a) Mean temperature $\bar{\theta}$,(b) Temperature intensity θ',(c) Correlation coefficient $R_{u\theta}$, (d) Correlation coefficient $R_{v\theta}$, (e) Correlation $\overline{u\theta}$, (f) Correlation $\overline{v\theta}$, for $Pr = 1.5$ and zero pressure gradient.

99
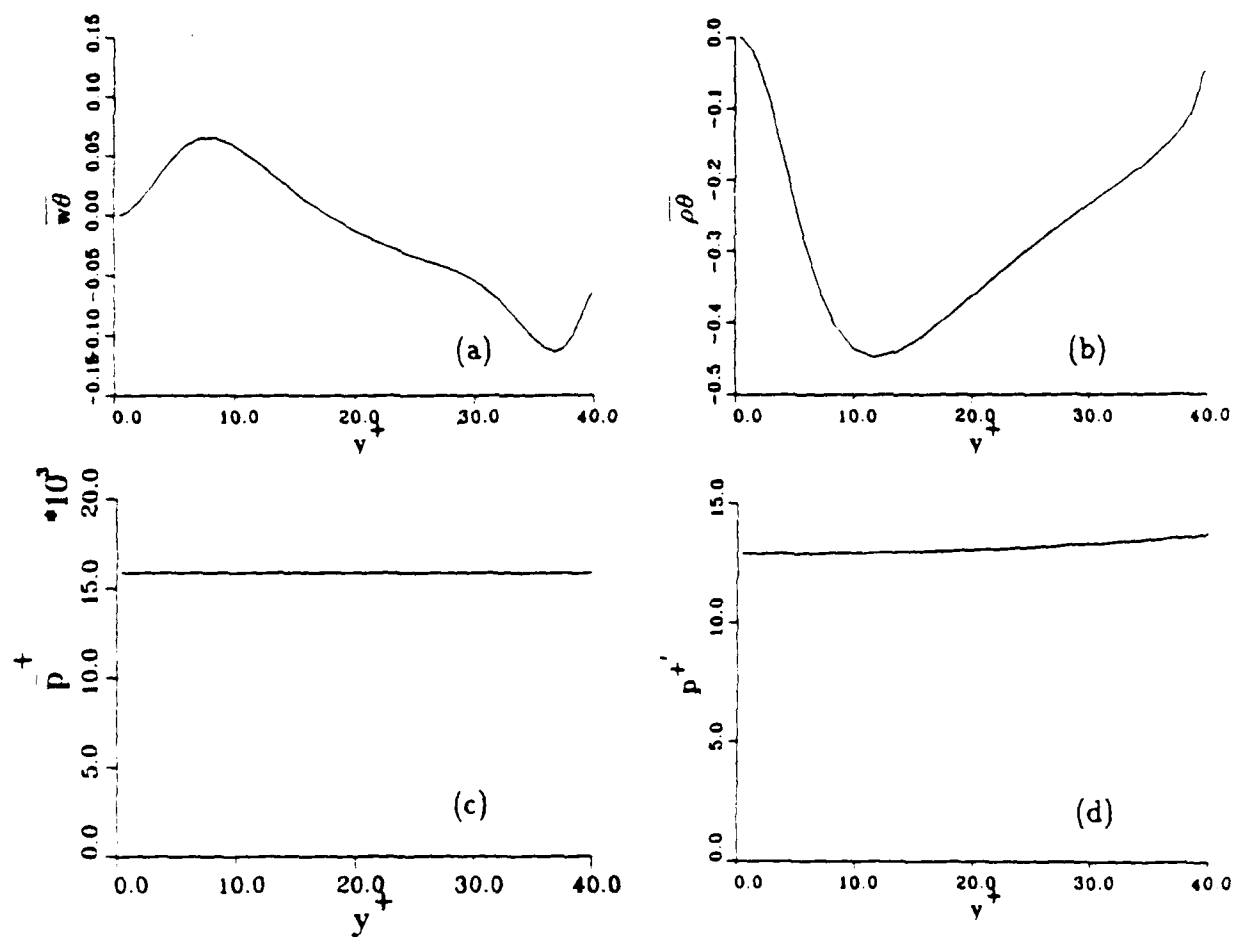
Figure 32 (a) Correlation $\overline{w\theta}$, (b) Correlation $\overline{\rho\theta}$, (c) Mean pressure $\bar{p}$, (d) Pressure intensity p', (e) Mean density $\bar{\rho}$, (f) Density intensity ρ', (g) Skewness of temperature S_θ, (h) Flatness of temperature F_θ, for $Pr = 1.5$ and zero pressure gradient.

100
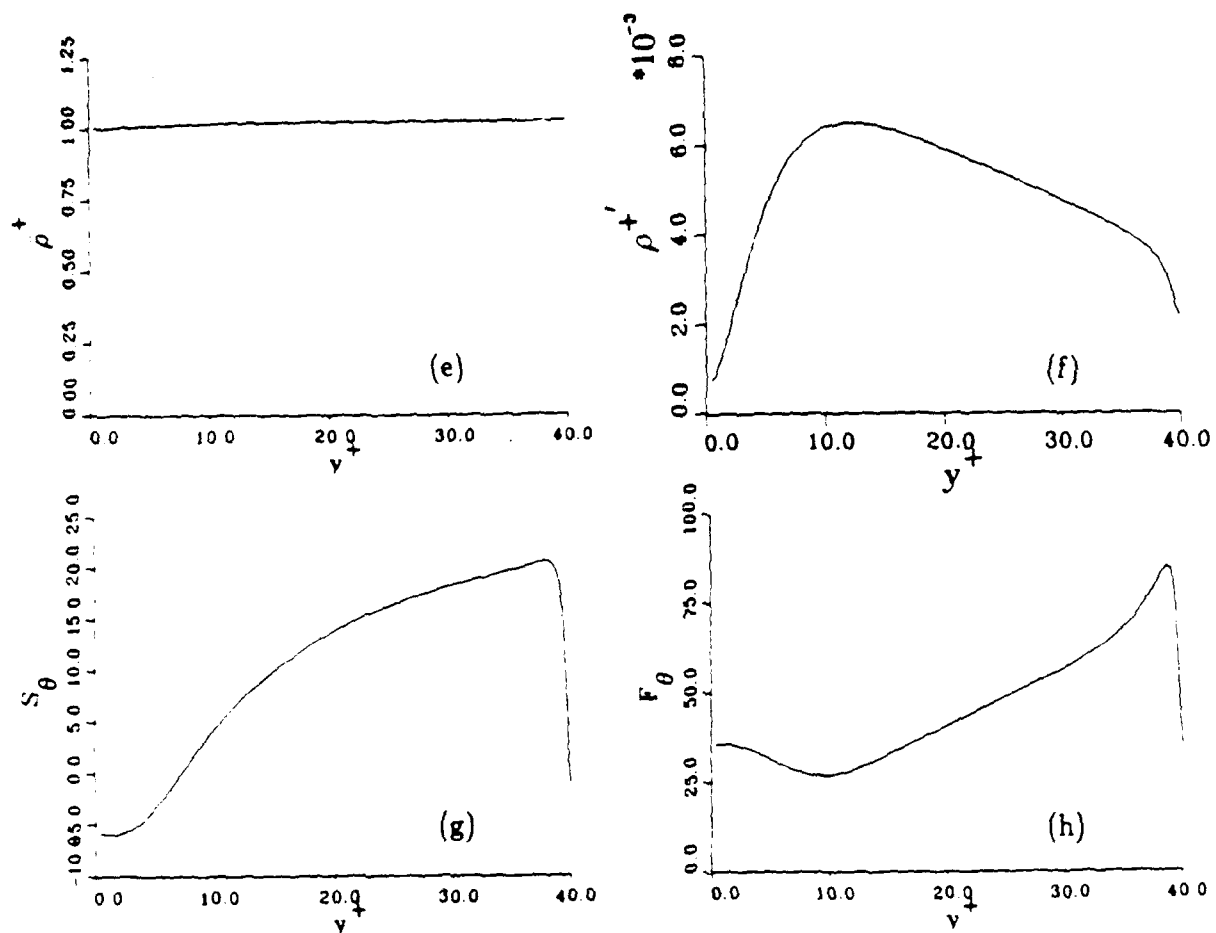
Figure 32 (continued)

101
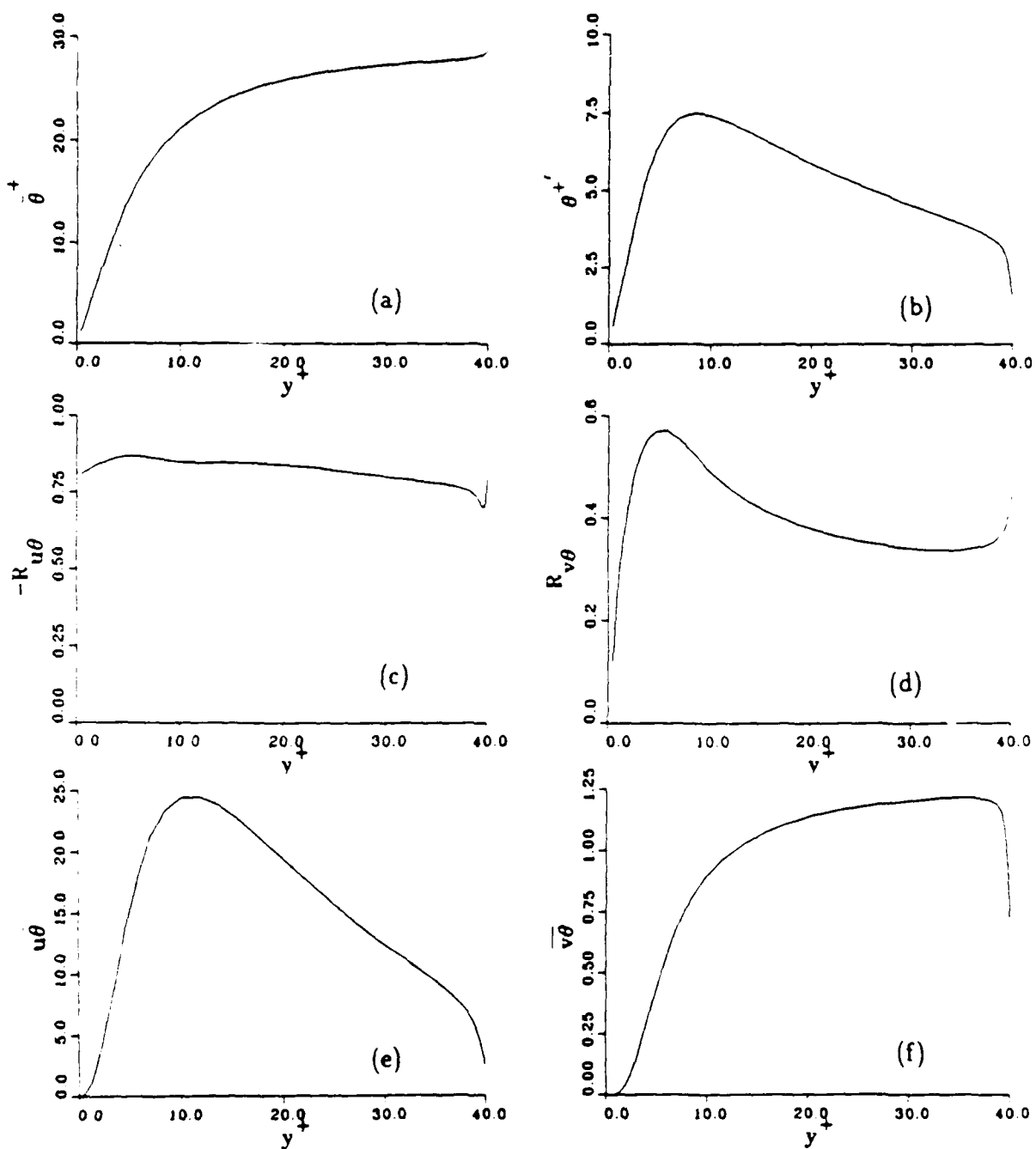
Figure 33 (a) Mean temperature $\bar{\theta}$. (b) Temperature intensity θ'. (c) Correlation coefficient $R_{u\theta}$. (d) Correlation coefficient $R_{v\theta}$. (e) Correlation $\overline{u\theta}$. (f) Correlation $\overline{v\theta}$. for $Pr = 3.0$ and zero pressure gradient.

102
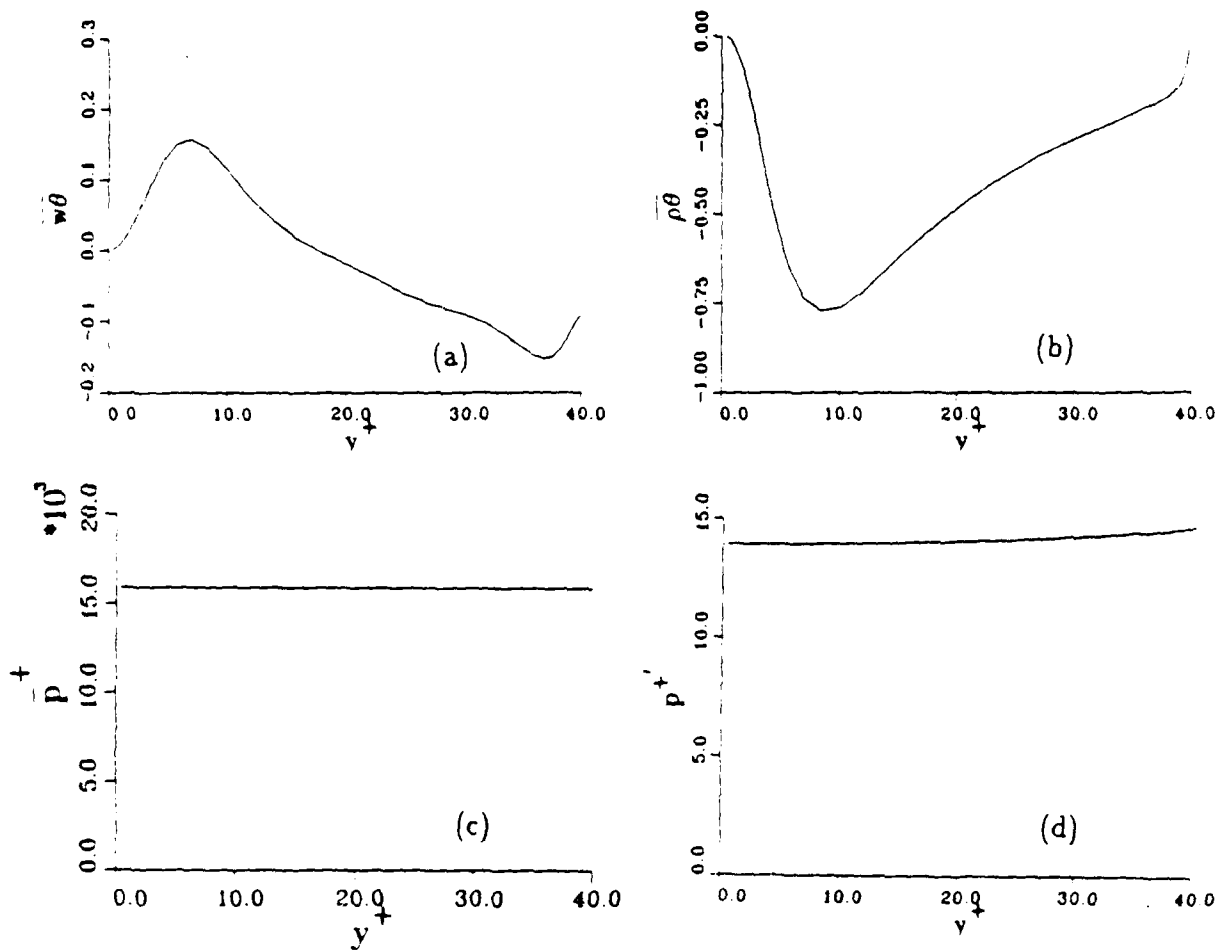
Figure 34 (a) Correlation $\overline{u\theta}$, (b) Correlation $\overline{\rho\theta}$, (c) Mean pressure $\bar{p}$. (d) Pressure intensity p'. (e) Mean density $\bar{\rho}$. (f) Density intensity ρ', (g) Skewness of temperature S_θ (h) Flatness of temperature F_θ, for $Pr = 3.0$ and zero pressure gradient.

103
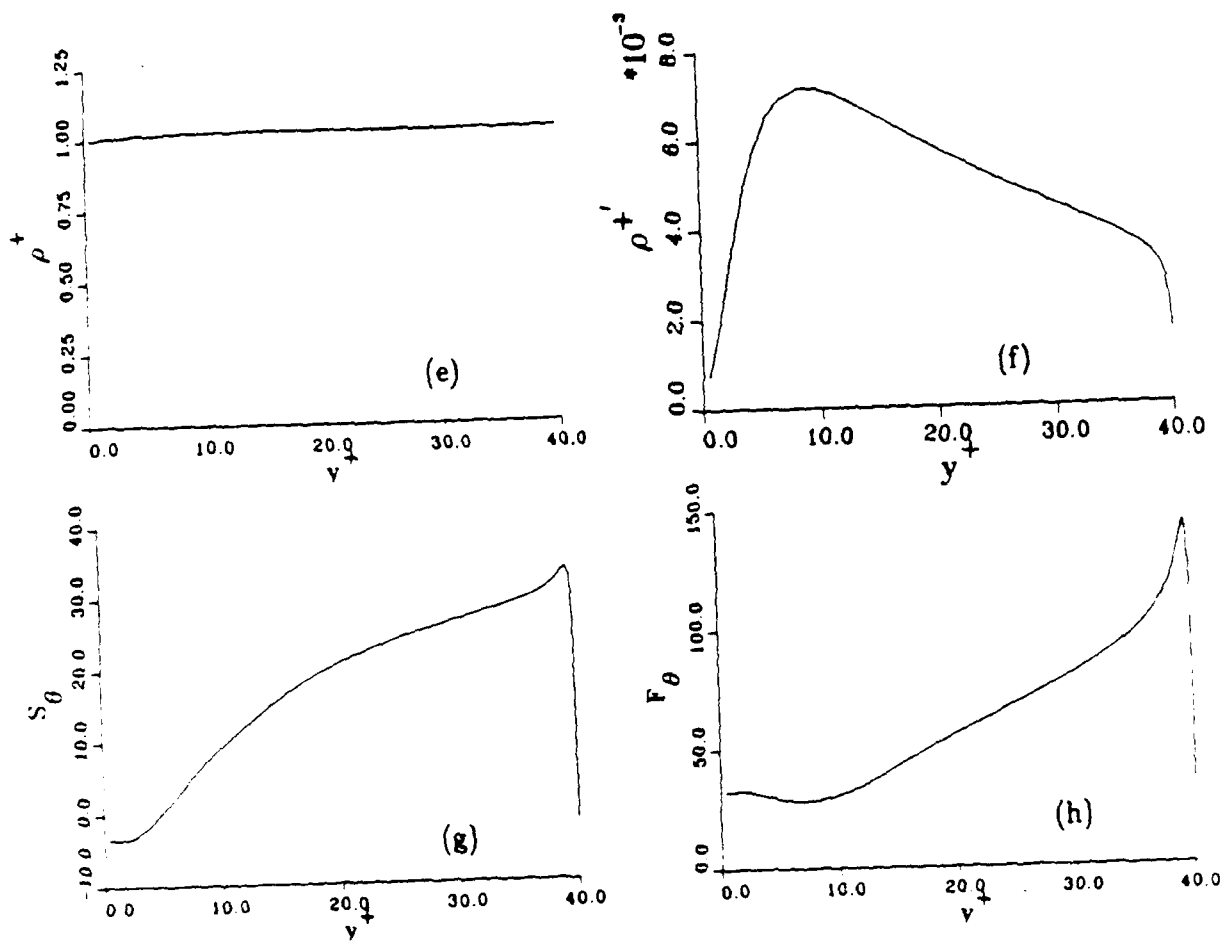
Figure 34 (continued)

104
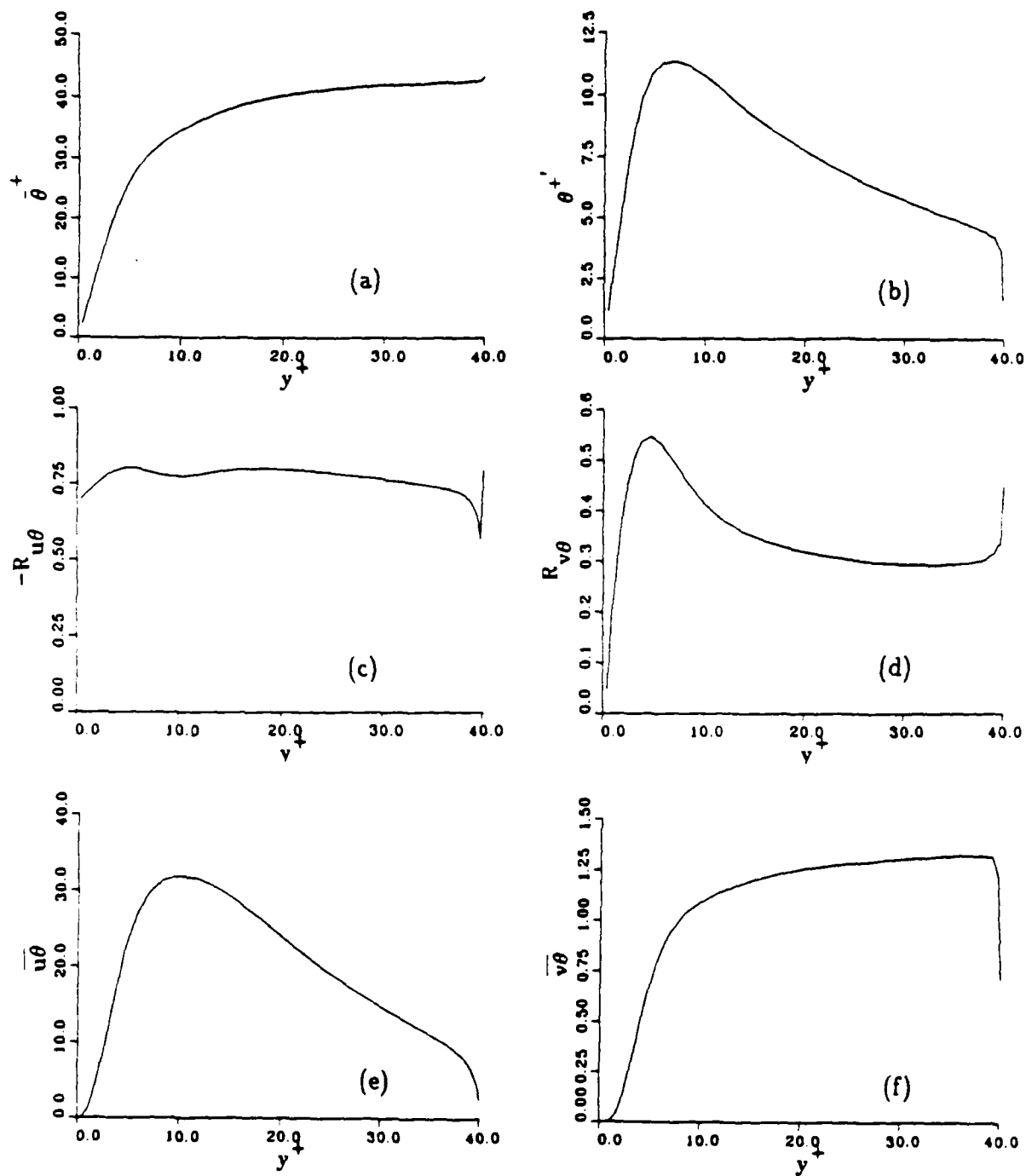
Figure 35 (a) Mean temperature $\bar{\theta}$,(b) Temperature intensity θ',(c) Correlation coefficient $R_{u\theta}$, (d) Correlation coefficient $R_{v\theta}$, (e) Correlation $\overline{u\theta}$, (f) Correlation $\overline{v\theta}$, for $Pr = 6.0$ and zero pressure gradient.

105
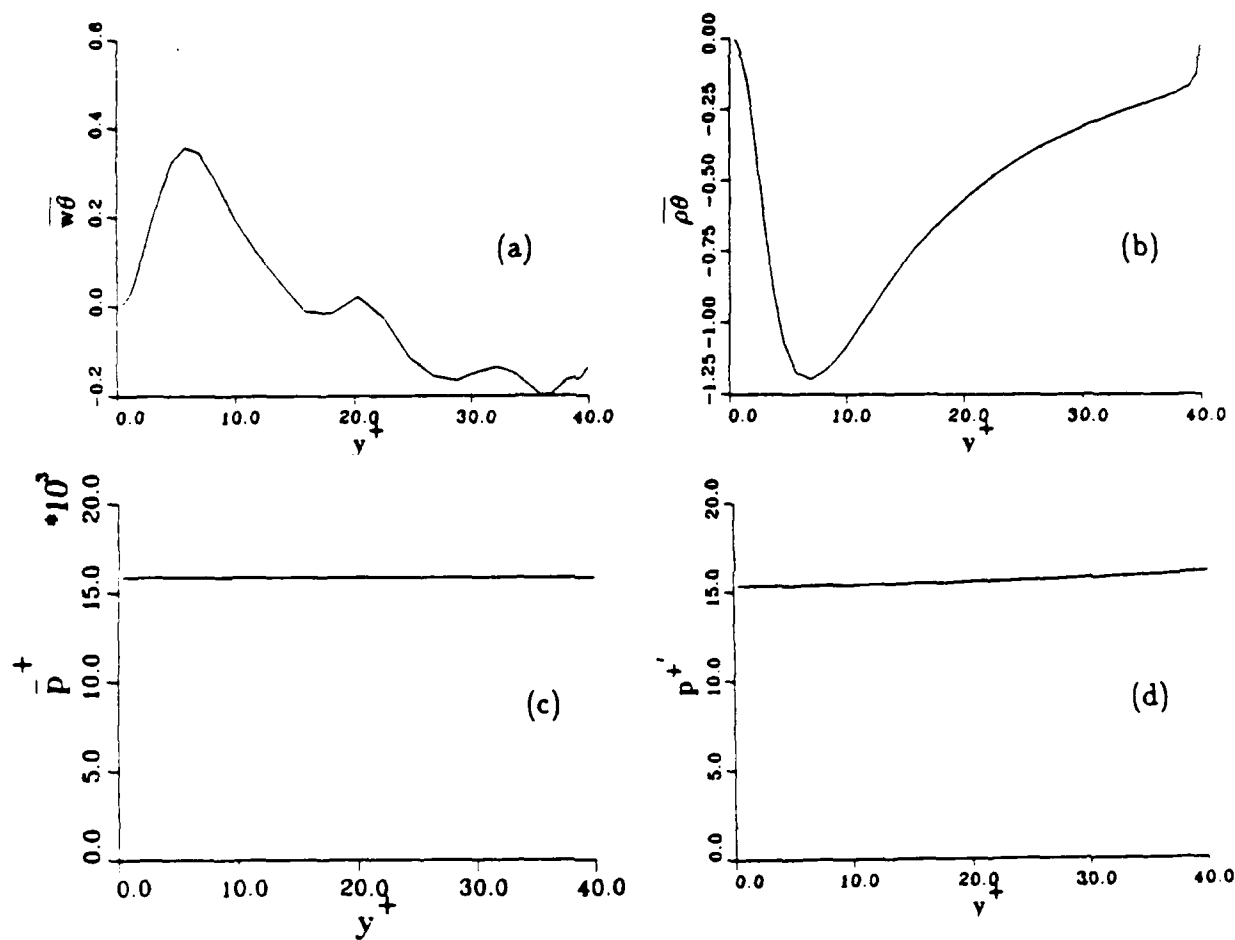
Figure 36 (a) Correlation $\overline{w\theta}$, (b) Correlation $\overline{\rho\theta}$, (c) Mean pressure $\bar{p}$, (d) Pressure intensity p', (e) Mean density $\bar{\rho}$, (f) Density intensity ρ', (g) Skewness of temperature S_θ (h) Flatness of temperature F_θ, for $Pr = 6.0$ and zero pressure gradient.
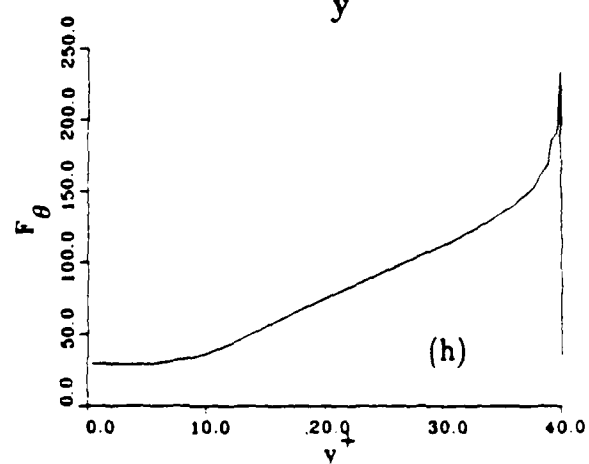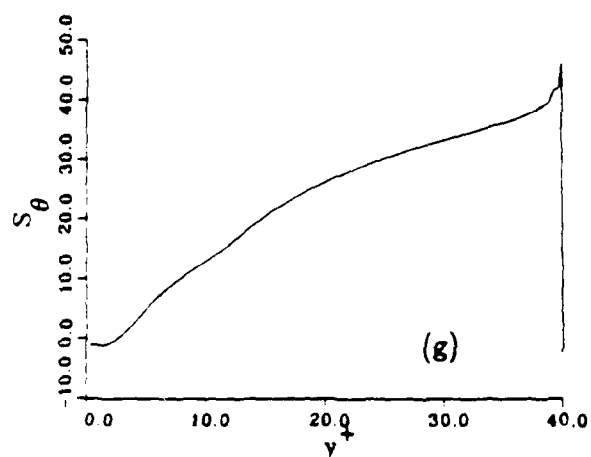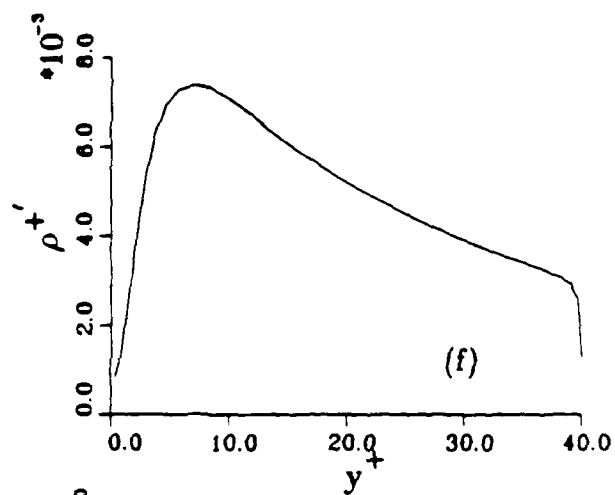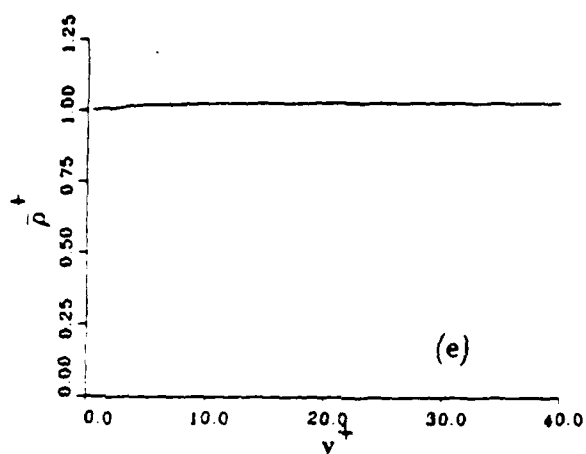
Figure 36 (continued)

107
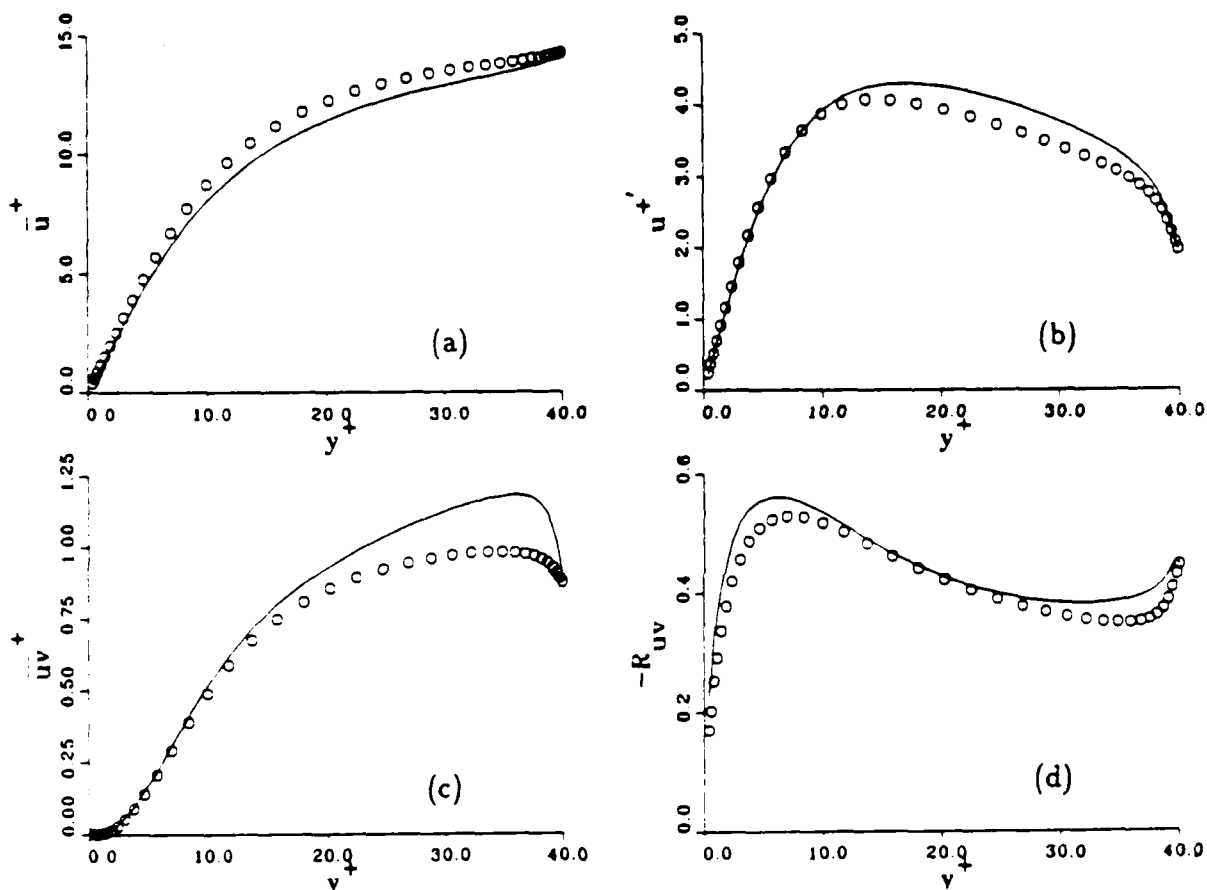
Figure 37 (a) Mean streamwise velocity $\bar{u}$, (b) Streamwise velocity intensity u', (c) Reynolds stress $-\overline{uv}$, (d) Reynolds stress correlation coefficient $-R_{uv}$, (e) Mean temperature $\bar{\theta}$,(f) Temperature intensity θ',(g) Correlation coefficient $-R_{u\theta}$, (h) Correlation coefficient $R_{v\theta}$, for $Pr = 0.72$ and $\dfrac{\partial \bar{p}}{\partial x} = .01$, $\circ$ = zero pressure gradient case.

108
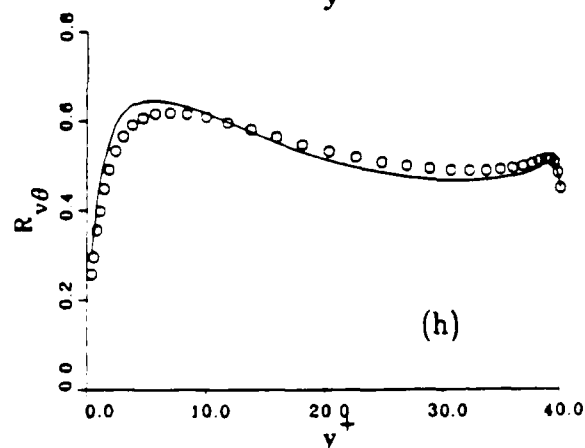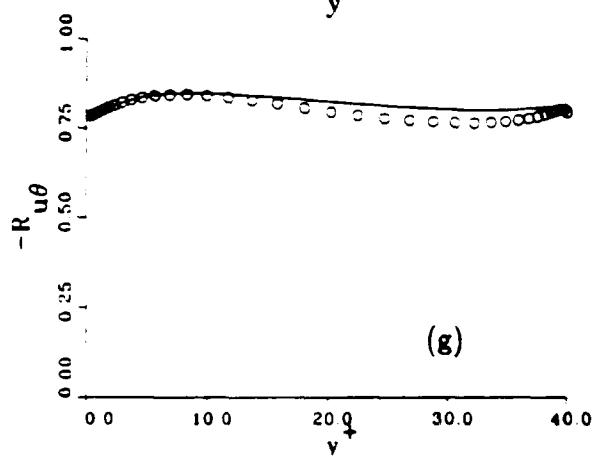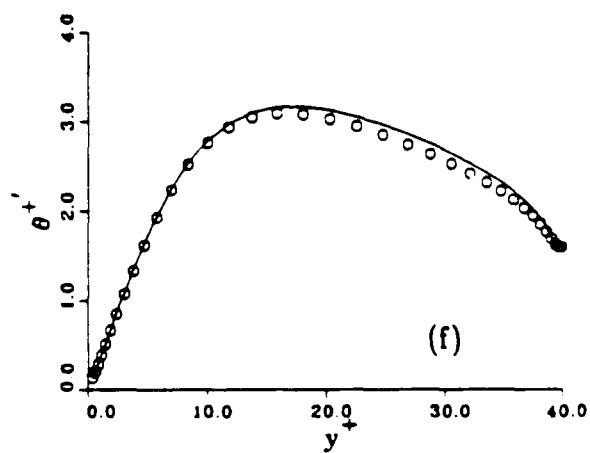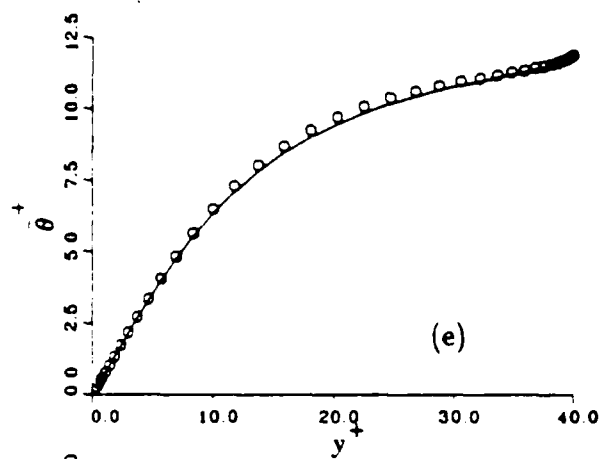
Figure 37 (continued)

109
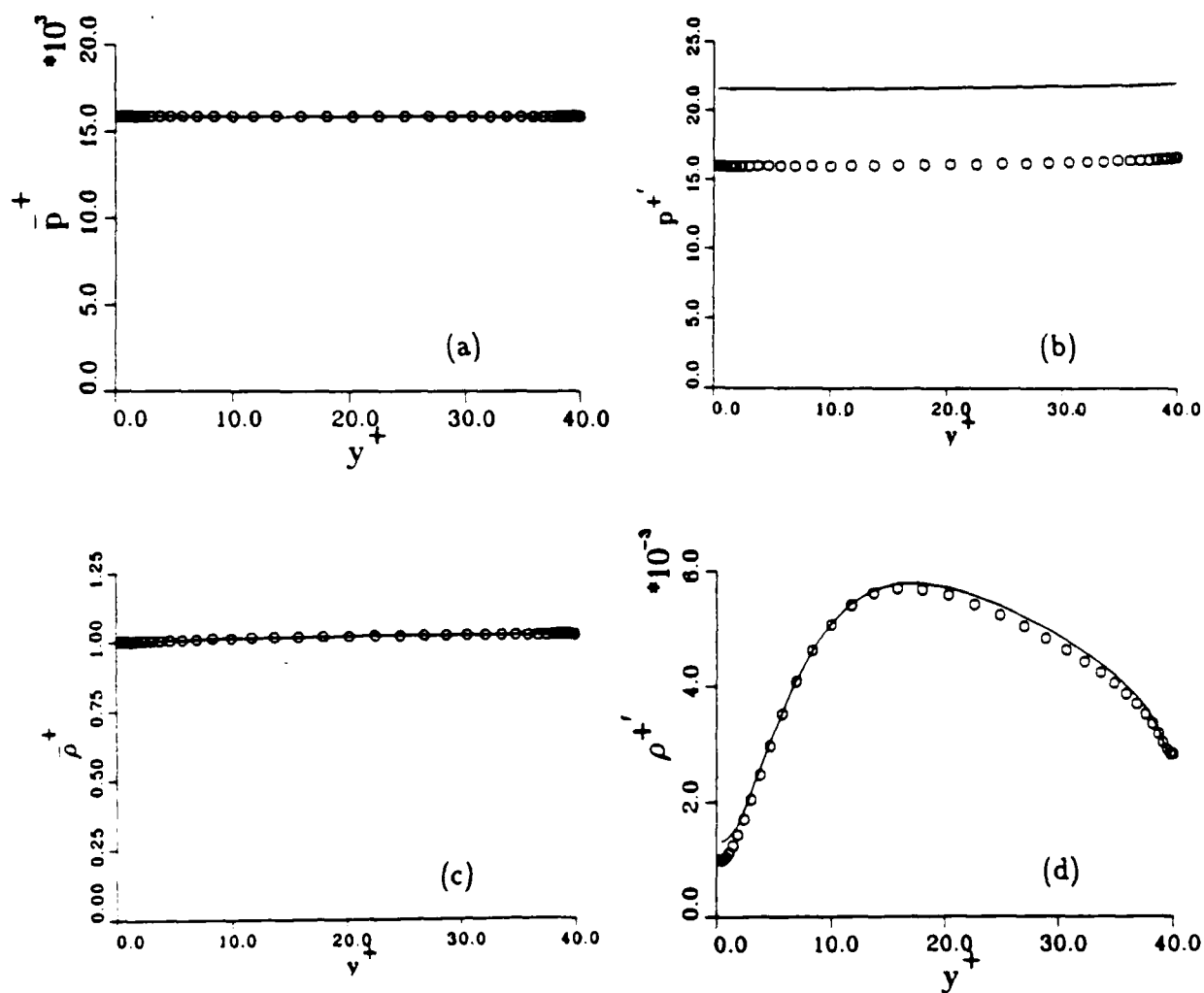
Figure 38 (a) Mean pressure $\bar{p}$, (b) Pressure intensity p', (c) Mean density $\bar{\rho}$, (d) Density intensity ρ', for $Pr = 0.72$ and $\dfrac{\partial \bar{p}}{\partial x} = .01$, $\circ$ = zero pressure gradient case.

110
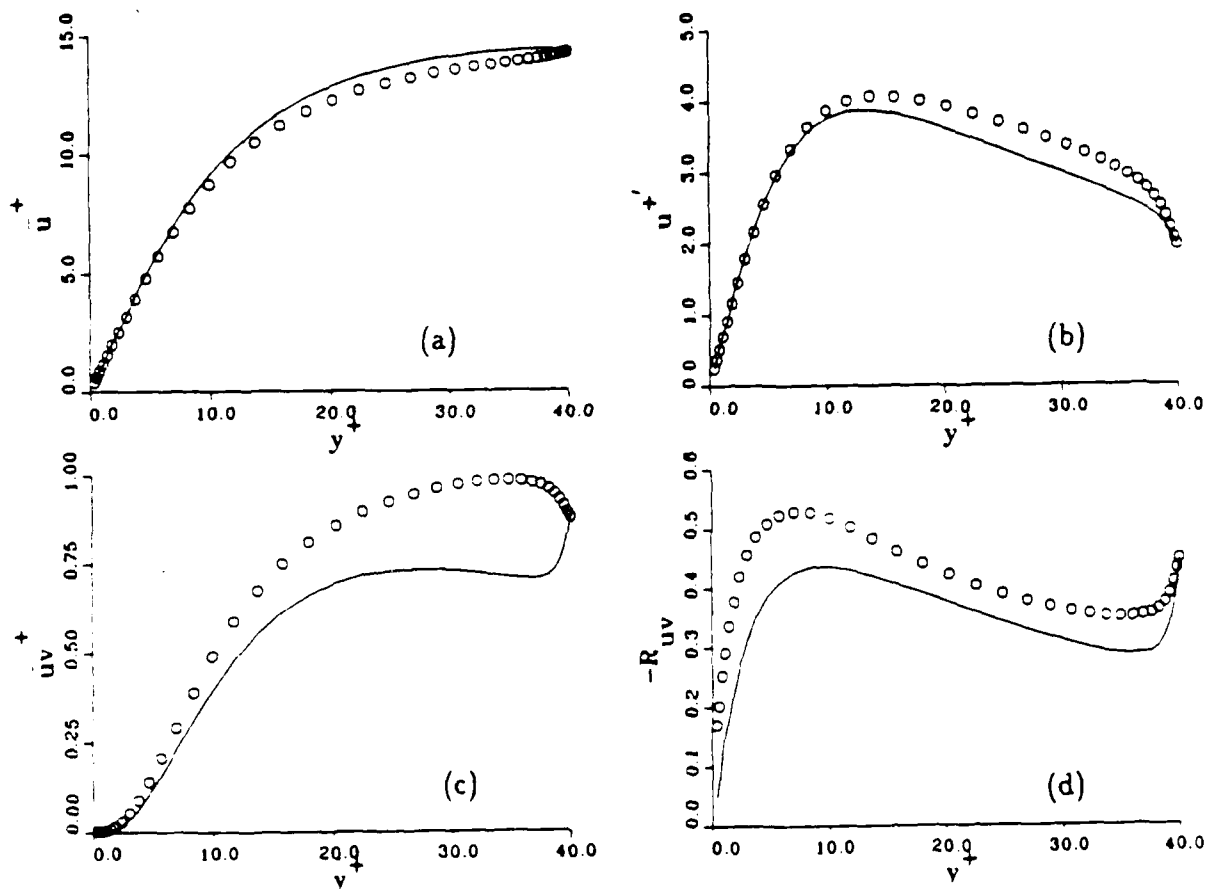
Figure 39 (a) Mean streamwise velocity $\bar{u}$. (b) Streamwise velocity intensity u', (c) Reynolds stress $-\overline{uv}$. (d) Reynolds stress correlation coefficient $-R_{uv}$, (e) Mean temperature $\bar{\theta}$.(f) Temperature intensity θ',(g) Correlation coefficient $-R_{u\theta}$, (h) Correlation coefficient $R_{t\theta}$. for $Pr = 0.72$ and $\dfrac{\partial \bar{p}}{\partial x} = -.01$, $\circ$ = zero pressure gradient case.

111
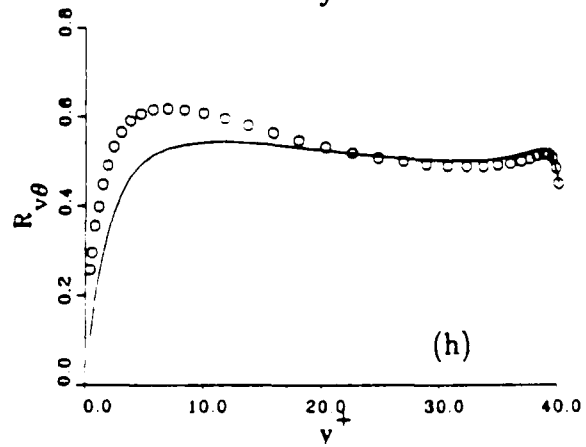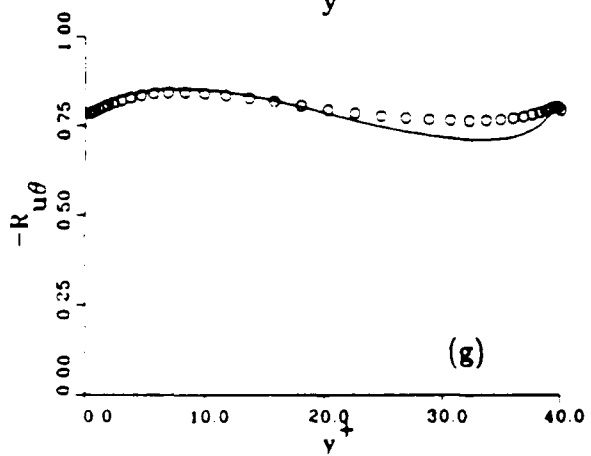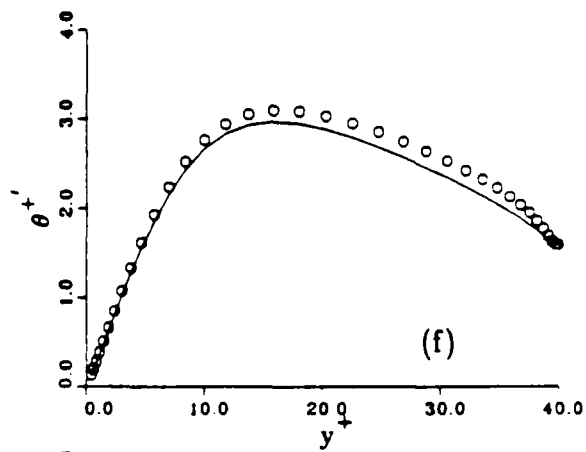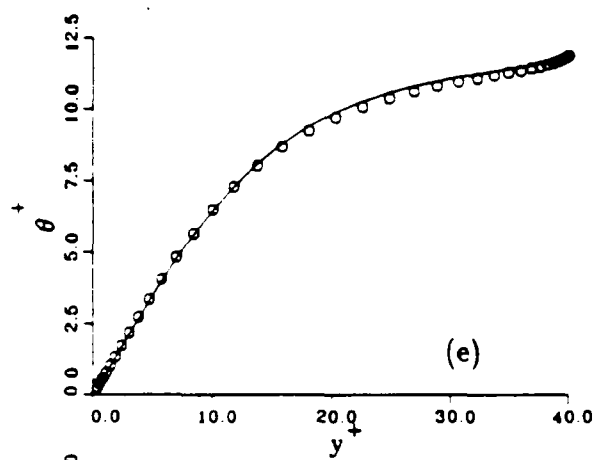
Figure 39 (continued)

112
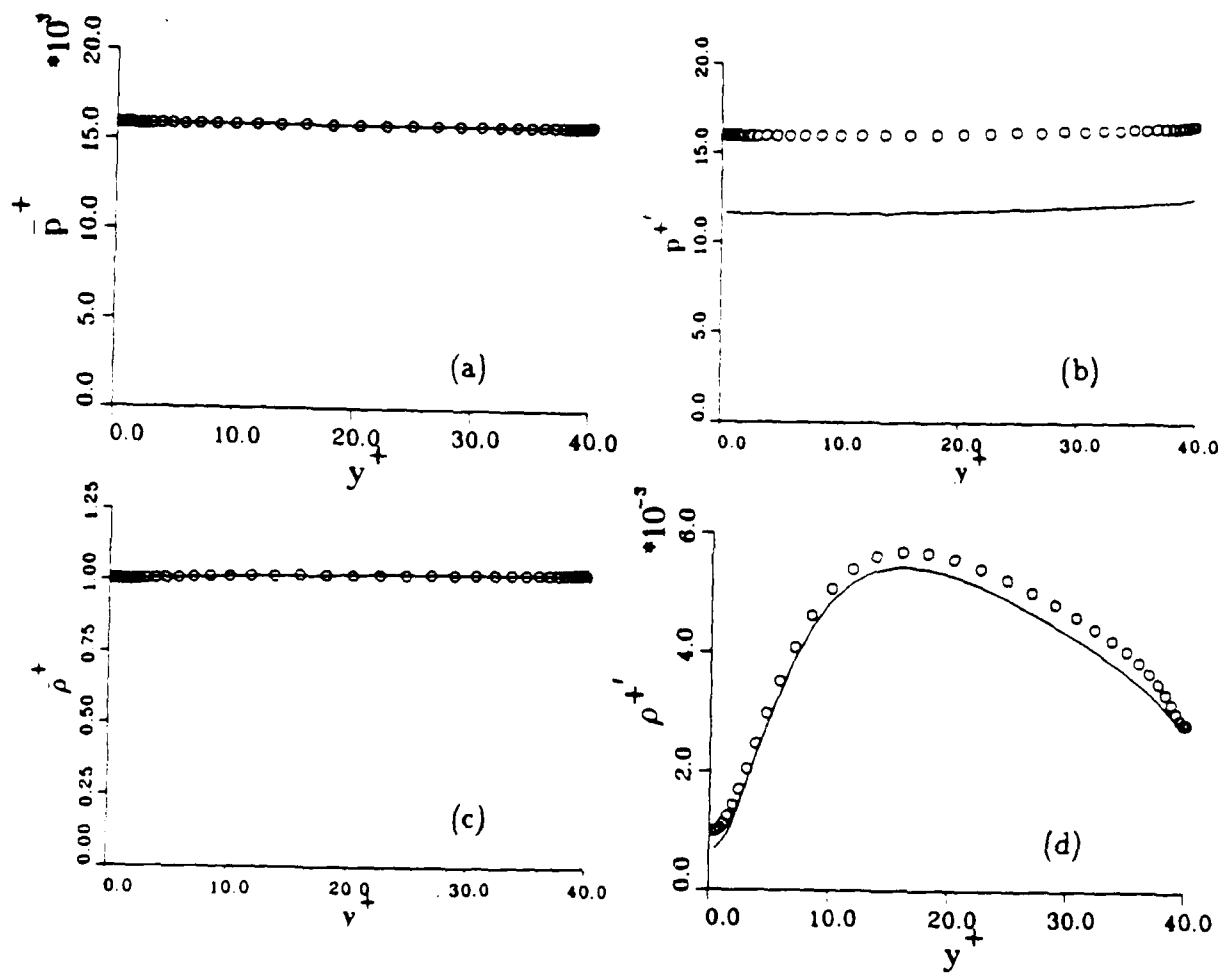
Figure 40 (a) Mean pressure $\bar{p}$. (b) Pressure intensity p', (c) Mean density $\bar{\rho}$, (d) Density intensity ρ', for $Pr = 0.72$ and $\dfrac{\partial \bar{p}}{\partial x} = -.01$, $\circ$ = zero pressure gradient case.

113
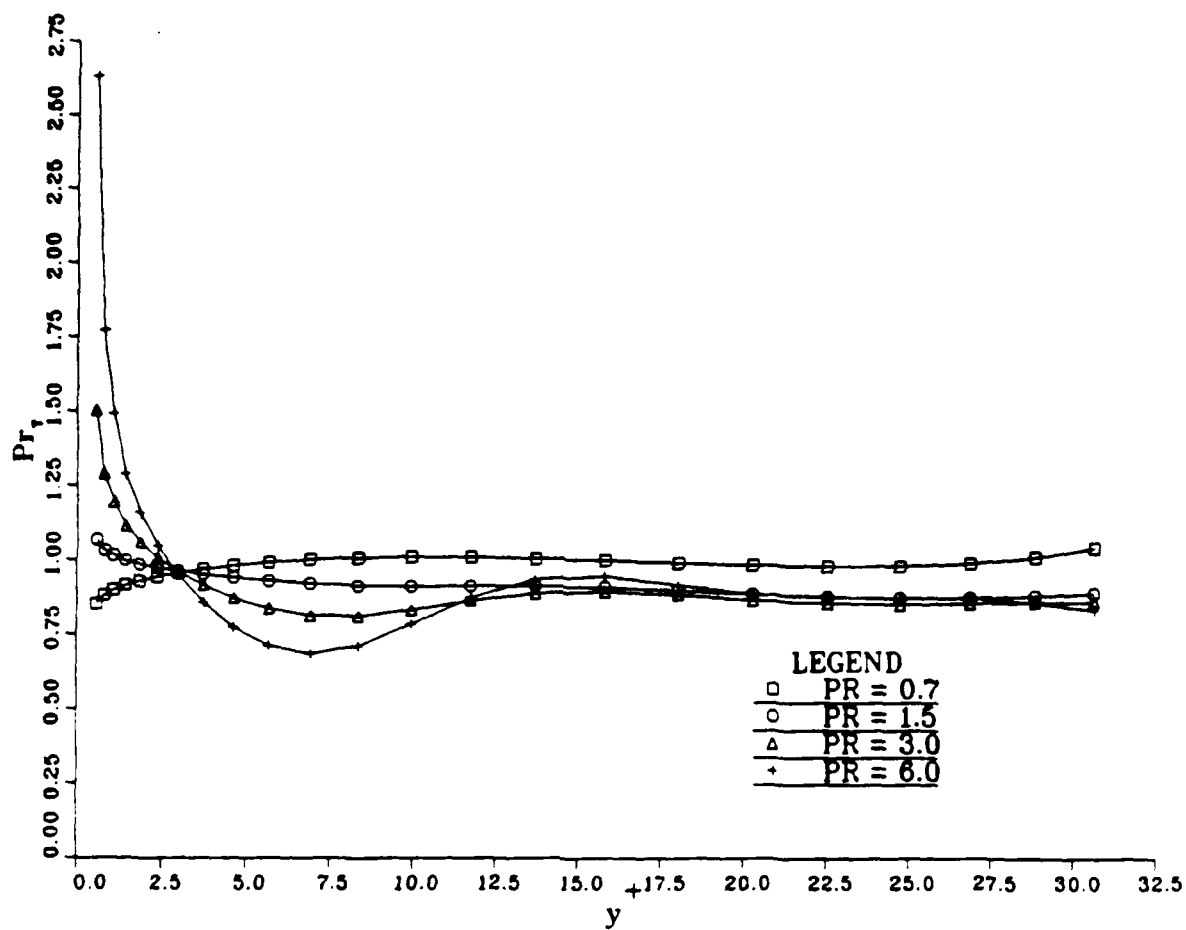
Figure 41 Turbulent Prandtl number as a function of y^+ for different molecular Prandtl numbers.

114
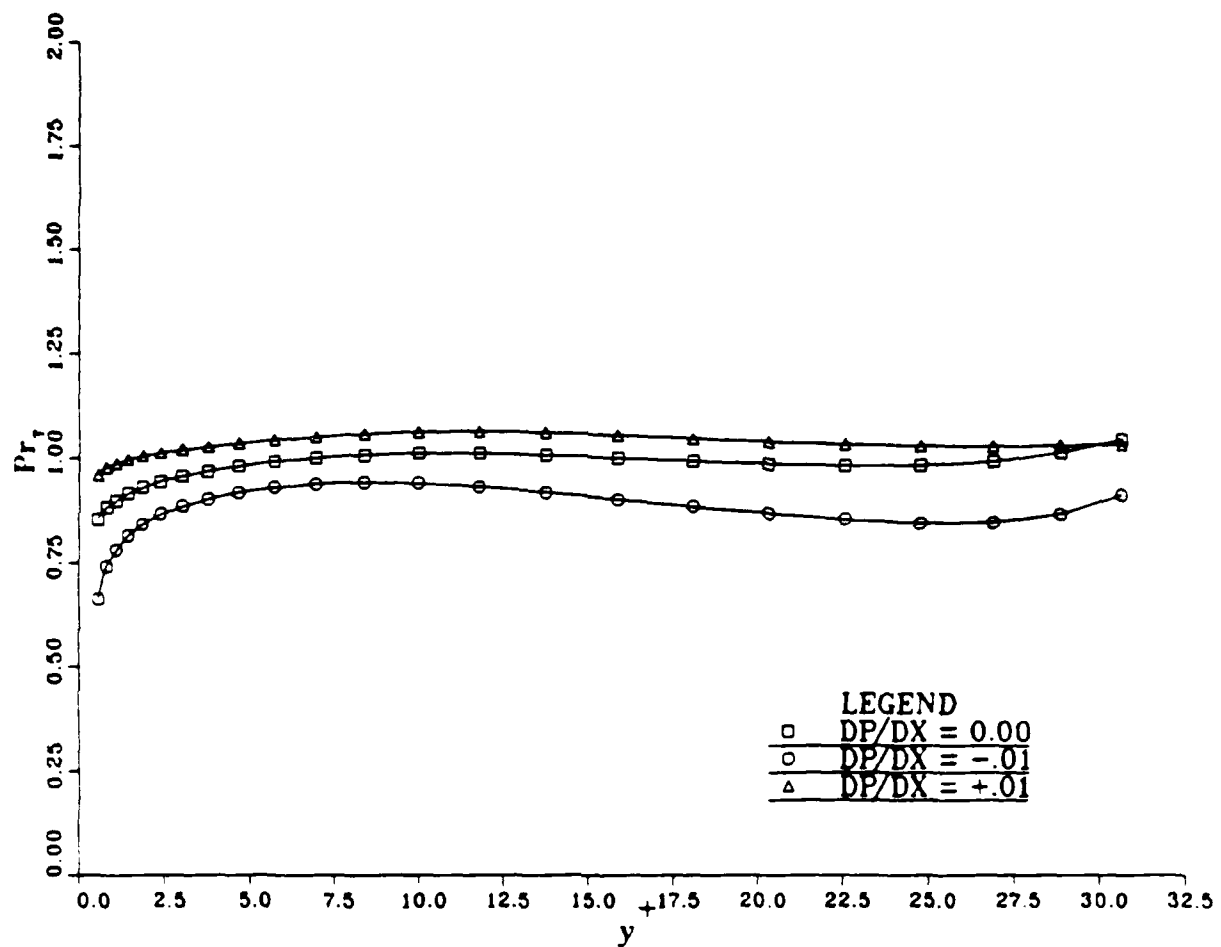
Figure 42 Turbulent Prandtl number as a function of y^+ for different mean streamwise pressure gradients.
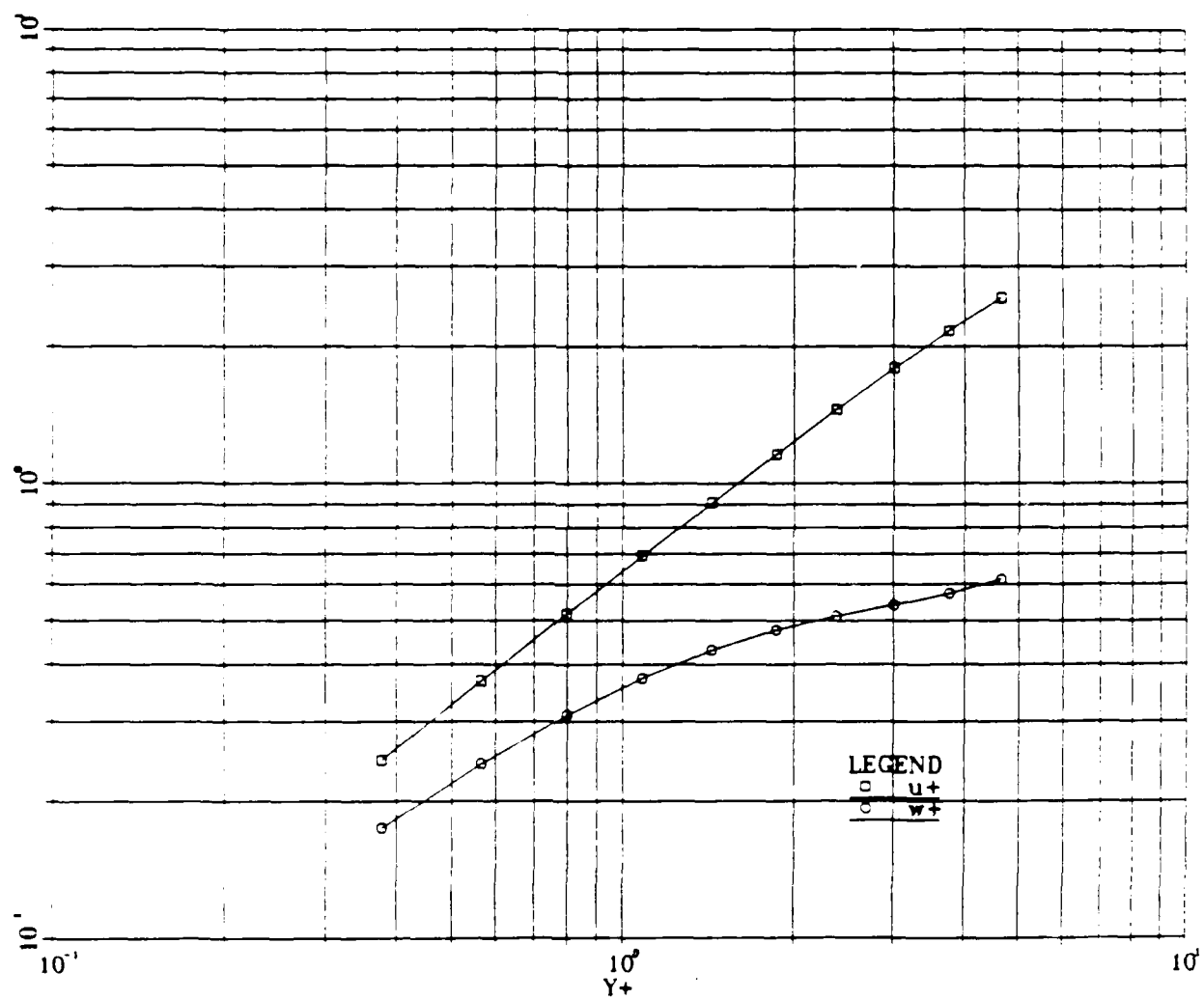
Figure 43 Log-log plots of computed u' and w' for $Pr = 0.72$.

116
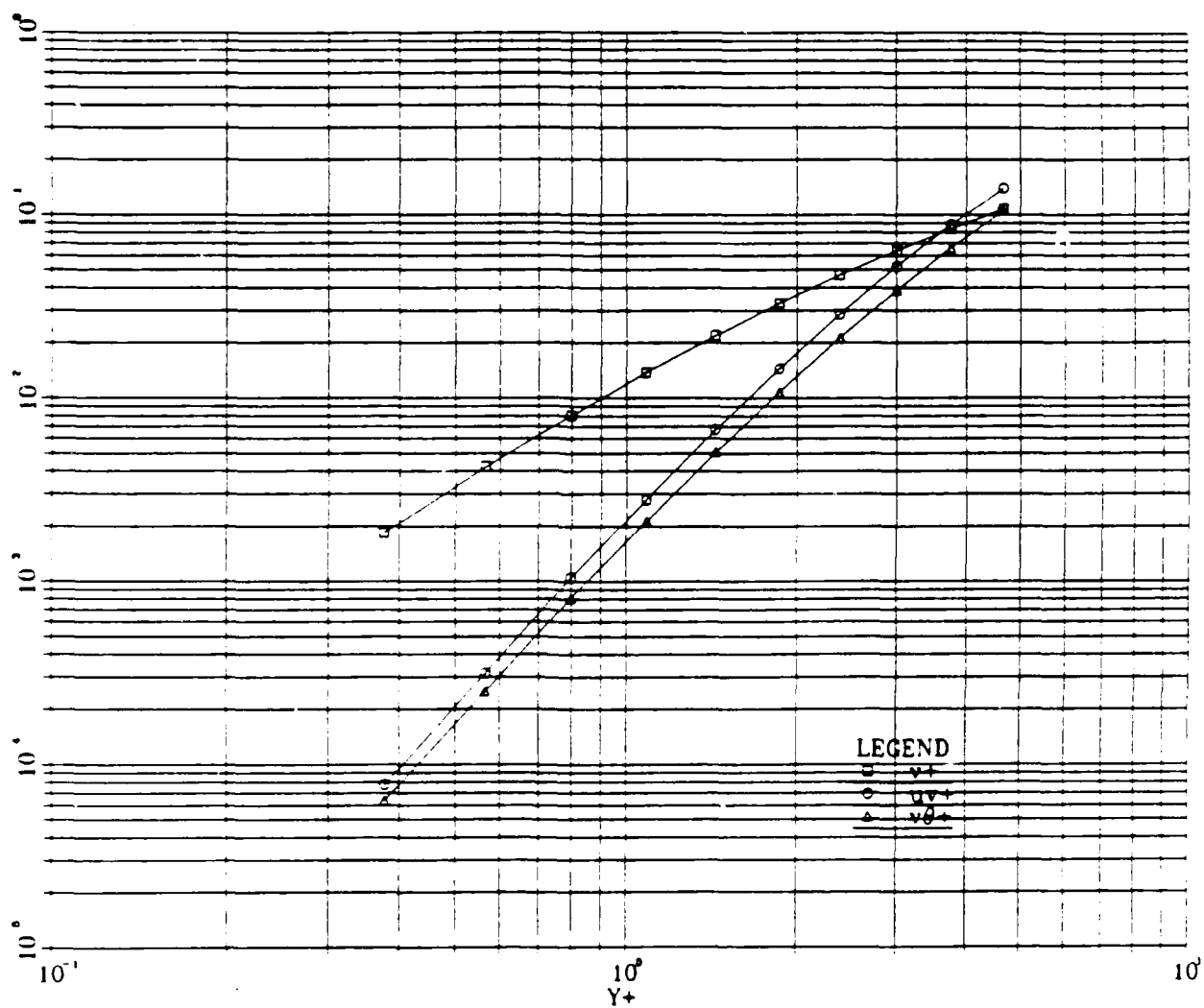
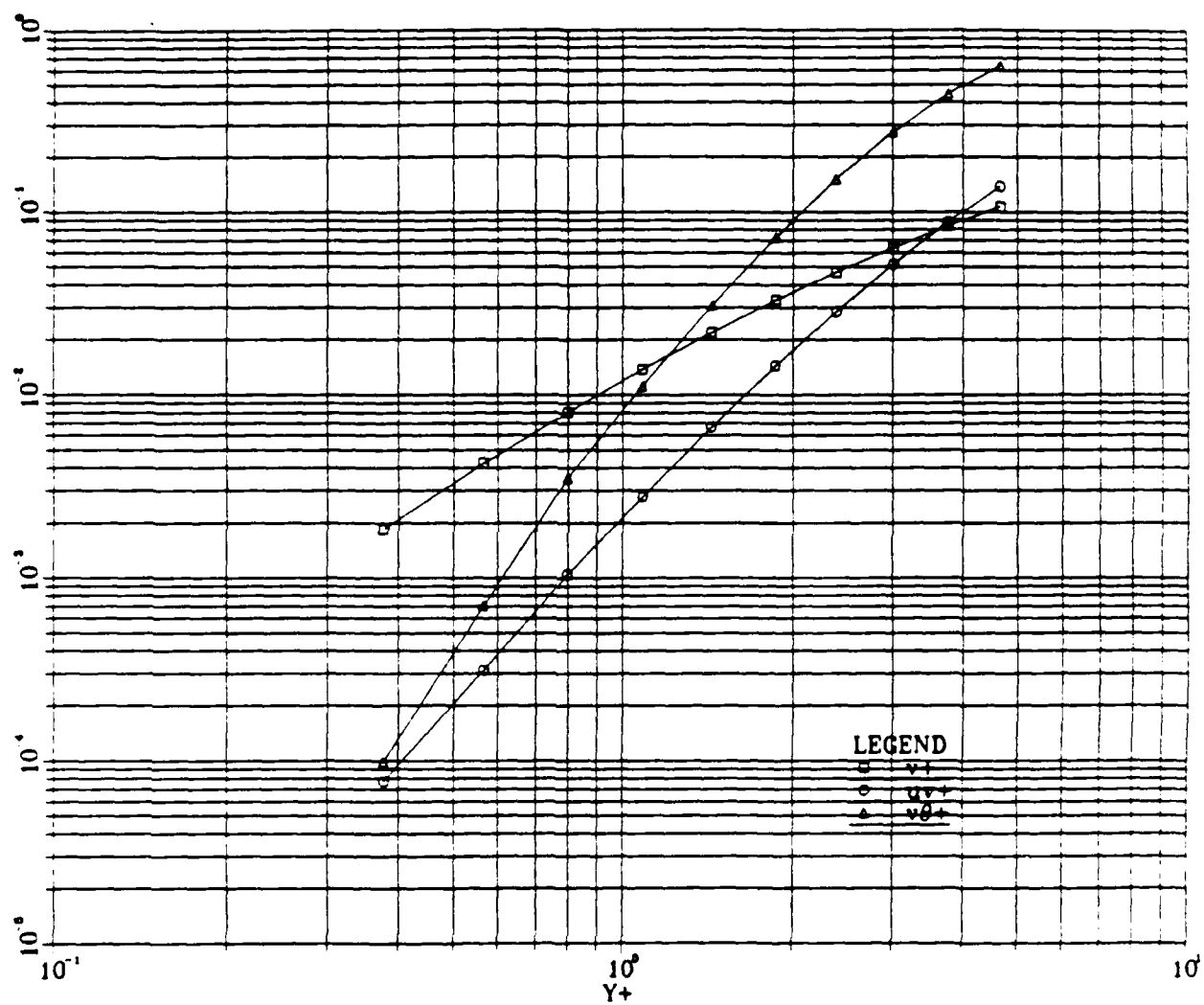Figure 44 Log-log plots of computed v' and $\overline{uv}^+$ and $\overline{v\theta}^+$ for $Pr = 0.72$.

117
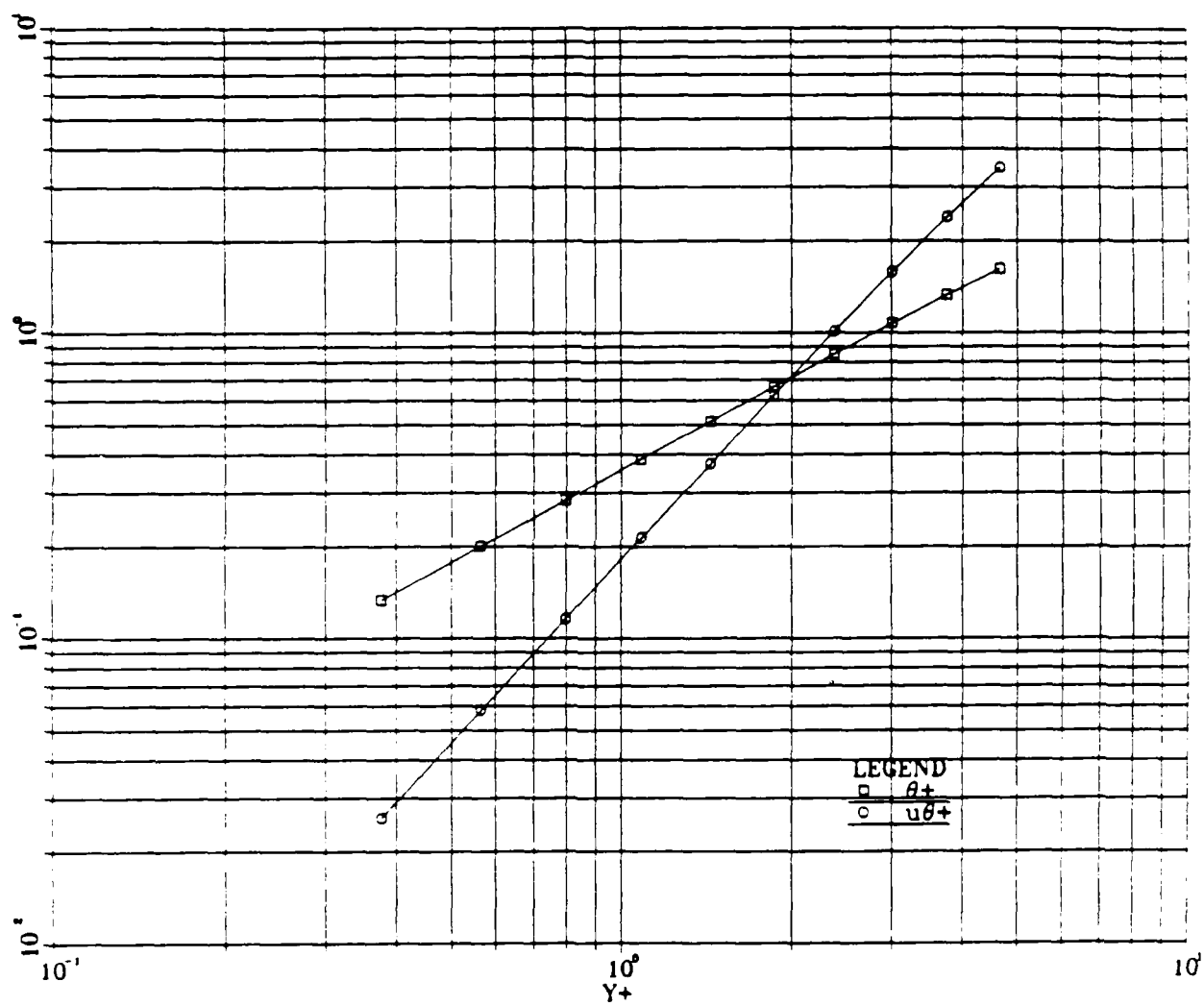
Figure 45 Log-log plots of computed θ' and $\overline{u\theta}^+$ for $Pr = 0.72$.

118
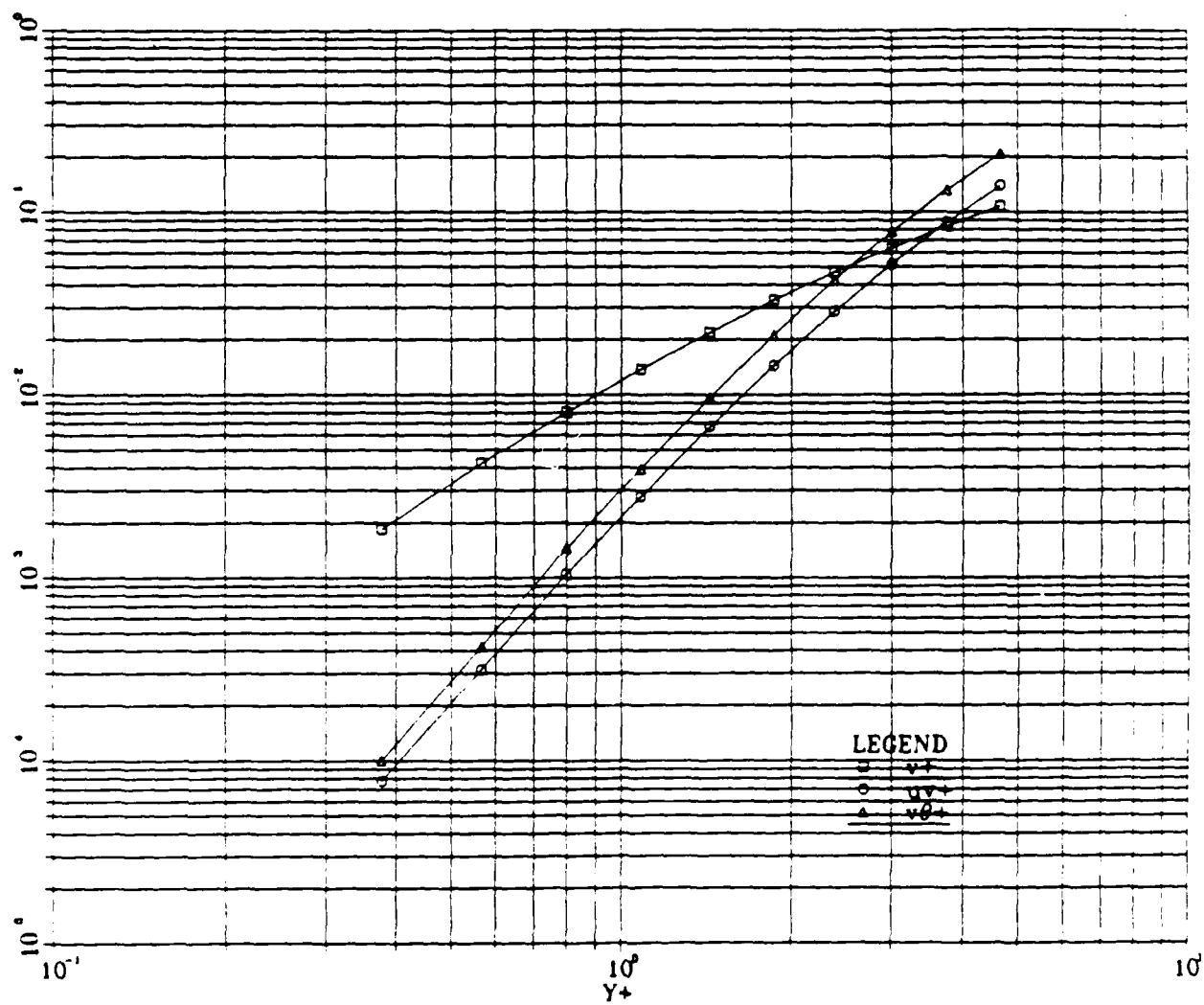
Figure 46 Log-log plots of computed v' and $\overline{uv}^+$ and $\overline{v\theta}^+$ for $Pr = 1.5$.

119
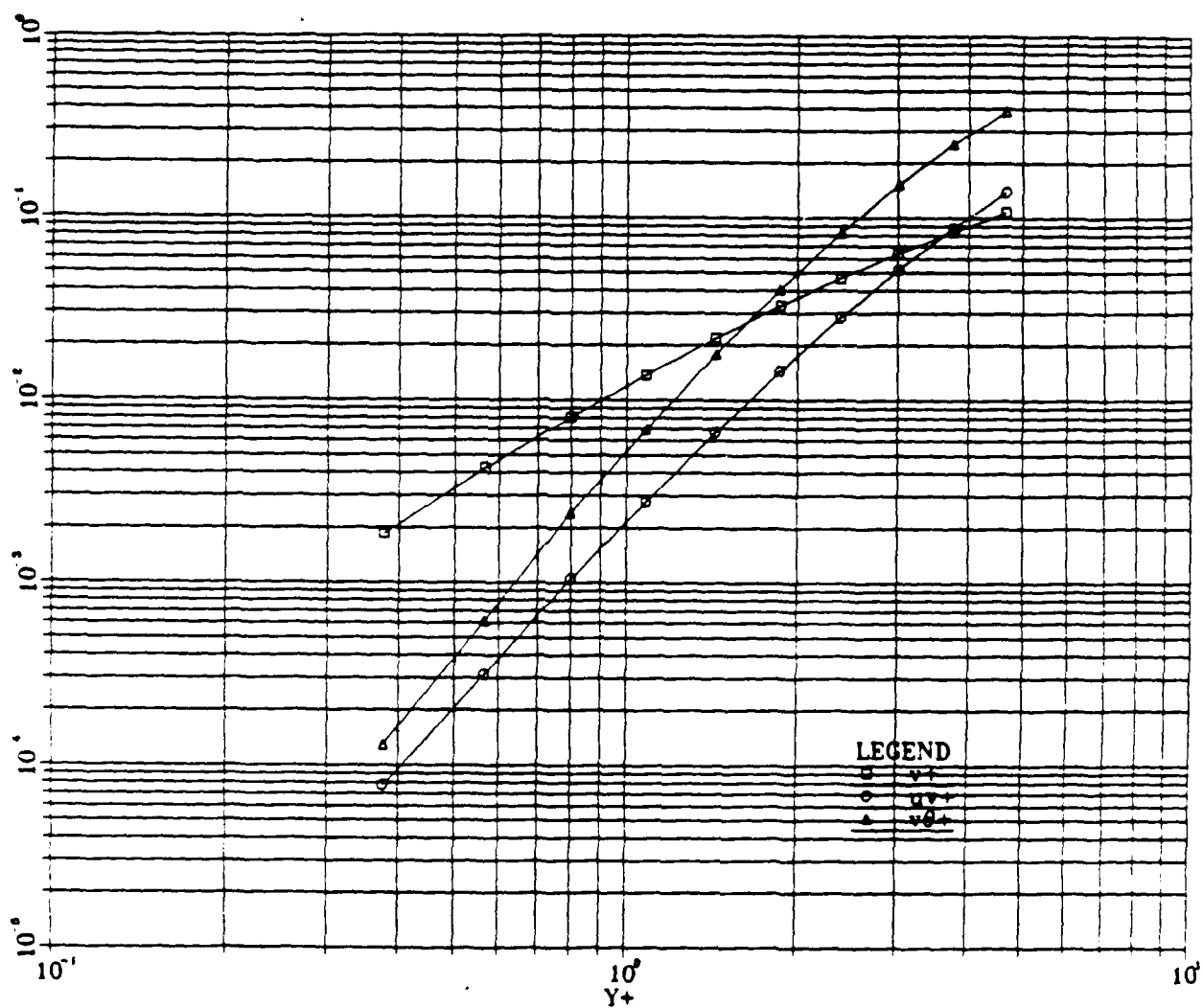
Figure 47 Log-log plots of computed v' and $\overline{uv}^+$ and $\overline{v\theta}^+$ for $Pr = 3.0$.

120

Figure 48 Log-log plots of computed v' and $\overline{uv}^+$ and $\overline{v\theta}^+$ for $Pr = 6.0$.

121
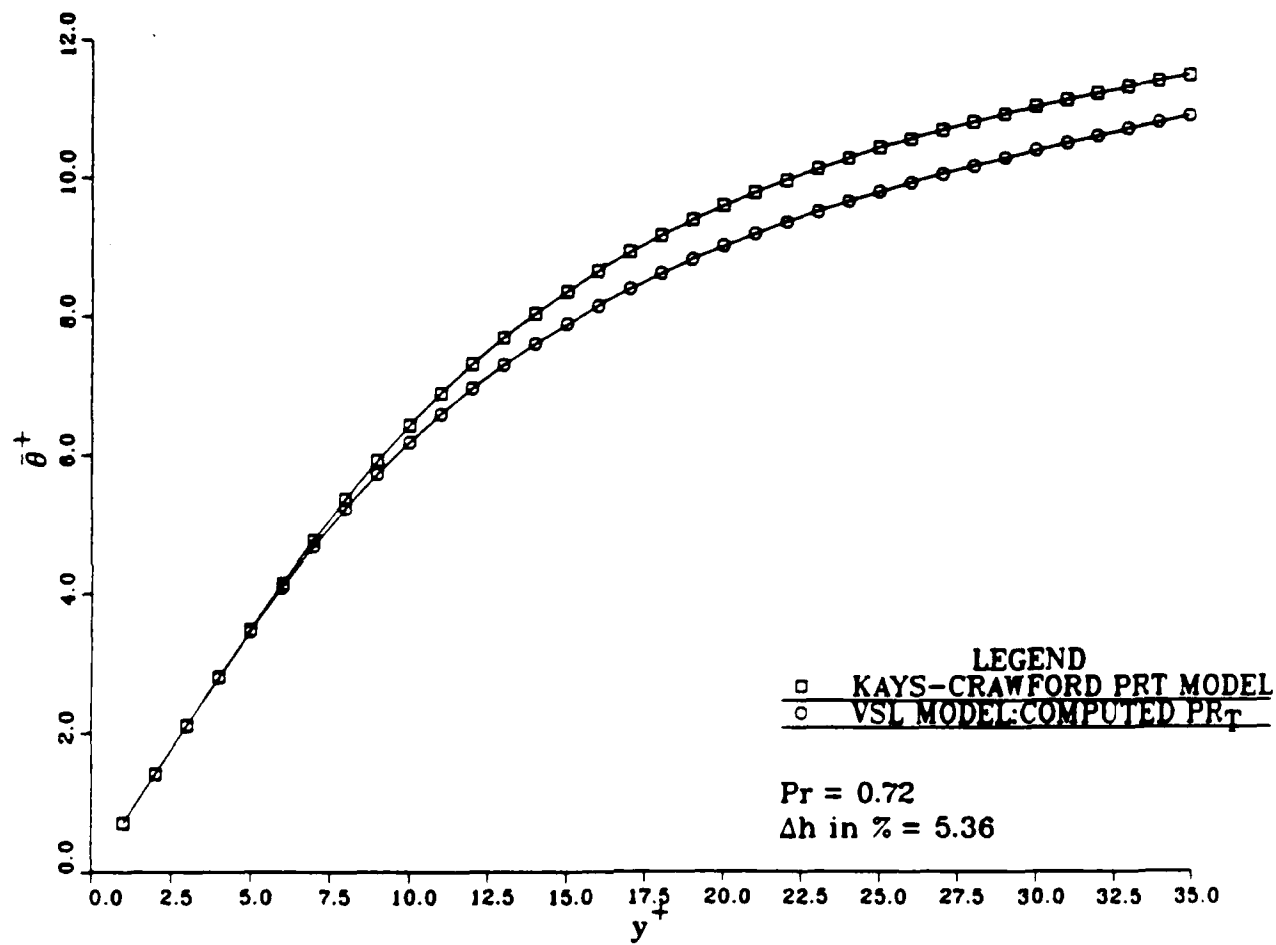
Figure 49 Temperature profile comparison between the Kays-Crawford model of Pr_T and the computed profile of Pr_T for $Pr = 0.72$. Δh represents approximate change in the convective heat transfer coefficient.
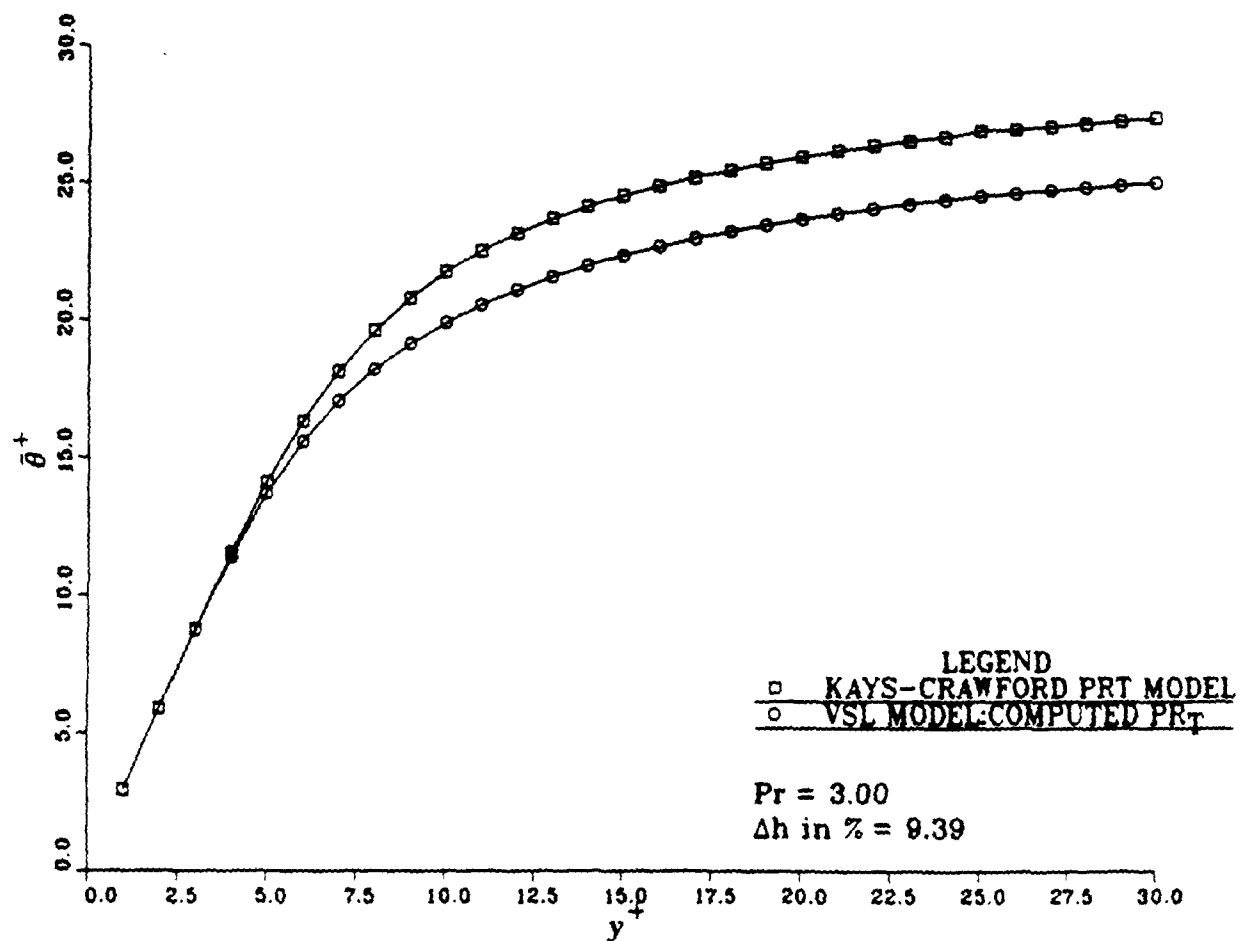
122
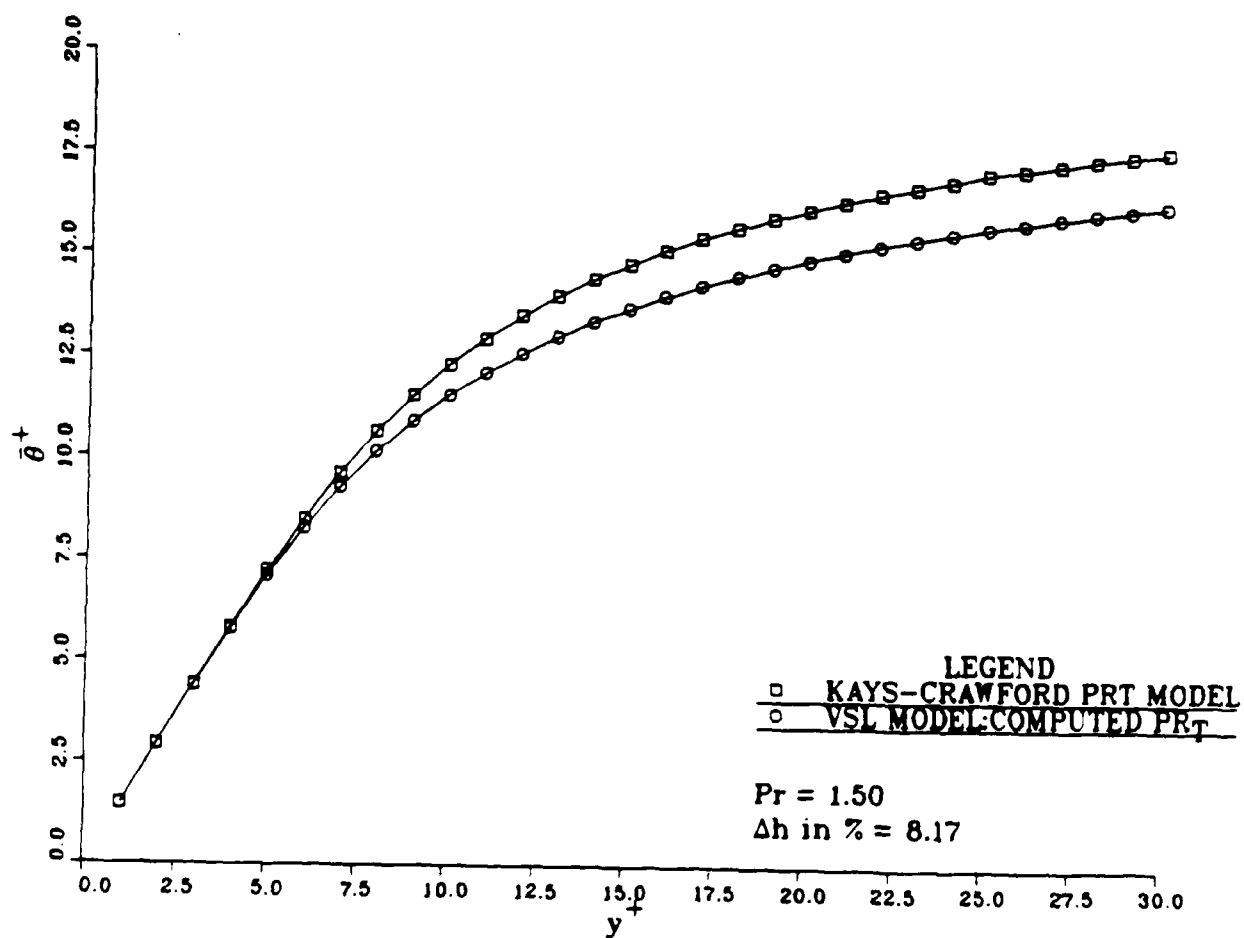
Figure 50 Temperature profile comparison between the Kays-Crawford model of Pr_T and the computed profile of Pr_T for $Pr = 1.50$. Δh represents approximate change in the convective heat transfer coefficient.
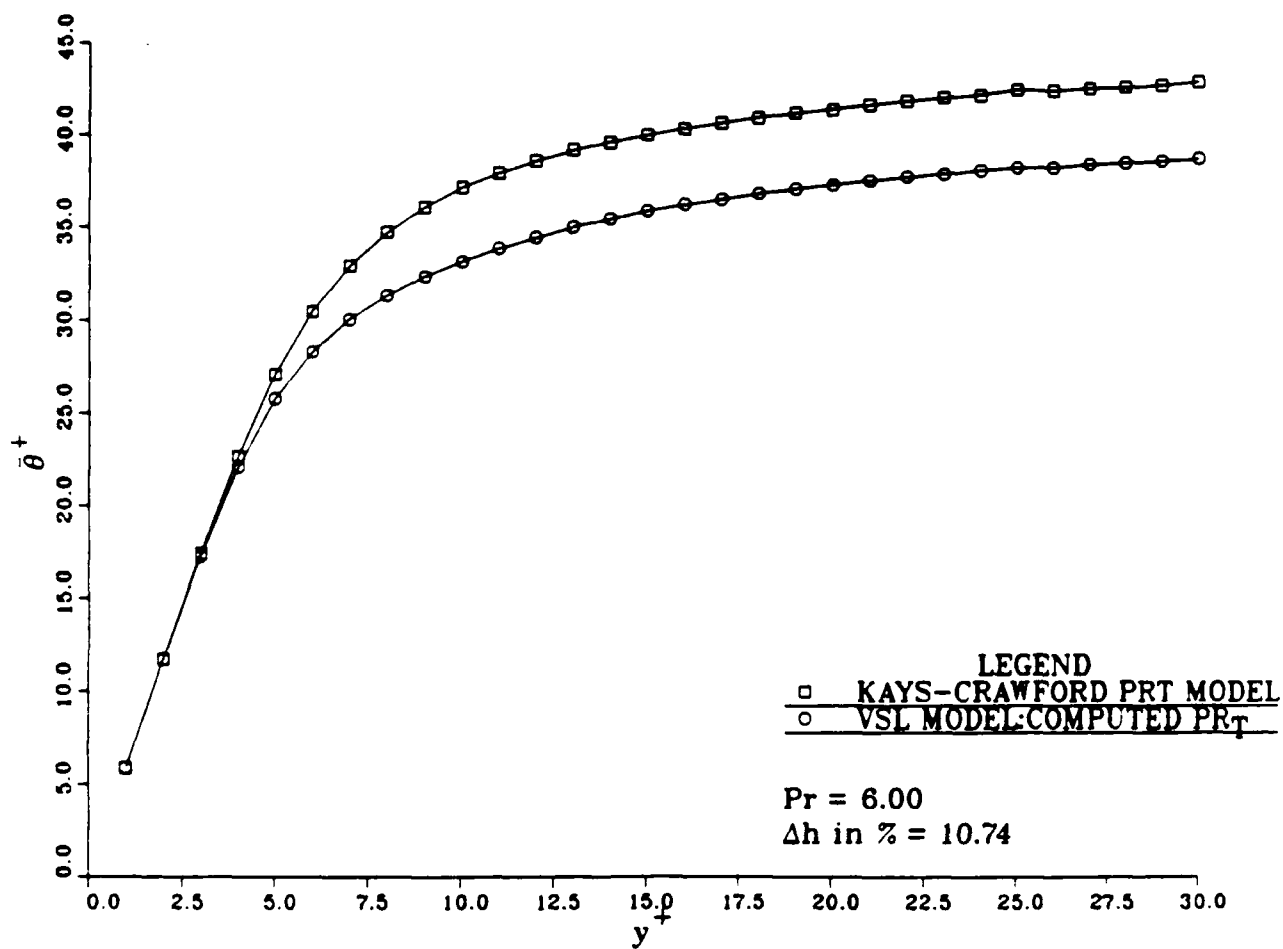
Figure 51 Temperature profile comparison between the Kays-Crawford model of Pr_T and the computed profile of Pr_T for $Pr = 3.0$. Δh represents approximate change in the convective heat transfer coefficient.

124

Figure 52 Temperature profile comparison between the Kays-Crawford model of Pr_T and the computed profile of Pr_T for $Pr = 6.0$. Δh represents approximate change in the convective heat transfer coefficient.
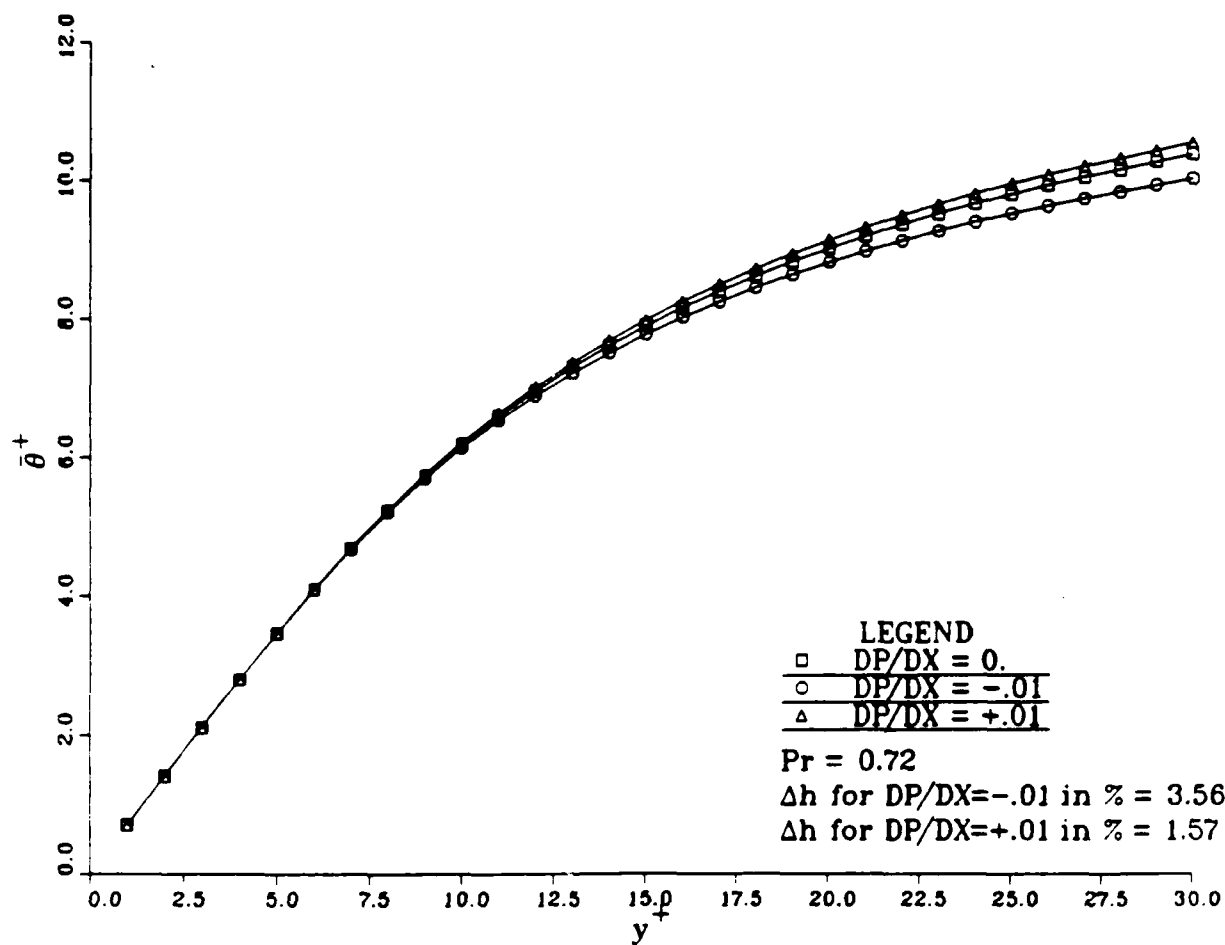
125

Figure 53 Temperature profile comparison between the the computed profiles of Pr_T with zero,adverse, and favorable pressure gradient for $Pr = 0.72$. Δh represents approximate change in the convective heat transfer coefficient.
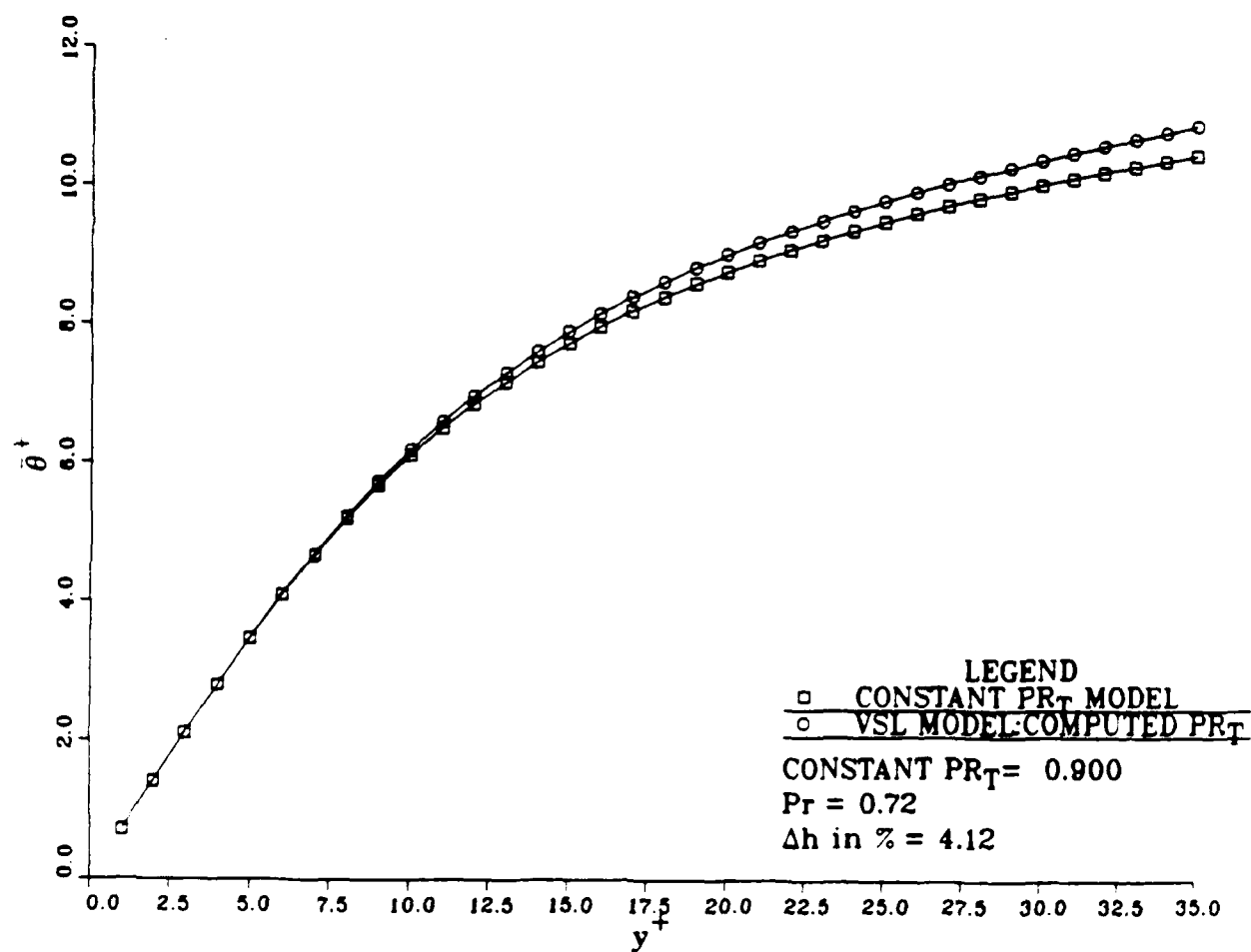
126

Figure 54 Temperature profile comparison between a constant $Pr_T = 0.9$ and the computed profile of Pr_T for $Pr = 0.72$. Δh represents approximate change in the convective heat transfer coefficient.
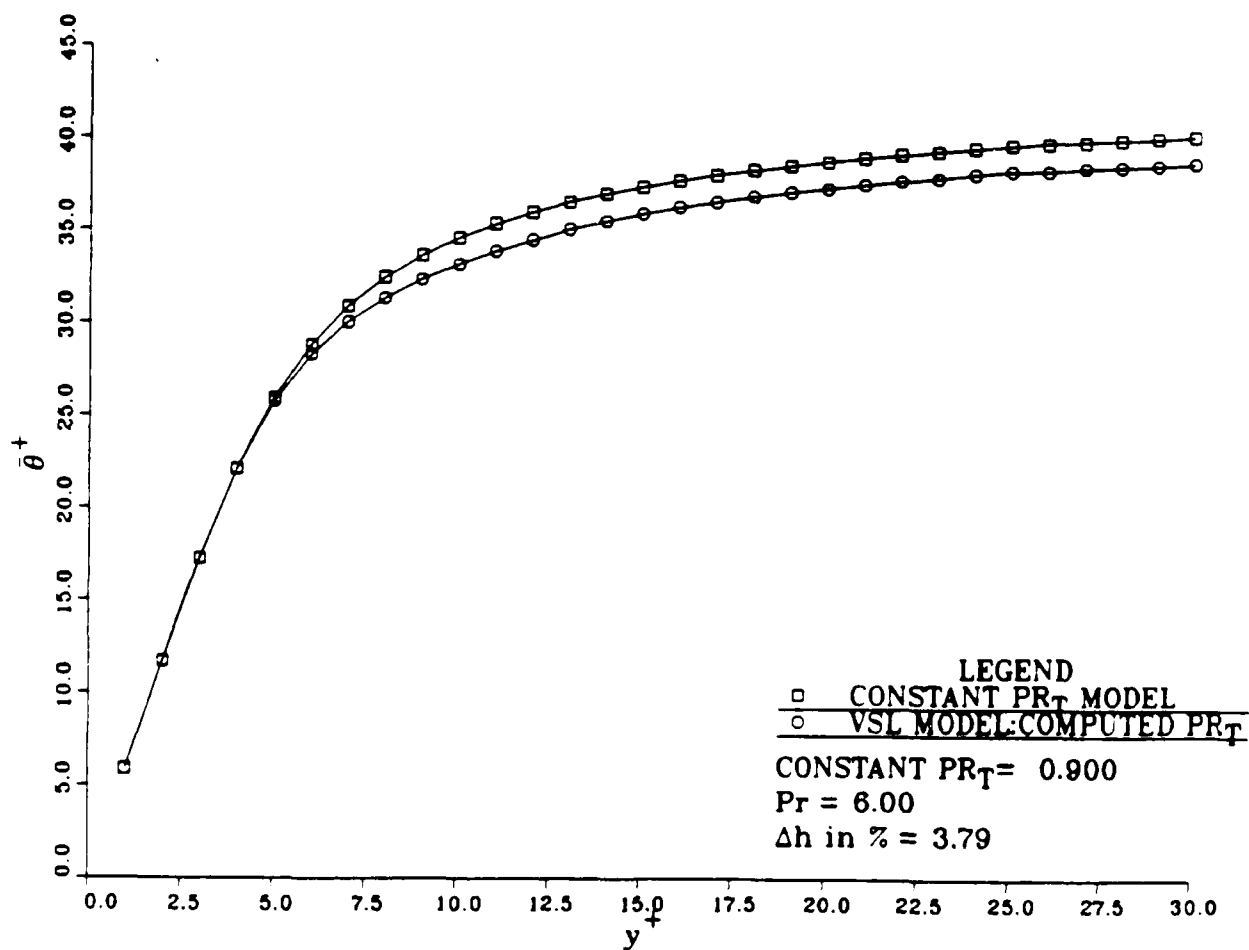
127

Figure 55 Temperature profile comparison between a constant $Pr_T = 0.9$ and the computed profile of Pr_T for $Pr = 6.0$. . Δh represents approximate change in the convective heat transfer coefficient.
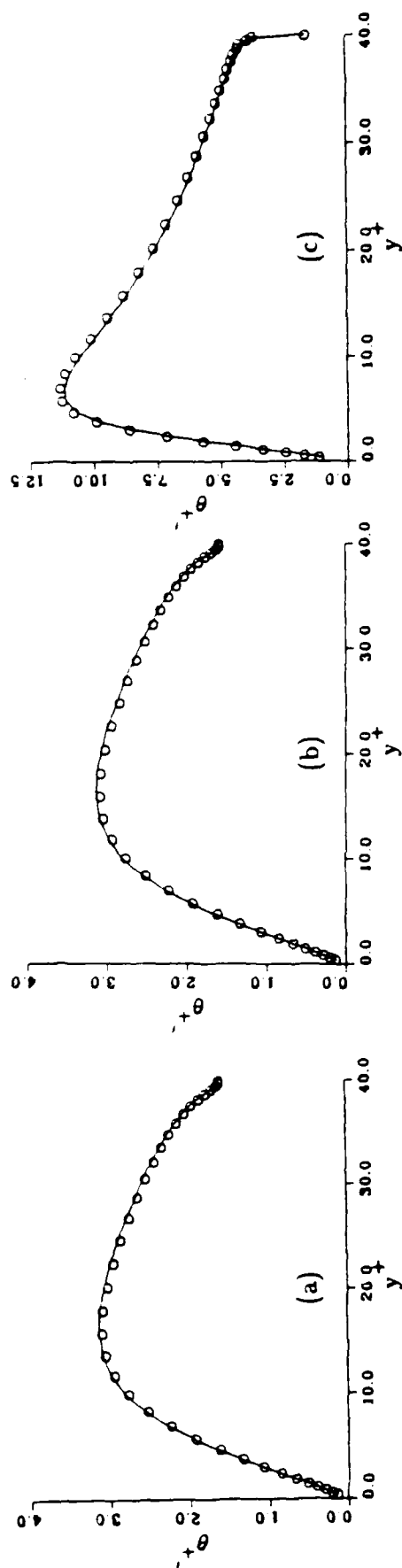
128

Figure 56 (a) Temperature intensity θ', air-copper interface, $P_T = 0.72$, (b) Temperature intensity θ', air-glass interface, $P_T = 0.72$. (c) Temperature intensity θ', water-copper interface. $P_T = 6.0$, for solid-fluid interface boundary condition runs, $\circ =$ isothermal wall temperature case.

129

END

2-87

DTIC